MAGNETOTRANSPORT STUDIES ON TOPOLOGICAL INSULATORS

A Dissertation

Submitted to

the Faculty of the Department of Physics

University of Houston

In Partial Fulfillment

of the Requirements for the Degree

Doctor of Philosophy

By

Keshav Shrestha

December 2015

MAGNETOTRANSPORT STUDIES ON TOPOLOGICAL INSULATORS

Keshav Shrestha

APPROVED:

Prof. Paul C. W. Chu, Chairman
Department of Physics

Prof. Wei Kan Chu
Department of Physics

Prof. Kevin Bassler
Department of Physics

Prof. Zhifeng Ren
Department of Physics

Prof. Allan Jacobson
Department of Chemistry

Dean, College of Natural Sciences and Mathematics

Acknowledgements

I would like to express my sincere gratitude to my dissertation supervisor Prof. Paul C.W. Chu for the continuous support during my PhD research. His constant encouragement and assistance at all times have been of immense value. Besides my advisor, I would like to express my deepest gratitude to Dr. Bernd Lorenz for his patient guidance, enthusiastic encouragement and useful comments throughout my research. I would like to thank to my PhD committee members, Prof. Kevin Bassler, Prof. Wei Kan Chu, Prof. Zhifeng Ren and Prof. Allan Jacobson for their insightful comments and encouragements with some hard questions which incented me to widen my research from various perspectives. I would like to extend my gratitude to other High-Pressure Low-Temperature team, Melissa Gooch, Zheng Wu, Ben Jawdat, Lianzi Deng, Kui Zhao, Narayan Poudel, Hanming Yuan, Shuyan for their assistance and having intense discussions to solve problems. I would like to thank Prof. Carlos Ordenez for bringing me from the Abdus Salam International Center for Theoretical Physics (ICTP) to the Physics Department at University of Houston. Some of my friends who deserve special thanks for their help and friendly advice are Rooplekha Mitra, Kalyan Sasmal, and all Nepalese students at the University of Houston.

Last but not the least, I would like to thank my family: my parents and to my brother for their love and support. A special thanks to Irina Galstyan for her true love and encouragement throughout my Ph.D. life. I will forever remain indebted to her. I wish for her success and happiness.

MAGNETOTRANSPORT STUDIES ON TOPOLOGICAL INSULATORS

An Abstract of a Dissertation
Presented to
the Faculty of the Department of Physics
University of Houston

In Partial Fulfillment
of the Requirements for the Degree
Doctor of Philosophy

By
Keshav Shrestha
December 2015

Abstract

The present work describes the magnetotransport studies of topological-surface state (SS) in metallic topological compounds. We have chosen three different classes of topological insulators, $Bi_2Se_{2.1}Te_{0.9}$ (BST), Bi_2Te_3 (BT), and Sb_2Te_2Se (STS) for our study. The BST sample shows metallic behavior and has p-type bulk charge carriers. From the angle dependence of quantum oscillations and our Berry phase calculations, we have proved the existence of topological SS in the metallic BST sample. Based on the frequency analyses at high field, up to 35 T, the SS quantum oscillations dominate at low magnetic field and the surface to bulk state cross-over of oscillations takes place at higher magnetic field. The physical origin of the SS in the BST metallic sample can be understood as the low position of the Fermi energy measured from the Dirac point; however, it still cuts the two valence band maxima in the band structure explaining the bulk metallic property. We have found the existence of weak antilocalization (WAL) in the three BT metallic single crystals with different bulk charge carriers. From the angle dependence of the WAL, we found that the topological SS dominates in the samples having lower bulk carriers. From our Hikami-Larkin-Nagaoka analyses, we have found a larger number of conduction channels and a smaller phase coherence length in the samples having more bulk carriers as compared to those having less bulk carriers. Similar magnetoresistance measurements have been carried out in the p-type metallic STS sample in high-field up to 31 T. The angle dependence of quantum oscillations and the Berry phase calculations also show the dominance of topological SS. The physical origin of topological SS in the STS sample can be understood the same way as in the BTS sample.

Contents

List of Figures

List of Tables

Chapter 1

Introduction

The discovery of a new state of matter is always the driving force of condensed matter physics research. This has led to many historical discoveries such as superconductivity [1], the quantum Hall effect (QHE) [2], the fractional quantum Hall effect (FQHE) [3]. The recent discovery of the topological insulating state of matter has opened a new area of research in condensed matter physics [4] [5]. The topological insulating state is a new manifestation of quantum mechanics which exploits the non-trivial topology of Hilbert space, a space spanned by wave functions characterizing electronic states. Depending upon how the Hilbert Space becomes topologically non-trivial, there are many different kinds of topological insulators [6].

The topologically non-trivial bulk states in topological insulators (TIs) lead to the existence of metallic states when the insulator is physically terminated and interfaces with an ordinary insulator (including vacuum) [5]. The metallic states in 2 dimensional (2D) topological insulators appear as edge states (edge modes) and as

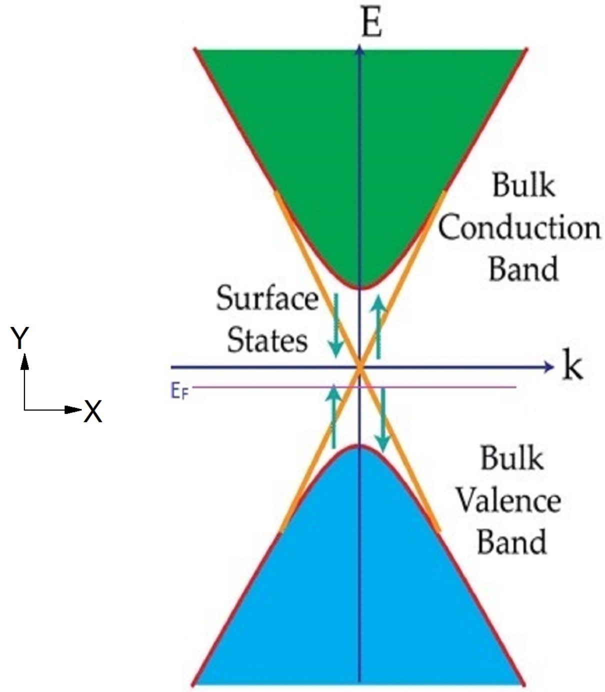

Figure 1.1: An energy (E) versus momentum (k) band structure sketch of a topological insulator. The Fermi level (E_F) lies somewhere in between the bulk valence band and conduction band. The surface states with spins up and down form a Dirac-like dispersion.

surface states in 3 dimensional (3D) topological insulators. The edge/surface state is protected by symmetry-like time-reversal symmetry (TRS) in 3D topological insulators. The surface states of 3D topological insulators show a characteristic Dirac dispersion as shown in Fig. [1.1], and the quasi-particles in this state are massless Dirac fermions where the spin is locked to the momentum, thereby forming a helical spin state.

Due to topological protection, the surface state (SS) is very stable and robust against disorder. The presence of surface states allows for potential applications in technology like spintronics and computer memory devices because of their stability and robustness [5]. Moreover, topological insulators can exhibit many exotic quantum effects. For example, $BiSbSe_2Te$ shows the QHE under high magnetic field [7]. By breaking time reversal symmetry (TRS) with magnetic impurities like chromium (Cr), TIs show the quantum anomalous Hall Effect (QAHE) [8] [9]. Furthermore, the proximity-induced superconductivity in TIs may pave the way towards the discovery of Majorana fermions, quasi-particles which are their own antiparticles [10][11]. Bi_2Se_3 is a topological insulator, which becomes superconductive with Cu or Sr intercalation [12] [13].

The transport characteristics of the SS are important for technological applications if the bulk is insulating. However, the majority of 3D topological insulators discovered until now, such as the bismuth chalcogenides like Bi_2Se_3, Bi_2Te_3, Bi_2Se_2Te or Bi_2Te_2Se, always have crystal defects (point, dislocations or antisite defects) [5]. The Fermi level lies either in the conduction band or the valence band; depending on the type of crystal defects, the bulk charge carriers will be of either electron or hole type. In such a case, the bulk conduction channel interferes SS which makes the transport studies of topological SS difficult and extremely challenging. A systematic transport study of Bi_2Te_3 single crystals (both metallic and non-metallic) has been completed, Qu *et al* [14] and they reported that it is hard to detect the topological SS in the metallic samples due to significant interference from the bulk conduction channel. The metallic sample studied by Qu *et al* has n-type bulk charge carriers. The question which still remains is: is it possible to detect SS in metallic samples by transport measurements? In this research work, we have carried out systematic magnetotransport studies on 3 different types of metallic topological insulating samples $Bi_2Te_{2.1}Se_{0.9}$, Bi_2Te_3 and Sb_2Te_2Se. Our angle dependent quantum oscillations and Berry phase calculations showed the existence of topological surface states in $Bi_2Te_{2.1}Se_{0.9}$ and Sb_2Te_2Se samples. Similarly, we have observed weak antilocalization (WAL) effects on the metallic Bi_2Te_3 sample. The angle depedence of the WAL effect proved the dominance of topological surface states in the magnetoconductivity of Bi_2Te_3 single crystals having lower bulk carriers.

In Chapter 2, I will present a broad but concise review of the topological phases of materials and their fundamental physical properties. Chapter 3 will cover the experimental methods used to carry out the measurements. Chapter 4 will include the results followed with discussions. Finally, Chapter 5 will summarize the whole research work with conclusions.

Chapter 2

Background

Electrons and atoms in the quantum world form many different states of matter [15]. Crystals, magnets, superconductors etc. are different states of matter. Quantum states are classified by the principle of "spontaneous symmetry breaking" [16]. For example: water and ice are the same material; however, they form different phases. The translational symmetry that exists in an ice crystal is broken when water is formed. Similarly, a ferromagnet breaks the rotational symmetry of electron spins; a superconductor breaks gauge symmetry, etc. Hence, a phase transition is equivalent to a symmetry breaking. Recently, a new state of matter has been discovered. Materials belonging to this state are classified based on a topological quantum number, sometimes known as a topological invariant [4][5]. A topological insulator has been theoretically predicted [17][18][19] and discovered experimentally later on [20][21]. The most interesting and useful property of a topological insulator is the surface state. There is a continous transition of electronic states if two materials

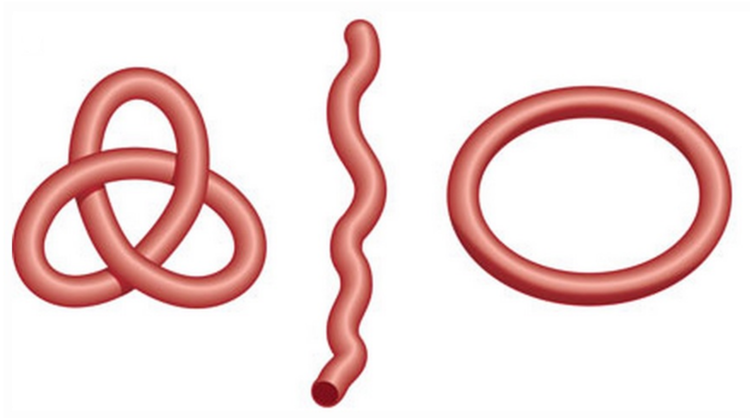

Figure 2.1: The trefoil knot (left) and the simple loop (right) represent different insulating materials: the knot is a topological insulator, and the loop is an ordinary insulator. The figure is adapted from the reference [22].

of the same topology interface with each other. However, a conducting edge state (surface state) appears if two materials of different topological phases interface with each others [22]. Geometrically, this can be understood by taking a simple cartoon as shown in Fig. [2.1]. Consider, for example, that we want to change a topologically non-trivial trefoil knot to a topologically trivial simple loop. From the theory of topology, the topology of an object does not change under a continous deformation [23]. However, in case of the above example Fig. [2.1] there is no way to convert the trefoil knot into the simple loop with a continous deformation. The only way to deform a trefoil knot into a simple loop is to cut the string and then reconnect it. However, the topological invariant is not defined for the string with open ends (middle in Fig. [2.1]). Similary, to go from one phase of matter defined by a certain topological invariant to another phase of matter defined by a different topological invariant, an intermediate state with an "undefined" topological invariant is needed; this is known as the metallic surface state. Some examples of topological insulators

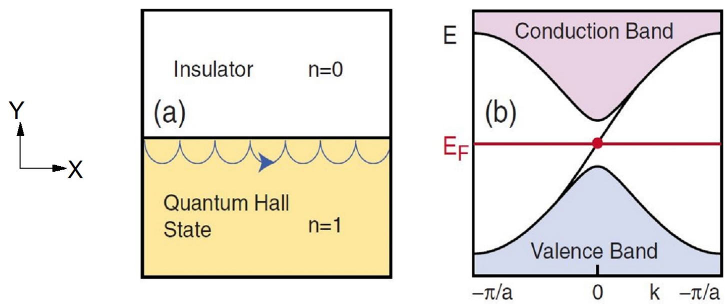

Figure 2.2: The interface between a quantum Hall state and an insulator has chiral edge mode. (a) The skipping cyclotron orbits. (b) The chiral edge mode which connects valence band to conduction band. The figure is adapted from the reference [4].

are the materials that show the quantum Hall Effect (QHE).

2.1 Quantum Hall Effect

QHE is the quantization of Hall conductance in 2D electron gas under high magnetic field [2]. The 2D electron gas is usually found in semiconductor interfaces. An electron moving in a magnetic field B experiences a Lorenz force of $F = Bev$ (e is electron charge and v is its velocity) and exhibits cyclotron motion with a frequency $\omega_c = \frac{eB}{m_{cyc}}$ (m_{cyc} is the cyclotron mass). The energy levels are quantized as

$$\epsilon_n = (n + \frac{1}{2})\hbar\omega_c,$$

n is an integer, also known as Landau level (LL); the consecutive Landau levels are separated by an energy of $\hbar\omega_c$. The Hall conductivity is quantized as

$$\sigma_{xy} = N\frac{e^2}{h} \tag{2.1}$$

where N is the filling factor. N can take any integer value in the QHE [2] and any positive rational number in fractional quantum Hall effect (FQHE) [3]. In the semiclassical picture, the QHE can be understood in terms of cyclotron motion of electrons. An electron inside the sample undergoes cyclotron motion about the axis of applied field; however, an electron close to the boundary can not complete its cyclotron orbit and makes an escaping orbit as shown in Fig. [2.2(a)]. These escaping orbits on the boundary can be regarded as the motion of an electron. The edge state is chiral and represented as a gapless state in the band structure Fig. [2.2(b)]. Thus, the electrons in the bulk do not conduct, but the edge electrons contribute to the flow of current at the edge in the QHE. That is why a QHE material is regarded as a topological insulator [4]; N is also regarded as the Thouless, Kohmoto, Nightingale, and den Nijs (TKNN) number. TKNN showed that the QHE is not only a quantum mechanical phenomenon, but also has a topological origin. They mapped the quantum Hall system in k-space to a topologically non-trivial Hilbert space, whose topology can be specified by an integer number N [24].

$$N = \frac{1}{2\pi} \int_{BZ} \nabla_k \times A(k_x, k_y) d^2k \tag{2.2}$$

where $A = -i <u_k|\nabla_k|u_k>$ is a vector potential, and $|u_k>$ is a Bloch wave function with a wave vector k. Thus, the precise quantization of Hall conductance can be understood in terms of topological protection.

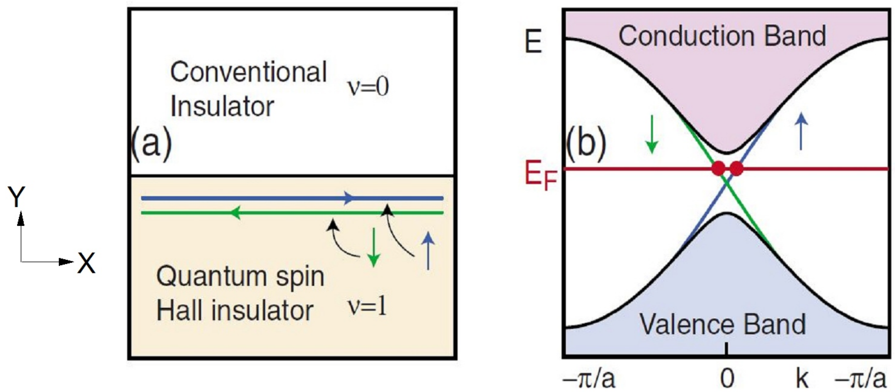

Figure 2.3: Quantum Spin Hall Insulator (QSHI). (a) The interface between QSHI and a trivial insulator. (b) Energy (E) versus wave vector (k) band structure of a QSHI. The Fermi energy (E_F) lies in between the valence and conduction bands. The figure is adapted from the reference [4].

2.2 Quantum Spin Hall State

In the quantum Hall effect, the time reversal symmetry (TRS) is broken because of external magnetic field. However, a question that still remained unanswered during that time is the existence of quantum Hall like states without external magnetic field. In order words, can we get a quantum Hall like state without breaking the TRS? This question could be answered after the discovery of the quantum spin Hall effect, where spin orbit coupling (SOC) provides an internal magnetic field [25].

Initially, the quantum spin Hall effect (QSHE) was considered as a combination of two QHE i.e. there are two edge currents, spin up and spin down, which preserve TRS. However, the TKNN or Chern number of two independent edge currents for spin up and spin down electron add up to give zero i.e. the net Chern number $n = n \uparrow + n \downarrow = 0$ [26]. However, that does not mean that QSHE is a topologically trivial state. Kane and Mele found a way to define another topological invariant ν in QSH system, which takes values of 0 or 1 [27]. For the QSHE, ν is equal to 1, and there exist two edge states (spin up and spin down) which form a Dirac cone. The quantum spin Hall state is a real 2D topological insulator and has been discovered in the HgTe/CdTe quantum well [28].

In this dissertation, we have studied the 3D topological insulator, which is the extension of the 2D topological insulator. The surface state in a 3D topological insulator is protected by TRS as in QSHE.

2.3 Quantum Oscillations

Ideally, a topological insulator should have large bulk resistivity so that only the surface state conducts electrical current. However, due to scattering and crystal defects in bismuth-based topological insulators, a bulk conduction channel always exists and this interferes with the surface channel. Therefore, resistance measurements alone cannot detect surface states. However, under the application of magnetic field, the resistivity or conductivity of a topological insulator shows quantum oscillations, known as Shubnikov de Haas (SdH) oscillations [29]. Physically, the origin of quantum oscillations can be understood in terms of the quantization of electron density of states into Landau levels in the presence of a magnetic field. With an increase of magnetic field, the Fermi level crosses the Landau levels (as shown in Fig. [2.4]) i.e. the density of states (DOS) becomes a periodic function of the magnetic field, which leads to oscillations in the physical properties of the materials. The angle dependence of the quantum oscillations with respect to the direction of magnetic field

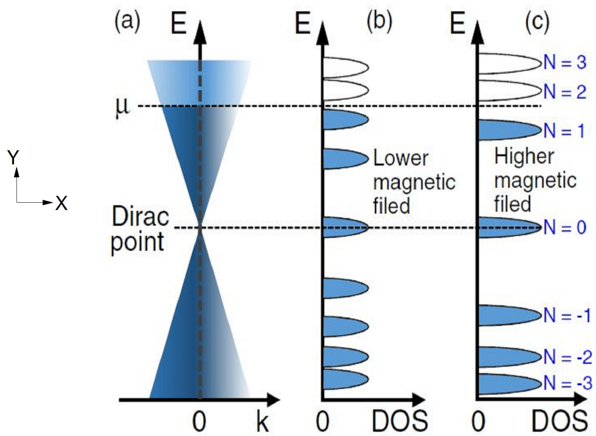

Figure 2.4: (a)Partially-filled 2D Dirac cone; μ is the Fermi level.(b) Landau quantization of the Dirac cone; LLs below μ are filled with electrons.(c) In a higher magnetic fields, the spacing between LLs increases as $\sqrt{N}$, and fewer Landau levels are filled. The figure is adapted from the reference [5].

allows one to map the Fermi surface, which ultimately probes whether the quantum oscillations originate from 2D surface states or 3D bulk states. Moreover, the phase factor of the quantum oscillations allows for the calculation of the Berry phase. It directly reflects the nature of the charge carrier, i.e. either Dirac fermions or normal electrons [5]. Thus, the ability to detect quantum oscillations is a very important tool for the study of surface states in 3D topological insulators.

2.3.1 Onsager Relation

Onsager developed a mathematical formula that maps the cross-sectional area of the Fermi surface to the frequency of quantum oscillations. The following derivations are inspired by Ashcroft and Mermin [30], and Kittel [15]. According to Bohr's corresponding principle, the spacing between two Landau levels is $\hbar\omega_c$,

$$
\begin{aligned}
E_{\nu+1}(k_z) - E_\nu(k_z) &= \hbar\omega_c \\
&= \hbar\frac{eB}{m_{cyc}}
\end{aligned}
\tag{2.3}
$$

where ν is LL index which is an integer number, k_z is the z component of the wave vector k, and m_{cyc} is the cyclotron mass of electron, which is defined as

$$
m_{cyc}(E_\nu, k_z) = \frac{\hbar^2}{2\pi}\frac{\partial A(E_\nu, k_z)}{\partial E}. \tag{2.4}
$$

where $A(E_\nu, k_z)$ is the area enclosed in k space by cyclotron orbit.
Combining Eq. [2.3] and Eq. [2.4], we get

$$
E_{\nu+1}(k_z) - E_\nu(k_z) = \frac{2\pi eB}{\hbar[\frac{\partial A(E_\nu, k_z)}{\partial E}]}. \tag{2.5}
$$

From the results of free electrons under a magnetic field, the energy difference between Landau levels is $\hbar\omega_c$, which is at least 10^{-4} times smaller than the energies of the levels themselves. So, we can approximate the expression

$$
\frac{\partial A(E_\nu, k_z)}{\partial E} = \frac{A(E_{\nu+1}, k_z) - A(E_\nu, k_z)}{E_{\nu+1}(k_z) - E_\nu(k_z)}. \tag{2.6}
$$

Putting Eq. [2.6] in Eq. [2.5], we get

$$
A(E_{\nu+1}, k_z) - A(E_\nu, k_z) = \Delta A = \frac{2\pi eB}{\hbar} \tag{2.7}
$$

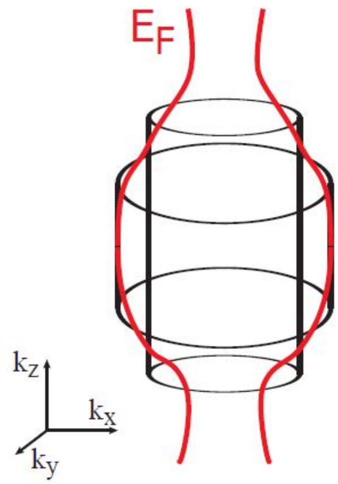

Figure 2.5: Landau levels in 3 dimension are cylindrical tubes as shown and the Fermi surface is displayed by the red lines.

Equation [2.7] states that the area between two adjacent classical orbits (at the same k_z) can differ only by a fixed amount ΔA. Thus the cross-section area enclosed by an orbit of LL ν is given by

$$A = \pi k_F^2 = (\nu + \beta)\Delta A \tag{2.8}$$

where β represents a phase constant which is connected to the Berry phase and gives information about the nature of the Dirac spectrum. For free spin 1/2 particles, the phase constant is 1/2. k_F is the Fermi wave vector. Substituting the value of ΔA from Eq. [2.7], we get

$$A = (\nu + \beta)\frac{2\pi e B}{\hbar c} \tag{2.9}$$

In Fermi surface experiments we may be interested in the increment ΔB for which two successive orbits, ν and ν+1, have the same area in k space on the Fermi surface.

The area is equal when

$$A\left(\frac{1}{B_{\nu+1}}-\frac{1}{B_{\nu}}\right)=\frac{2\pi e}{\hbar c} \tag{2.10}$$

Equation [2.10] is an important result which implies that equal increments of 1/B reproduce similar orbits - this periodicitiy is a striking feature of the magneto-oscillatory effects in many physical properties of metals at low temperature.

2.3.2 Lifshitz Kosevich Theory

Various physical quantities which characterize quantum oscillations, like the cyclotron mass m_{cyc}, the scattering time τ, mobility μ and etc., can be evaluated using the Lifshitz Kosevich theory. Following Shoenberg [29], the quantum oscillations in conductivity can be expressed as

$$\Delta R_{xx}=\Delta R_0 R_T R_D R_S cos\left[2\pi\left(\frac{F}{B}-\frac{1}{2}+\beta\right)\right] \tag{2.11}$$

where ΔR_0 is a constant and the three coefficients,
$R_T=2\pi^2(k_BT/\hbar\omega_c)/sinh[2\pi^2(k_BT/\hbar\omega_c)]$, $R_D=exp[-2\pi^2(k_BT_D/\hbar\omega_c)]$ and
$R_S=cos(\frac{1}{2}\pi g m_e/m_{cyc})$ are called temperature, Dingle, and spin damping factors, respectively with T_D the Dingle temperature (g is the electron g-factor and m_e is the free electron mass). For a given magnetic field, R_D does not change and temperature dependence shows up only through R_T. Thus, the cyclotron frequency ω_c can be calculated using the temperature dependence of quantum oscillation amplitude, which in turn gives $m_{cyc}=eB/\omega_c$. From Eq. [2.4],

$$m_{cyc}(E_\nu,k_z)=\frac{\hbar^2}{2\pi}\left[\frac{\partial A(E_\nu,k_z)}{\partial E}\right]_{E=E_F}. \tag{2.12}$$

In case of 2D Dirac fermions, the energy dispersion is $E(k) = \hbar v_F k$, and one obtains $A(E_F) = \pi k_F^2 = \pi E_F^2/(\hbar v_F)^2$ and hence $m_{cyc} = E_F/v_F^2 = \hbar k_F/v_F$. Thus, by calculating the cyclotron mass m_{cyc}, we can calculate Fermi velocity $v_F = \hbar k_F/m_{cyc}$. Other quantities like the Dingle temperature, T_D, can be determined from the magnetic field-dependence of the amplitude of the SdH oscillations at a fixed temperature and obtain the quantum scattering time, τ. The obtained τ can be used to calculate the mean-free-path $l^{SdH} = v_F\tau$, which in turn gives an estimate of the surface carrier mobility $\mu_s^{SdH} = e\tau/m_{cyc}$.

2.4 Weak Antilocalization

Weak antilocalization (WAL) is a quantum interference effect in quantum transport of a disordered electron system having strong spin-orbit coupling [31]. These effects have been widely observed in topological insulators [32][33][34]. The WAL effect enhances the conductivity. However, in the presence of magnetic field, time reversal symmetry (TRS) is broken and, consequently, the magnetoconductivity decreases. Thus, negative magnetoconductivity is taken as an experimental signature of WAL [31] as shown in Fig. [2.6].

2.4.1 Physical Origin of WAL

Motion of an electron in a disordered system is characterized by three parameters, the scattering length (l), the phase coherence length (l_ϕ) and the sample length (L).

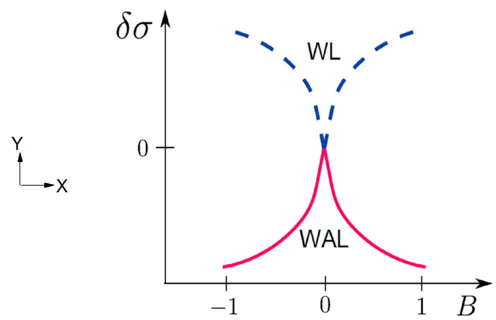

Figure 2.6: Conductivity as a function of magnetic field B. Negative and positive mangnetoconductivities are taken as signature of WAL and WL respectively. The figure is adapted from the reference [35].

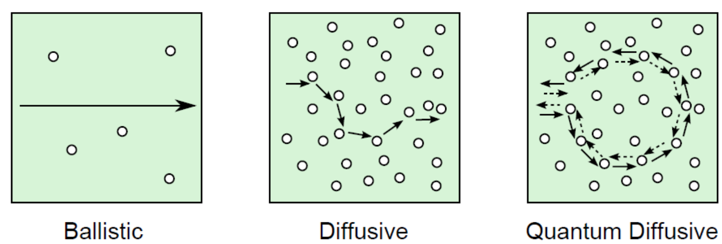

Figure 2.7: Schematic illustration of different electronic transport regimes in solids. The open circles represent impurities and arrows mark the trajectories that electron travelled. The figure is adapted from the reference [31].

Depending upon the disorders in a given sample as shown in Fig. [2.7], the motion of electrons can be either (i) ballistic ($l > L$), (ii) diffusive ($l < L$, and $l << l_\phi$), or (iii) quantum diffusive ($l_\phi >> l$). In diffusive region, we can use the classical Drude formula to calculate the conductivity. However, the quantum interference between two time-reversed paths in the quantum diffusive region gives quantum correction to the conductivity. The quantum correction is mostly due to quantum interference effects between self-crossing electron paths [36]. The electron paths due to scattering can be either clockwise or counter-clockwise as shown in Fig. [2.8]. Due

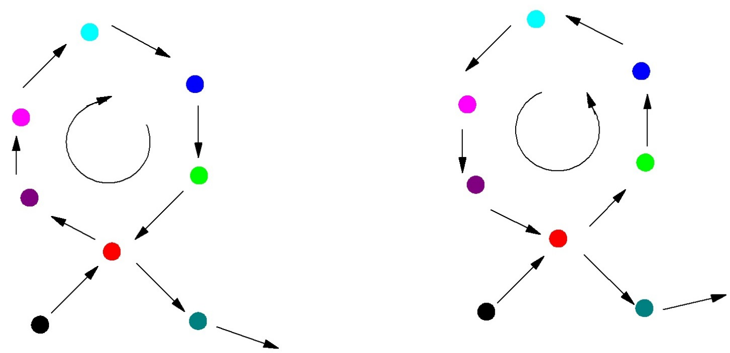

Figure 2.8: Schematic illustration of different electron paths in a disorderd system. (a) Clockwise (b) Anticlockwise.

to the identical lengths of the two paths along a loop, the quantum phases cancel each other out; if not, they are random in sign (i.e. the quantum interference terms survive upon disorder averaging). In strong-spin orbit interaction (SOI) systems, the electron spin is coupled to its momentum. The phase difference between two time-reversed paths for a spin is 2π. However, the wavefunction of a spin changes sign for the rotation of 2π, this causes a destructive interference. The destructive interference increases the conductivity; this is called weak antilocalization. Since it is more probable to find self-crossing paths in lower dimensions, the WAL effect is more tangible to thin films or wires. In two dimensions, the quantum correction to conductivity is described by the Hikami-Larkin-Nagaoka (HLN) formula [37]

$$\sigma(B) - \sigma(0) = \Delta\sigma_{xx}(B) = \alpha\frac{e^2}{\pi h}\left[\Psi\left(\frac{\hbar c}{4el_\phi^2 B} + \frac{1}{2}\right) - ln\left(\frac{\hbar c}{4el_\phi^2 B}\right)\right] \tag{2.13}$$

where Ψ is the digamma function and l_ϕ is the phase coherence length. The pre-factor α takes a value of $\frac{1}{2}$ per conduction channel that carries the π Berry phase or bears a strong SOC.

Equation [4.4] is derived for 2D systems like thin films having strong SOC. However, this formula still can be used in case of 3D topological insulators having insulating bulk channels. The surface channel is 2D in nature and many physical properties can be studied using the HLN formula.

Chapter 3

Methods

3.1 Sample Preparation

3.1.1 $Bi_2Se_{2.1}Te_{0.9}$ Single Crystal

Single crystals of $Bi_2Se_{2.1}Te_{0.9}$ were grown by a modified Bridgman technique. The starting materials with high purity, Bi (99.9999%), Se (99.9999%), and Te (99.9999%), were mixed according to the desired compositions in encapsulated quartz ampoules of 20 mm diameter. The mixtures were annealed at 875 ^{o}C for 48 hour in order to obtain a homogenized melt. Then the melt was cooled to 670 ^{o}C at a rate of 0.5 ^{o}C/hour. Finally, the crystals were cooled to room temperature at a rate of 0.5 ^{o}C/hour. The single crystals of $Bi_2Se_{2.1}Te_{0.9}$ were grown by Dr. Vera Marinova at the Institute of Optical Materials and Technology, Bulgarian Academy of Sciences, Acad. G. Bontchev Str. 109, Sofia 1113, Bulgaria. Figure [3.1] shows the

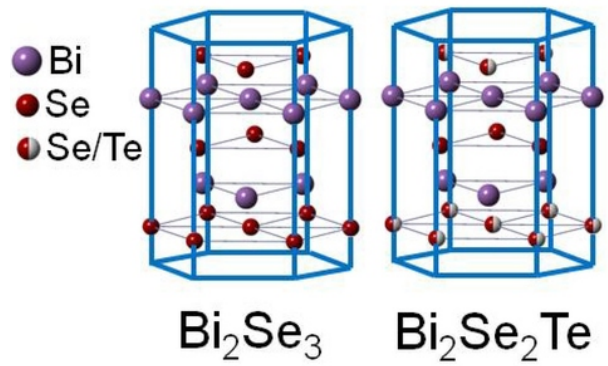

Figure 3.1: Crystal Structures of Bi_2Se_3 and Bi_2Se_2Te. The picture is adapted from the reference [38].

crystal structures of Bi_2Se_3 and Bi_2Se_2Te. The crystal is rhombohedral with hexagonal planes. The rhombohedral crystal structures of Bi_2Se_3 and Bi_2Se_2Te consist of hexagonal planes of Bi and Se/Te stacked on top of each other along the z-direction.

3.1.2 Sb_2Te_2Se Single Crystal

The preparation of Sb_2Te_2Se crystals is described further as follows. First binary compounds Sb_2Se_3 and Sb_2Te_3 were synthesized. The synthesis was done by using stoichiometric quantities of the starting materials Sb, Se, and Te, with purity of 99.9999%, mixed in quartz ampoules with a diameter of 20 mm, vacuumed to 10^{-6} torr. The synthesis and homogenization process last for 25 hours at a temperature in the interval 620 - 650 ^{o}C. The binary compositions prepared in this way were mixed to the desired ternary compounds and then placed in quartz ampoules with diameter 10 mm and after that vacuumed to 10^{-6} torr and sealed. These ampoules were further positioned in Bridgman crystal growth furnace. In the furnace the ampoules were heated to 650 ^{o}C and homogenized for 36 hours. The crystal growth process was performed through temperature decreasing with a speed of 0.5 ^{o}C per hour in the interval 650 - 570 ^{o}C. Further in the temperature interval from 570 ^{o}C to room temperature, the ampoules were cooled with a speed 10 ^{o}C/ hour. The single crystals of Sb_2Te_2Se were grown by Dr. Vera Marinova in Institute of Optical Materials and Technology, Bulgarian Academy of Sciences, Acad. G. Bontchev Str. 109, Sofia 1113, Bulgaria.

3.2 Experimental Setup

3.2.1 Sputtering Gold Contacts

A fresh single crystal of a typical size 5 mm×3 mm×0.1 mm was cleaved and cut into a rectangular shape. The selected sample was patterned using scotch tape as a mask. Six gold contacts were sputtered on the top surface (a-b plane) of the sample using an Anatech Hummer 6.2 sputtering machine as shown in Fig. [3.2]. The sample was placed inside the glass jar and purged with argon gas several times. A constant flow of argon was maintained with a pressure of approximately 100 mbar. Under a high dc electric field, the argon gas atoms ionize and form a plasma. A continous bombardment of argon ions (Ar^{+}) on the gold target caused erosion of gold atoms which then was deposited on the sample. The sputtered sample was attached on a substrate (MgO) using GE varnish. The geometrical configuration of the sample for

Figure 3.2: Hummer 6.2 sputtering and carbon coating machine. A sample is placed inside the glass jar (shown on the top) and a high dc electric field is applied from the control unit.

the transport measurements is shown in Fig. [3.3]. Six platinum wires were attached using silver paint. I^+ and I^- represent the current contacts; V_L and V_T represent pairs for the longitudinal and transverse voltages, respectively. The dot sign inside the circle shows that the magnetic field is pointing out and perpendicular to the sample surface i.e. ab plane. The sputtered gold contacts are shown by the yellow patches.

3.2.2 Magnetoresistance Measurements

The resistivity of the topological insulator samples was measured in the physical properties measurement system (PPMS, Quantum Design). The resistance was

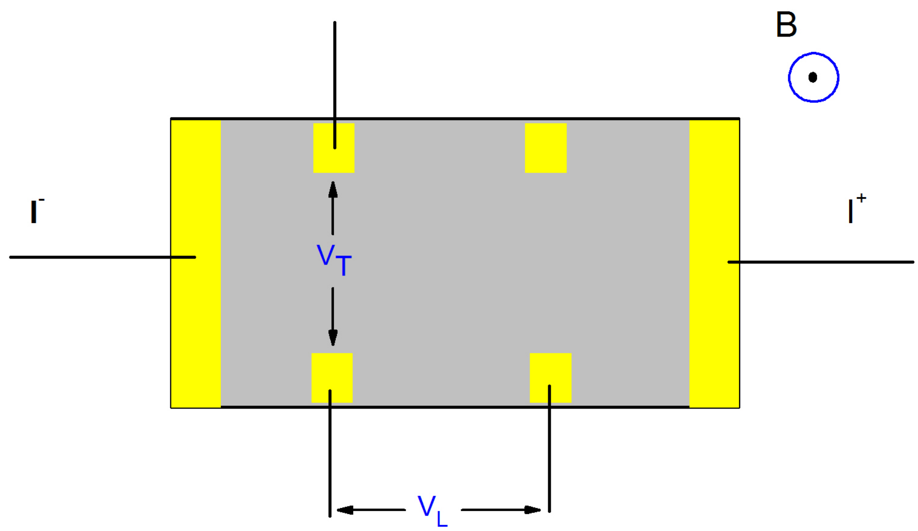

Figure 3.3: A sample geometry for measuring the longitudinal and Hall resistances.

measured from 300 K to 2 K. The sample was attached with GE - varnish on the rotator platform and then plugged onto the PPMS horizontal rotator as shown in Fig. [3.2.2]. The platform has 3 channels: channel 1 is used for the platform thermometer; 2 is used for the longitudinal resistance; and channel 3 is used for the Hall resistance measurements. The channel 2 provides the current for both the longitudinal and the Hall resistance measurements. The sample platform can be rotated by 360^o using a stepper motor attached on the top of the probe. The top part of the probe has a vernier dial which measures the angle of rotation of the sample platform with respect to the direction of applied magnetic field. At 0^o angle of rotation, the sample platform is horizontal with its surface facing the downward direction. Therefore, the applied magnetic field is always perpendicular to the platform surface at 0^o angle.

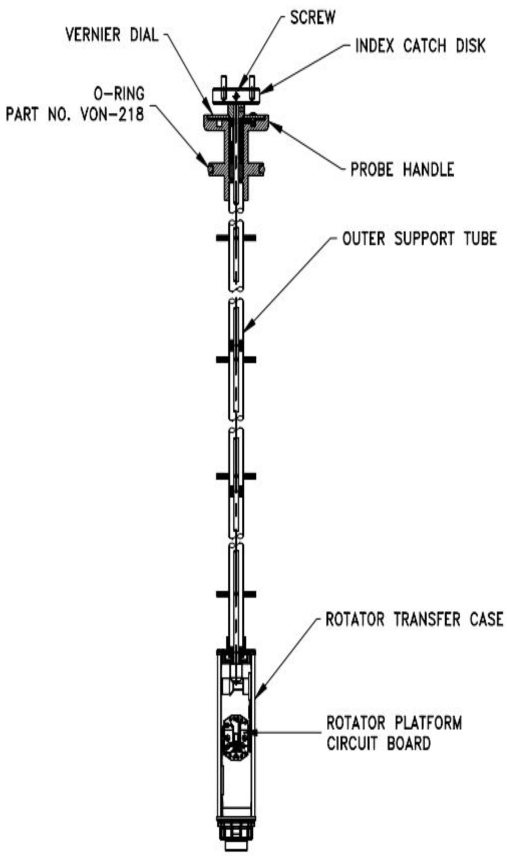

(a) A horizontal rotator probe.

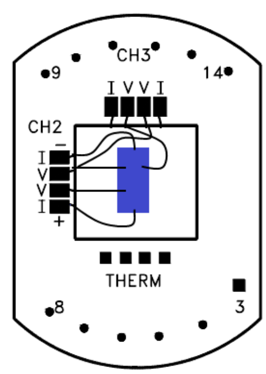

(b) A rotator platform.

Figure 3.4: (a) A horizontal rotator probe for resistivity and Hall measurements in the PPMS. (b) The wire connection for resistivity and Hall measurements, where the blue rectangle represents a sample.

The sample platform was always rotated in one direction in order to reduce the backlash error. The calibration of the polarity of charge carriers and any adjustment of the rotational angle were done using a Hall sensor. At 0^o angle, the positive slope of the Hall resistance indicates the presence of positive (hole) type of charge carriers and vice versa. A typical error bar in the angle of rotation is less than 3^o.

3.2.3 Magnetoresistance Measurements in Oxford Cryostat

The range of the magnetic field was extended to 13 Tesla using an Oxford cryostat. In order to conduct measurements at different angles, a rotator probe had to be built, calibrated and tested, as described below.

3.2.3.1 Probe Construction

The probe for the magnetotransport measurements in the Oxford cryostat is shown in Fig. [3.5]. This special probe has a facility to rotate a sample in a magnetic field. The rotation mechanism is attached at the bottom part of the probe. The bottom part of the probe consists of a hollow cylinder built by joining two circular discs with two walls as shown in Fig. [3.6]. A threaded plastic wheel is attached to one of the walls. A plastic scew with exact matching thread is attached against the rim of the wheel; so that the screw rotation moves the wheel. A small stainless steel rod (S1) rotates the plastic screw. Both the wheel and screw are made out of nylon plastic. A sample holder made out of copper is attached to the wheel. A cernox temperature sensor is attached on the back side of the sample holder to measure the temperature of the sample. The cernox temperature sensor was calibrated from room temperature to 1.9 K using the standard probe built in our lab. The plastic scew is rotated by a stepper motor attached on the top part of the probe as shown in Fig. [3.2.3.1]. The number of rotations is counted by a mechanical counter. The angle of rotation was calibrated by counting the number of turns need to rotate the plastic disc by 360^o as follows.

76 turns of the stainless steel rod (S1) = 360^o of the plastic wheel

1 turn of the stainless steel rod (S1) = 4.737^o of the plastic wheel

Similarly,

1 turn of the stainless steel rod (S1) = 360^o of the stepper motor

1 turn of the stainless steel rod (S1) = 4.737^o of the plastic wheel

Therefore,

1^o of the stepper motor = $4.737^o/360^o = 0.013^o$ of the plastic wheel

However, the smallest step of the stepper motor is 0.9^o. Hence,

0.9^o of the stepper motor = 0.012^o of the plastic wheel

Thus, the sensititivity of the angle of rotation of the sample platform is less than 0.2^o. This very high sensitivity is due to the very small step of angle of rotation of the stepper motor.

The middle part of the probe consists of a stainless steel tube with six copper radiation heat shields. Five pairs of twisted copper wires run from the sample holder to a 25 pins connector, which is attached on the top of the probe. A Lakshore LS336 and a linear resistance bridge LR-700 were used for temperature and electrical signal

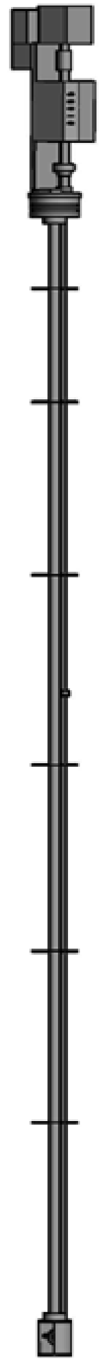

Figure 3.5: An AutoCAD design of the probe that fits in 16 Tesla Oxford cryostat. The top part consists of a stepper motor and a mechanical counter, the middle part has a stainless steel with heat shields made out of copper, and the buttom part is made out of brass cylinder.

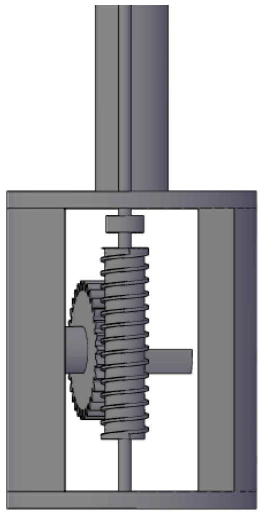

(a) AutoCAD drawing .

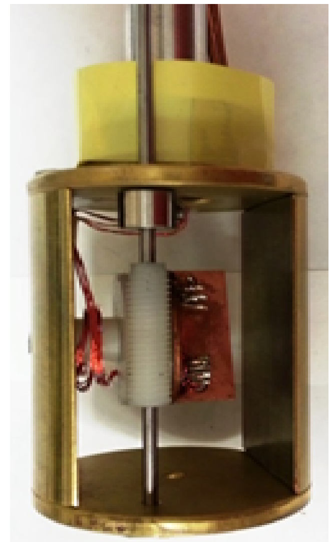

(b) A real picture.

Figure 3.6: The botton part of the probe that houses the rotational mechanism.

measurements, respectively. Fig. [3.8] shows the connection diagram for measuring temperature and electrical signals coming from the sample. Since the Hall resistance depends on the angle of rotation with respect to magnetic field, we tested the peformance of the probe by using a Hall sensor. It was found that the Hall resistance follows a $cos\theta$ dependence, where θ is the angle between the normal to the sample surface and the direction of magnetic field as shown Fig. [3.9], this step confirmed that the mechanism for rotation is behaving as expected.

3.2.3.2 Cooling the Cryostat

Figure [3.10] shows the Oxford cryostat in our laboratory. The Oxford cryostat consists of two vacuum jackets: an outer and an inner jacket. The outer vacuum jacket was pumped overnight with a turbo pump to a pressure lower than 10^{-4}

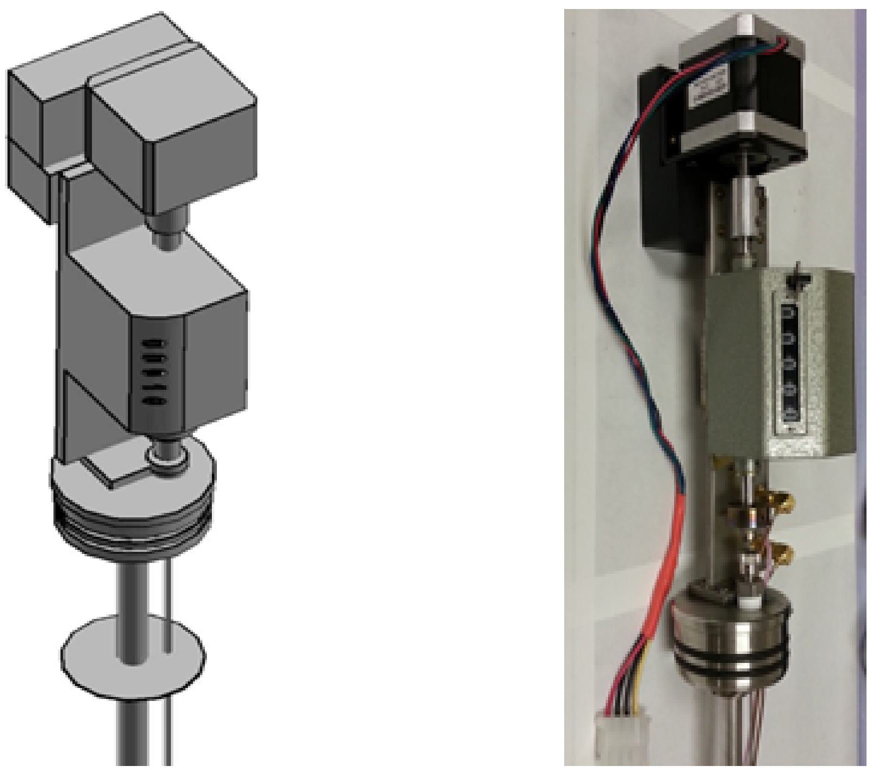

(a) AutoCAD Drawing. (b) A Real Picture.

Figure 3.7: The top part of probe that consists of a stepper motor and a mechanical counter. The stepper motor is driven by an external electrical control unit.

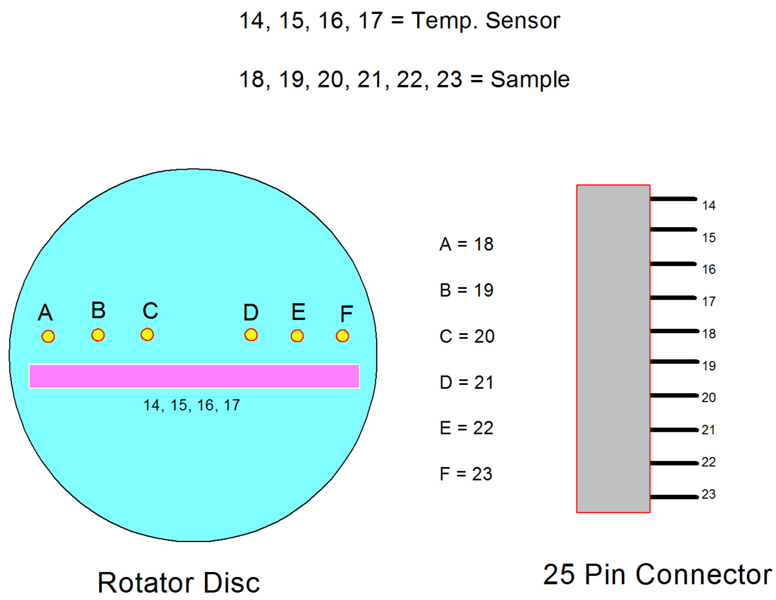

Figure 3.8: The connection diagram for the probe. Pin numbers (14, 15, 16, 17) and (18, 19, 20, 21, 22, 23) in 25 pin connector are used for the cernox temperature sensor and samples, respectively.

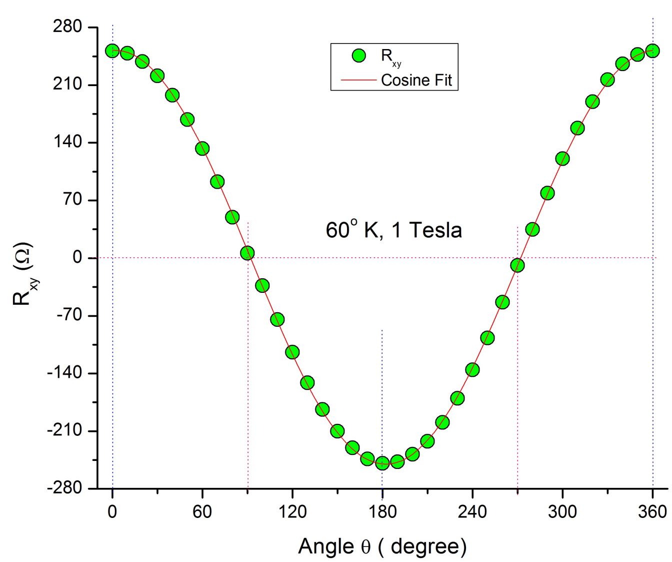

Figure 3.9: Hall resistance as a function of the angle of rotation. The green circles show the measured Hall resistance and solid red line is the cosine fit. The measurment has been conducted at 60^o K in the presence of a 1 Tesla magnetic field.

mbar. Then, the variable temperature insert (VTI) was removed using a crane and the helium dewar was pre-cooled using liquid nitrogen. The cryostat was filled with liquid nitrogen overnight. The inner vacuum jacket was also evacuated using the turbo pump. On the next day, the liquid nitrogen was pumped out using a nitrogen hose. It is very important to note that there should be no liquid nitrogen left in the cryostat. Otherwise, it is impossible to condense helium. Once all the liquid nitrogen was pumped out, the VTI was inserted back into the cryostat. Then, we started filling helium through helium filling port. Initially, the flow of helium was kept low to cool down the cryostat slowly. Once the cryostat was cool enough to condense helium, the rate was increased. The condensation of helium was measured using the helium level meter. It usually takes 70 - 80 liters of helium for the first fill. So, it is recommended to use a 100 L tank for the first fill.

3.2.4 Experimental Set up in National High Magnetic Field Laboratory

High field measurements were perfomed at the National High Magnetic Field Laboratory (NHMFL), with fields up to 35 Tesla. Longitudinal and Hall resistances were measured using Oxford lock-in amplifiers. AC current of 1 mA was passed through the sample at a certain frequency using a Keithley source meter. The longitudinal and Hall resitances were measured in channel 1 and 2 of the lock-in amplifier respectively. The sample was mounted on a rotating platform which allowed for positioning the sample at different angles with respect to the magnetic field. The

Figure 3.10: The Oxford Cryostat with 13 Tesla superconducting magnet in our lab.

(a) Toploading ^{3}He Cryostat.

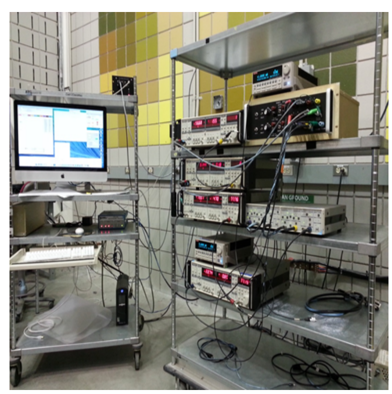

(b) Lock-in amplifier measurement setup.

Figure 3.11: Experimental Set up in the National High Magnetic Field Laboratory.

platform, mounted in a ^{3}He cryostat (Oxford), was inserted into the 32 mm bore of a resistive magnet with a maximum field of 35 Tesla. Fig. [3.12] is a sketch of the 35 T resistive magnet system. The magnet is comprised of an assembly of Bitter plates, named after American physicist Francis Bitter. A Bitter plate is a circular conducting metal plate having several holes on it as shown in Fig. [3.13]; these plates are then stacked in a helical configuration with insulating spacers between. The current flows in a helical path through the plates and this design of stacked plate magnet also helps to withstand the enormous outward mechanical pressure due to the Lorentz force. Also, this design allows for cold water to pass easily through the holes and carry away the heat produced due to resistive heating. The magnet was operated always in sweeping mode with a rate of 2 Tesla per minute in order to minimize electric power consumption.

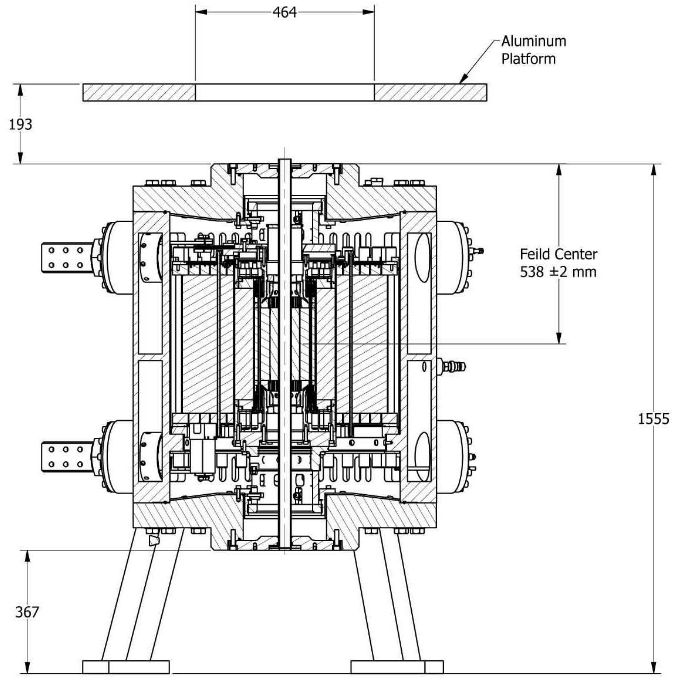

Figure 3.12: A sketch of 35 Tesla magnet design in NHMFL, Tallahassee, Florida. The dimensions are measured in mm. The figure is adapted from NHMFL website.

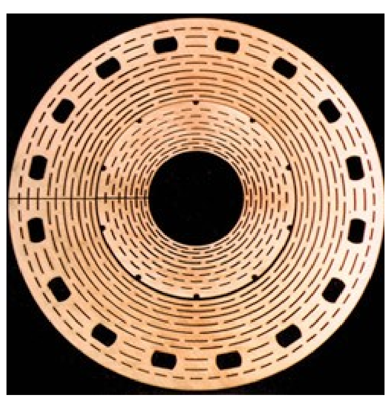

Figure 3.13: Resistive magnets are made of metal Bitter plates stacked into a coil.

3.2.5 Seebeck Coefficient Under Magnetic Field

The Seebeck coefficient of topological single crystals were measured in a magnetic field up to 7 Tesla. We designed a special puck that can be fitted in PPMS (Quantum Design). A sinusoidal temperature gradient at a certain frequency is created and the sinusoidal thermovoltage of the same frequency is measured across the sample. The computer program performs a non-linear curve fitting to the sinusoidal thermovoltage to calculate its average amplitude. This non-linear curve fitting also helps to reduce the noise level in the measurement. By taking the ratio of the amplitude of the thermovoltage (ΔV) to the amplitude of the temperature gradient (ΔT), we can calculate Seebeck coefficient i.e.

$$S = \frac{\Delta V}{\Delta T}. \tag{3.1}$$

This technique is similar to a lock-in technique where the signal of only desired frequency is measured. That is why this measurement is more precise than a one heater or a direct current (dc) technique to measure the Seebeck coefficient.

A sample was placed across two sapphire plates (as shown in Fig. [3.15]). A sinusoidal temperature gradiant of amplitude 0.25 K was created across the sample using two thin film heaters H_1 and H_2. A sinusoidal current was applied to both heaters using Keithley 220 programmable current source with a 90^o phase offset. Consider $I_1 = I_0 Sin(\omega t)$ and $I_2 = I_0 Cos(\omega t)$ to be the current through the first heater and second heater, respectively, then total power dissipated on the sample

$$P = I^2 R = I_1^2 R + I_2^2 R = I_0^2 R \tag{3.2}$$

is constant with time. This tells that the average sample temperature is constant.

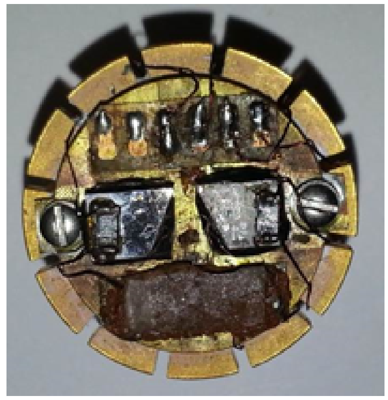

Figure 3.14: A thermoelectric power puck. Two black rectangular plates are saphhire plates which are heated by individual thin film heater attached on them.

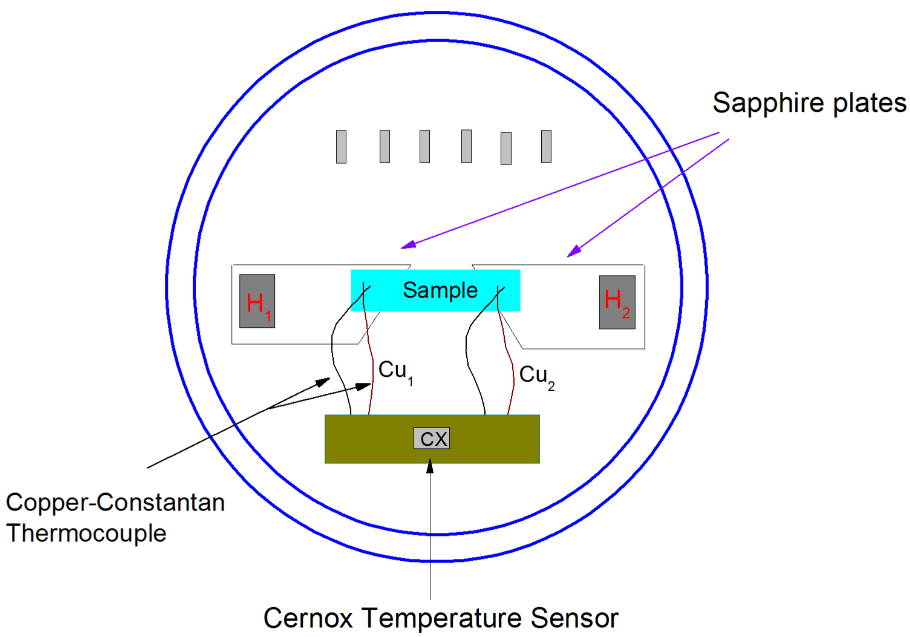

Figure 3.15: A sketch of the front panel of the thermoelectric power puck.

The temperature measured by a cernox was used as the reference temperature to the Copper-constantan (Cu-Con) thermocouple. Two Cu-Con thermocouples measured temperatures at two ends of the sample for the temperature difference, as well as the ac thermovoltage at either ends of the sample. A HP34420A nanovoltmeter was used to measure the voltage across the copper wires Cu_1, Cu_2 and sample i.e.

$$V = V_{Cu_1} + V_{sample} - V_{Cu_2}. \tag{3.3}$$

The negative voltage across Cu_2 wire is because of negative temperature gradient with respect to the reference temperature. In order to get the real signal from the sample, we have to know the voltage across the copper wires Cu_1 and Cu_2. Since a superconductor has zero a Seebeck coefficient at its superconducting state, we have used Yttrium Barium Copper Oxide (YBCO), a high temperature superconductor to measure the Seebeck coefficient of the copper wires. However, the high temperature calibration (above 90 K) of the copper wires were done using a high purity lead. The thermopower of high purity lead is known well and its value was substracted to calculate the thermovoltage across copper wires.

The magnetic field dependence of thermocouple was done by creating a constant temperature in one of thermocouples. A dc current was applied to one of the heaters that creats a temperature gradient across the thermocouple. The current was adjusted such that a constant temperature gradient of 0.5 K is maintained. Similarly, the magnetic field dependence of thermovoltage across the copper wires was carried out using a Manganin foil. The Manganin foil was used as a sample and its magneto-thermovoltage was substracted to evaluate the magneto-thermovoltage of the copper wires.

Chapter 4

Results

In this chapter, I will present the main findings of the present work. We have carried out a detailed magnetotransport study on $Bi_2Se_{2.1}Te_{0.9}$, Bi_2Te_3, and Sb_2Te_2Se metallic topological insulators to investigate the possible presence of topological surface states. All magnetotransport experiments are carried out at low temperatures (5 K to 300 mK). After detailed analyses, we concluded the existence of topological surface states in metallic topological samples and the possible reasons for their existence. In $Bi_2Se_{2.1}Te_{0.9}$ and Sb_2Te_2Se samples, we found that if the Fermi energy is low enough that it cuts the valence band in the band structure, it allows us to study the surface states at low magnetic field. Our theoretical arguments are further supported by the high field data up to 35 Tesla at the national high magnetic field lab, Tallahassee, Florida. Similarly, angle dependence of weak antilocalization in Bi_2Te_3 samples proved the dominance of topological surface states in the samples having low bulk carriers.

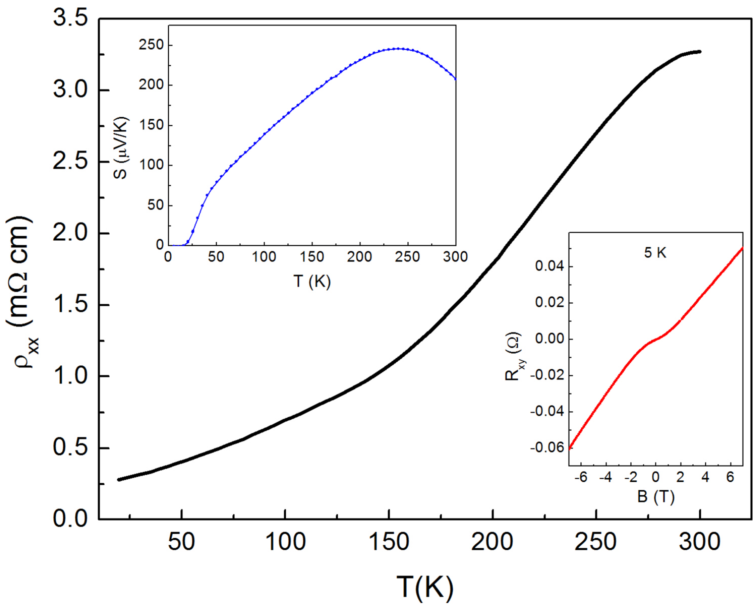

Figure 4.1: Temperature-dependence of resistivity (ρ_{xx}) of a $Bi_2Se_{2.1}Te_{0.9}$ single crystal. The lower right inset shows Hall data at 5 K. The upper left inset displays the temperature dependence of the thermoelectric power.

4.1 $Bi_2Se_{2.1}Te_{0.9}$ Single Crystal

4.1.1 Resistivity, Hall and Seebeck Coefficient

We have selected a single crystal of $Bi_2Se_{2.1}Te_{0.9}$ and sputtered six gold contacts on its surface as explained in the method section. The temperature-dependence of the resistivity is metallic as shown in Fig. [4.1]. Hall measurements reaveled that the charge carriers are p-type, as shown in lower inset Fig. [4.1]. The bulk carrier density is found to be $N = 2\times10^{18}$ cm^{-3} at 5 K, consistent with the metallic character of the bulk resistivity. The positive and large thermoelectric power has further confirmed the p-type nature of the carriers, as shown in the upper left inset to Fig. [4.1].

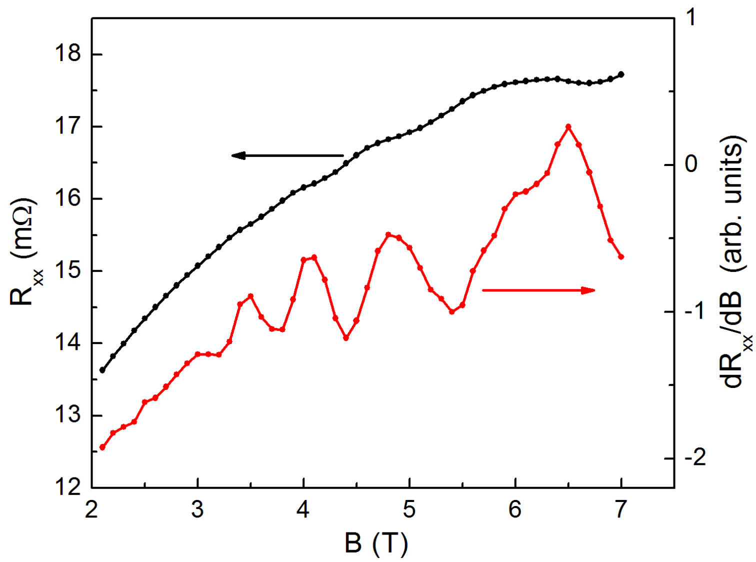

Figure 4.2: Magnetic field dependence of the resistance of $Bi_2Se_{2.1}Te_{0.9}$ (black, upper curve) at 2 K. The red (lower) curve shows the SdH oscillations in the derivative dR_{xx}/dB.

4.1.2 Shubnikov de Haas Oscillations

The magnetoresistance $R_{xx}(B)$ of $Bi_2Se_{2.1}Te_{0.9}$ single crystal is shown in Fig. [4.2]. The magnetic field was applied along c-direction of the sample. Small quantum oscillations can be seen above 3 Tesla magnetic field, known as Shubnikov de Haas (SdH) oscillations. These oscillations become more clear in the derivative of R_{xx} as shown in the right scale of Fig. [4.2]. The quantum oscillations that we have observed can be of either surface or bulk origin. In order to identify the possible origin of the quantum oscillations, we have measured the magnetoresistance at different angles of rotation of the sample with respect to B. The SdH oscillations maxima and minima positions do not change when the derivatives dR_{xx}/dB are plotted as a function of the inverse of the normal component of applied magnetic field $1/B_\perp$ as shown in

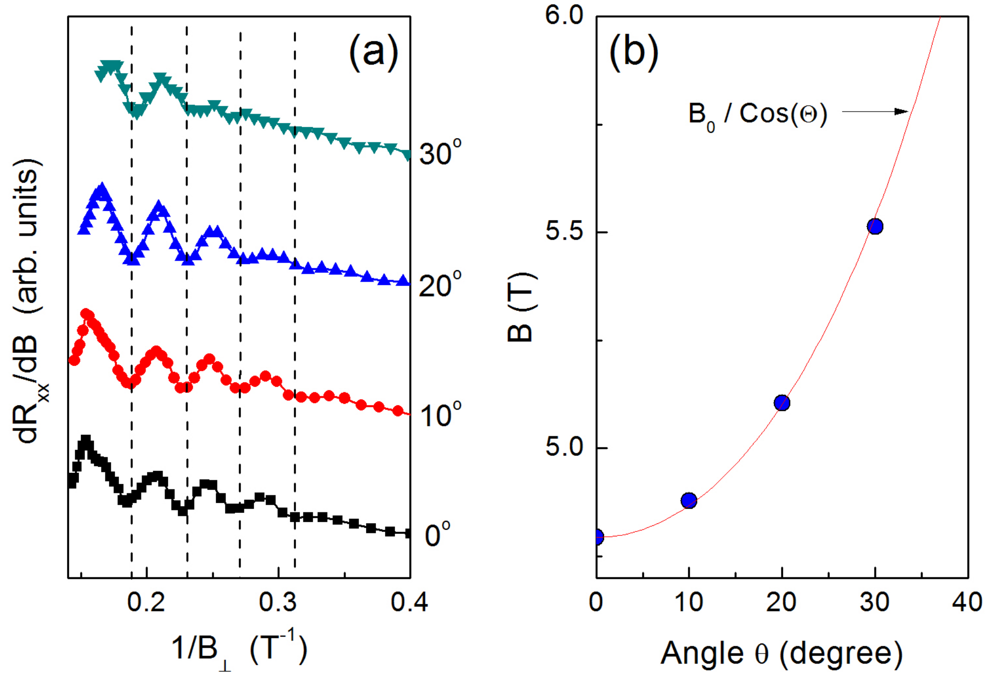

Figure 4.3: (a) dR_{xx}/dB as a function of the inverse perpendicular component $1/B_{\perp}$=$1/Bcos\theta$, demonstrating the scaling expected for surface conduction channels. (b) Plot of the field position of a maximum of dR_{xx}/dB corresponding to n=5.5 in the Landau level fan diagram. The line shows the $1/cos\theta$ scaling.

Fig. [4.3 (a)], where $B_{\perp}$=$Bcos\theta$ is the normal component of magnetic field with θ is the angle between the normal to the sample surface and the direction of B. This shows that the quantum oscillations we observed here depends only on the normal component of B, indicating they are possibly originated from topological surface states. The amplitude of the oscillations decreases quickly at higher angles and the SdH oscillations can no longer be resolved. The angle dependence of one extremum is shown in Fig. [4.3 (b)] and it follows the expected $1/\cos\theta$ scaling for surface states. This is taken as evidence that the quantum oscillations arise from the topological surface states [14].

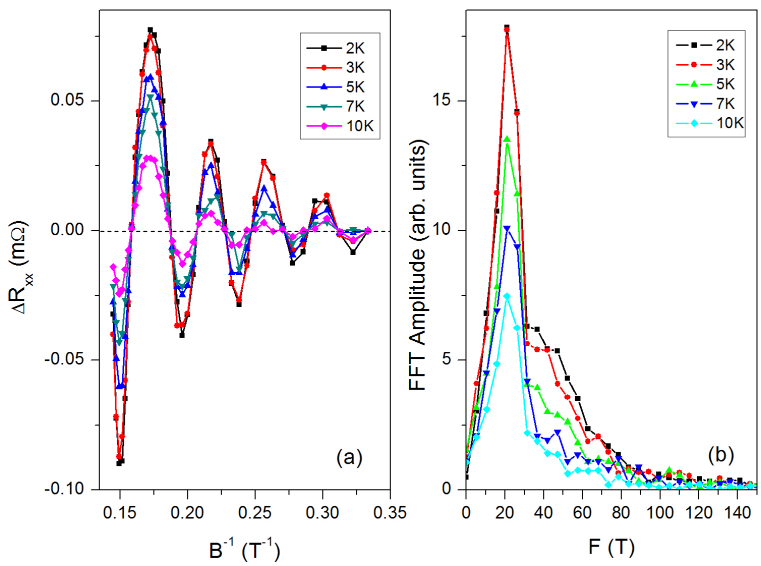

Figure 4.4: (a) Oscillatory part of the magnetoresistance R_{xx} (B) at different temperatures vs inverse magnetic field. The field is perpendicular to the crystals surface. (b) Fourier transform of the data from (a).

4.1.3 Frequency Analysis

Figure [4.4] shows the oscillations at different temperatures, obtained after substracting the smooth polynomial background. The oscillations are periodic in $1/B$ and the amplitude decreases with an increase in temperature; however, the frequency remains unchanged as shown in Fig.[4.4 (b)]. Besides the major sharp peak at a frequency of $F_1 \approx 23$ T, there is a weak shoulder around a frequency $F_2 \approx 50$ T. This could indicate a small contribution from a higher frequency, as observed in other topological systems with complex Fermi surfaces [39][40][41]. However, the effect is relatively minor and disappears with increasing temperature.

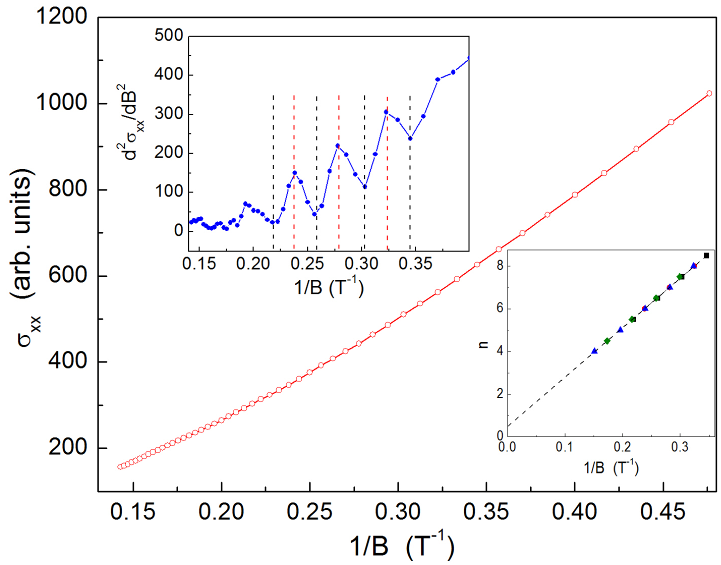

Figure 4.5: Field dependence of conductivity σ_{xx} (B) (red curve). Upper left inset: second derivative $d\sigma_{xx}^2/dB^2$ vs $1/B$. The vertical dashed lines mark the positions of the maxima and minima of the quantum oscillations. Lower right inset: Landau level fan diagram with linear extrapolation (dashed line) to $1/B = 0$.

4.1.4 Berry Phase

Further evidence of the origin of SdH oscillation from the topological surface states can be provided from the value of the Berry phase β. It can be evaluated from Landau level fan diagram [5]. Here the integer n, denoting the n^{th} Landau level, is plotted as a function of the position of maxima and minima of the quantum oscillations, $1/B_{max}$ and $1/B_{min}$. The value of n_0, obtained by a linear extrapolation of $1/B \to 0$, defines the value of the Berry phase in units of 2π. $n_0 = 0.5$ $(\beta = \pi)$ is expected for Dirac particles. As pointed out by Ando [5], however, using resistivity ρ_{xx} data can lead to a deviation from the true value of β, and conductivity (σ_{xx}) data should be evaluated instead.

We have evaluated the conductivity using the formula $\sigma_{xx} = \rho_{xx}/(\rho_{xx}^2 + \rho_{xy}^2)$ from ρ_{xx} and ρ_{xy} measured at 2 K. Figure [4.5] shows the conductivity as a function of $1/B$. The quantum oscillations are not visible in σ_{xx} and its first derivative. However, the oscillations are clear in its second derivative as shown in upper inset to Fig. [4.5]. Assigning integer values to the positions of minima and half integer values to the maxima in $d^2\sigma_{xx}/dB^2$ vs $1/B$ graph, we have plotted a Landau level fan diagram in the lower inset to Fig. [4.5]. The positions of the extrema of $d^2\sigma_{xx}/dB^2$ are in perfect agreement with the extrema of ΔR_{xx} shown in Fig. [4.4 (a)]. The values from ΔR_{xx} are included as blue triangles and green diamonds in the Landau level fan diagram of Fig. [4.5]. The linear extrapolation $1/B \to 0$ in the Landau level fan diagram yields $n_0 = 0.45 \pm 0.04$, consistent with the Dirac nature of the particles, and a slope of $F = 23.3$ T, in good agreement with the characteristic frequency of the SdH oscillations determined from Fig. [4.4 (b)].

4.1.5 Lifshitz Kosevich Theory

The characteristic angle dependence of quantum oscillations and the value of Berry phase show that the SdH oscillations in the transport data are predominantly caused by the topological surface states of $Bi_2Se_{2.1}Te_{0.9}$. Therefore, it is quite interesting to know the physics of why there is a small interference from the bulk conduction channel in p-type metallic topological insulators. For that, we have calculated many physical parameters characterizing the quantum oscillations by using the Lifshitz Kosevich (LK) theory. The frequency of oscillations, $F = 23.3$ T, corresponds to a Fermi momentum $k_F = 2.7 \times 10^6$ cm^{-1} according to the Onsager relation

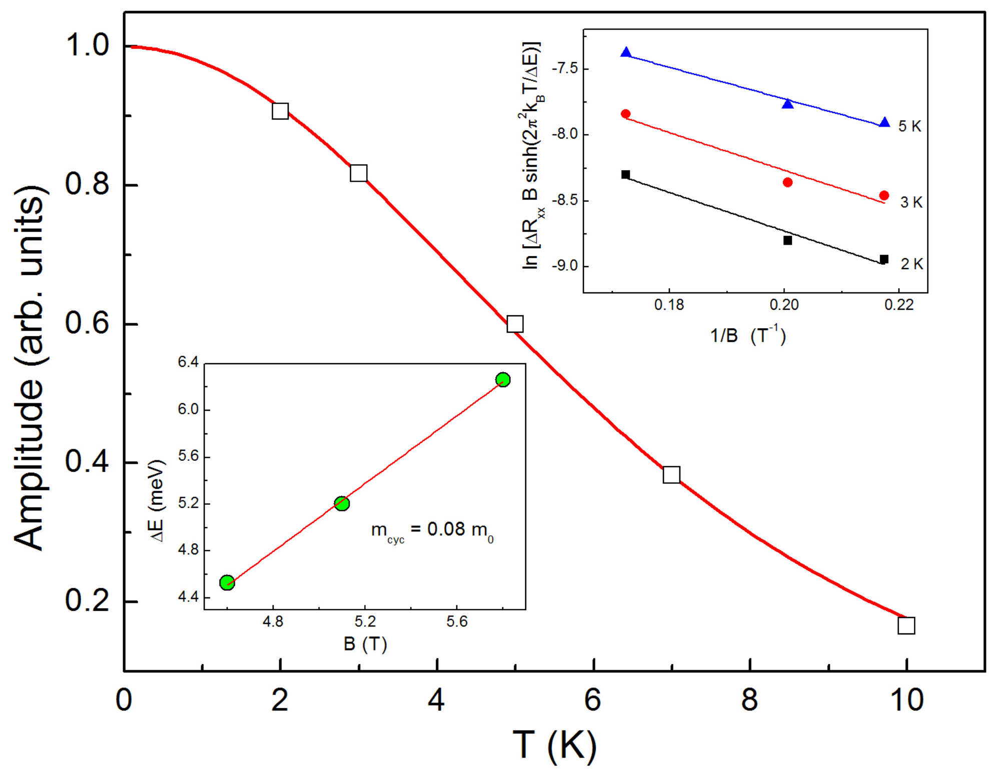

Figure 4.6: Temperature dependence of the amplitude of the SdH oscillation (ΔR_{xx}) at 4.6 T. The red line represents the fit to the equation for R_T. Lower left inset: ΔE vs B. Upper right inset: Dingle plot used to determine the Dingle temperature T_D and the carrier lifetime τ.

$F = 1/(2e)k_F^2$. For a circular Fermi surface, this value of k_F results in a surface carrier density of $n_{2D} = k_F^2/4\pi = 5.8 \times 10^{11}$ cm^{-2}. The value of k_F is slightly smaller than those obtained in other topological insulators with electron as well as hole carriers at the surface [14][42][43][39], indicating the closer proximity of the Fermi level to the Dirac point in our sample.

According to the LK theory, the temperature dependence of the amplitude of the SdH oscillation is given by $\Delta R_T = e^{-\lambda_D}\lambda(T/B)/sinh[\lambda(T/B)]$, where λ_D is defined below, $\lambda(T/B) = [2\pi^2 k_B T/(\Delta E_N(B))]$ and the Landau level spacing $\Delta E_N(B) = \hbar eB/m_{cyc}$. $\Delta E_N(B)$ can be determined for different magnetic field values from $\Delta R_{xx}(T)$, as shown in Fig. [4.6] for $B = 4.6$ T. The lower left inset in Fig. [4.6] displays the linear dependence of E_N on B. From the slope, the cyclotron mass is determined as $m_{cyc} = 0.08m_0$, with m_0 the bare electron mass. With the linear dispersion relation for Dirac fermions, $v_F = \hbar k_F/m_{cyc}$, the Fermi velocity of the surface carriers is obtained as $v_F = 3.9 \times 10^7$ cm/s.

Another factor in the LK theory is the Dingle factor $e^{-\lambda_D}(\lambda_D = 2\pi^2 k_B T_D/\hbar\omega_c)$, where ω_c is the cyclotron frequency, which accounts for the life time τ of the surface carriers through the Dingle temperature, $T_D = \hbar/(2\pi k_B \tau)$. T_D is determined, following the standard Dingle analysis, from the slope of the semilogarithmic plot shown in the upper right hand inset of Fig. [4.6]. With the estimated value $T_D = 12$ K, the surface carrier lifetime is $\tau = 1.0 \times 10^{-13}$ s, corresponding to a mean free path of $l_{2D}= v_F\tau = 39$ nm and a surface carrier mobility of $\mu_{2D} = (el_{2D})/(\hbar k_F) = 2200$ $cm^2/(VS)$. These values are comparable with other topological systems [44][45].

4.1.6 Discussion

From the angle dependence of the quantum oscillations and the Berry phase calculations, we have proved the existence of topological surface states in $Bi_2Se_{2.1}Te_{0.9}$ despite the metallic conductivity from bulk carriers, which deserves a more detailed discussion. The relatively small value of k_F indicates that the Fermi energy in our sample is lower than in other Bi-Se-Te based compounds. The estimated Fermi energy $E_F = 69$ meV is significantly closer to the Dirac point than E_F values found, for example, in Bi_2Te_3 [14], Bi_2Te_2Se [43], or in Sb-doped Bi_2Se_3 [42]. With this low value, E_F cuts through the maxima of the valence band in the band structure, as sketched in Fig. [4.7]. It is important to note that the valence band has two maxima at a finite momentum whereas the conduction band shows its minimum at $k = 0$ [14] [43].

The question arises as to why the bulk states do not produce SdH oscillations within the field range of the current experiment. The peculiar shape of the valence band with the Fermi energy cutting through the two maxima as well as the Dirac cone requires a larger Fermi momentum k_F^{bulk} and a larger area of the Fermi surface to observe bulk SdH oscillations. The corresponding oscillation frequency $F = (\hbar/2e)k_F^2$ will be significantly higher. The magnetic field needed for the n^{th} Landau level of the bulk carriers to cross the Fermi energy and to impact the conductivity is now much larger, dictated by the condition $F/B_n - \beta = n - 1$. Therefore, the quantum oscillations of bulk carriers for low n are shifted to higher fields, beyond the range of the current measurements. Only bulk oscillations at larger Landau level indices could be observed at smaller fields, however, these oscillations are naturally attenuated,

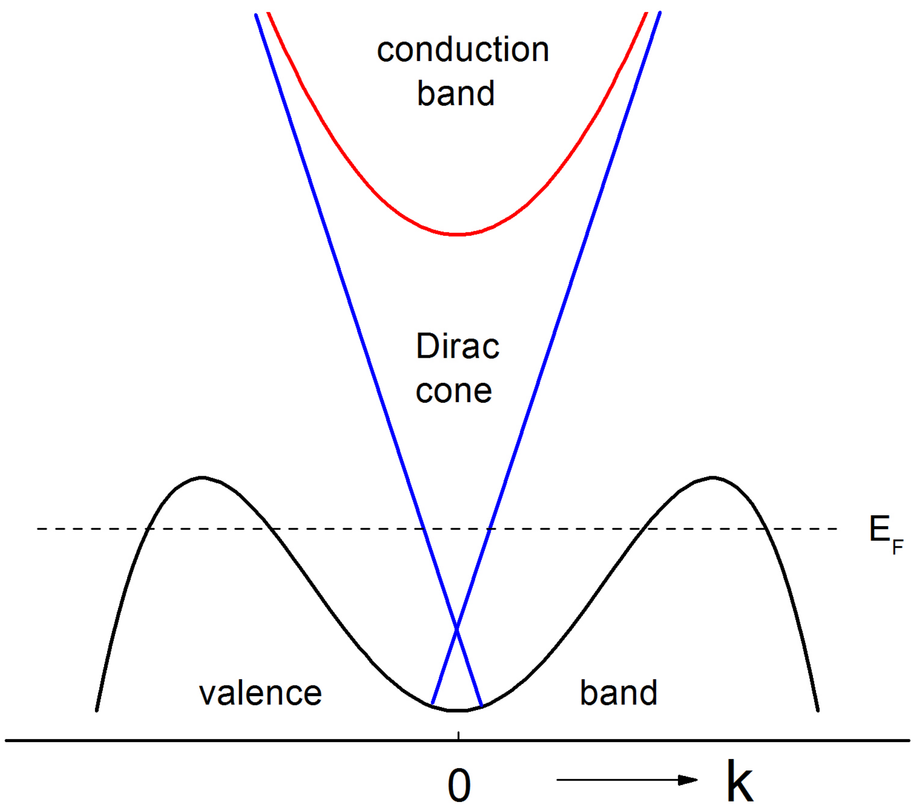

Figure 4.7: Schematic of the band structure of $Bi_2Se_{2.1}Te_{0.9}$. The Fermi energy is low enough to cut through the maxima of the valence band, resulting in bulk holelike transport properties.

according to the LK theory. This explains why in the present data (Figs. 4.2 - 4.4) the topological surface states dominate the oscillations of the electrical transport properties. The observations discussed above open additional possibilities to study topological effects in Bi-Te-Se type compounds when the Fermi energy is close to or even cutting through the valence band.

It should be noted that the above discussion only applies if the Fermi energy is low and close to the Dirac point and the valence band. For higher E_F, cutting through the bottom of the conduction band, the above argument is not valid. Since the conduction band has its minimum at $k = 0$, the related Fermi momentum of the bulk carriers is of the same magnitude as that of the Dirac states. In this case, the bulk transport is electronlike (metallic) and the SdH oscillations from bulk and surface states will be equally present in the whole range of magnetic fields. The quantum oscillations from bulk states are frequently dominating [14].

4.2 Extending Magnetic Field Range

In the previous section, we have argued that the observation of a second frequency F_2 is possibly due to interference from the bulk states. However, as the frequency F_2 is almost twice the value of the first frequency F_1, it could also be interpreted as the second harmonic of F_1. In order to resolve the origin of the F_2, we extended the range of the magnetic fields to 13 Tesla. We have selected another fresh single crystal of $Bi_2Se_{2.1}Te_{0.9}$ from the same batch and sputtered six gold contacts for resistivity and Hall measurements. From the preliminary characterization of the sample up to 7 T

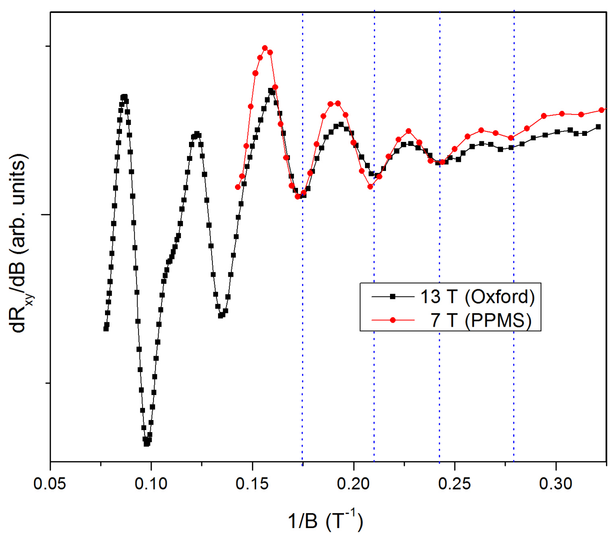

Figure 4.8: Comparison of quantum oscillations measured in PPMS (Quantum Design) and those measured in an Oxford cryostat. The range of magnetic fields are 7 and 13 Tesla in PPMS and Oxford cryostat, respectively.

in the PPMS, the sample is found to be metallic and p-type, similar to the previous sample [46]. The bulk carrier density is found to be $N = 7 \times 10^{17}$ cm^{-3} from the Hall measurements. Also, the existence of surface states is confirmed from both the angle dependence of quantum oscillations and Berry phase calculation. Figure [4.8] shows the comparison of quantum oscillations measured in PPMS and Oxford cryostat at 5 K. With the increase of magnetic field to 13 T, more quantum oscillations are observed. However, there is a slight mismatch in the positions of quantum oscillations measured in Oxford cryostat compared to those measured in PPMS. This may be caused by the sweeping drive mode of magnet that cause the loss of the precision of the measurements. There appears to be a possible interference of the second frequency at higher fields. This can be observed clearly in FFT spectrum as shown in Fig. [4.9]. The position of the first frequency F_1 does not change, however, the

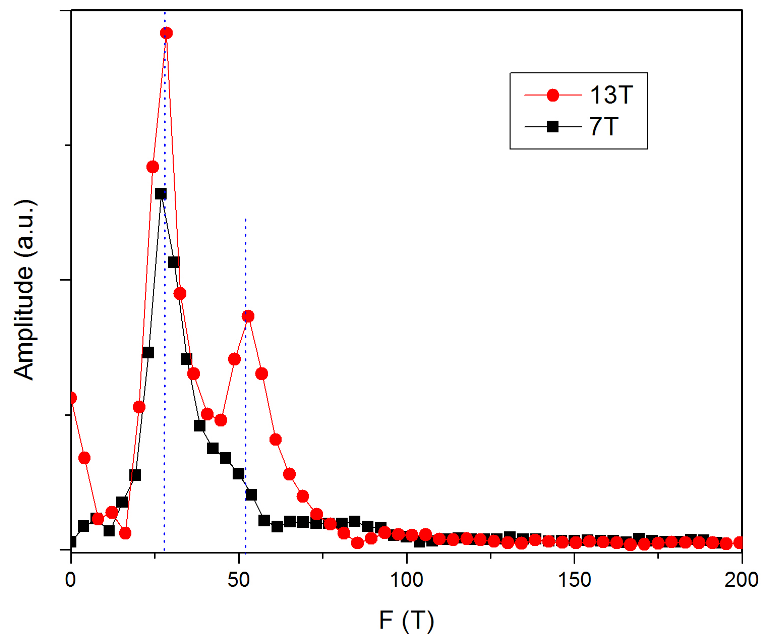

Figure 4.9: Fourier transform of quantum oscillations shown in Fig. [4.8].

second frequency F_2 becomes more prominent upon an increase in magnetic field. This result is consistent with our previous theoretical argument [46].

The amplitude of F_2 is found to be weaker at higher angle of rotation of the sample with respect to magnetic field direction. That is why we could not study the angle dependence of F_2 to investigate its possible origin. Hence we have extended the measurements even further, to 35 T in National High Magnetic Field Laboratory, Tallahassee, FL.

4.3 Measurements in National High Field Lab

In this work, another freshly cleaved piece of p-type metallic $Bi_2Se_{2.1}Te_{0.9}$ single crystal was selected and used for magnetoresistance measurements in the magnetic

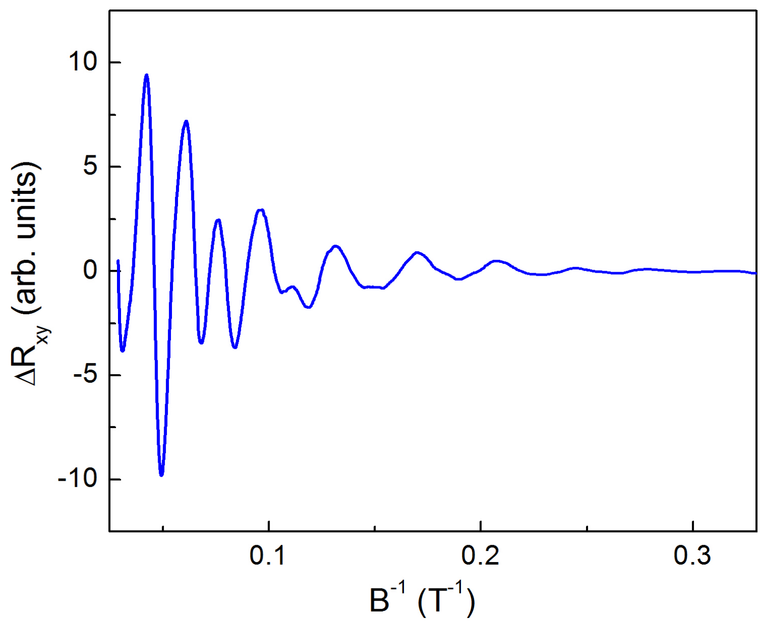

Figure 4.10: Shubnikov-de Haas oscillation of the transverse magnetoresistance of $Bi_2Se_{2.1}Te_{0.9}$. The oscillatory part ΔR_{xy} is plotted versus the inverse field.

field range up to 35 Tesla. The sample was metallic and carrier density was found to be 1.3 $\times 10^{18}$ cm^{-3} from the Hall measurement. This bulk carrier density is reasonable agreement to the previous single crystal of similar comosition [46]. We have found that SdH oscillations from bulk carriers dominate at higher magnetic field but are attenuated at lower fields. This allows us to separate bulk and surface states, determine the relevant parameters, and explain the interference and possible separation of surface and bulk quantum oscillations.

4.3.1 Shubnikov-de Haas Oscillations

Figure [4.10] shows the SdH oscillations of R_{xy} obtained after substracting the smooth polynomial background. The measurements were conducted with the magnetic field perpendicular to the large face of the crystal (a $\perp$ b plane in the hexagonal system). The quantum oscillations originate from the quantization of Landau levels in strong magnetic field and are periodic in $1/B$. However, it is obvious from Fig. [4.10] that the data cannot be described by an oscillation with one single frequency only, but rather by a superposition of different frequencies. This is confirmed by analyzing the Fourier transform of the data shown in Fig. [4.10].

Two frequencies, $F_1 \approx 26$ Tesla and $F_2 \approx 55$ Tesla, dominate the oscillating behavior of R_{xy}. Since F_2 is nearly twice F_1, both frequencies could be the first and second harmonic of the same oscillation, as observed in other compounds [39][40][47][48]. However, the relative weight of the oscillations with F_1 and F_2 strongly depends on the magnetic field range, which rules out the possibility of F_2 being simply the second harmonic of F_1. The SdH oscillation with the lower frequency F_1 dominates in the low-field range whereas the higher frequency F_2 is stronger at higher magnetic fields. This is demonstrated in Fig. [4.11], where the Fourier transform of the data is shown in Fig. [4.10] for various field ranges with the cutoff fields indicated in the figures. In the low-field range, B $<$ 5 Tesla, the FFT transform exhibits only one peak at frequency F_1 [Fig. 4.11(a)]. This is similar to and consistent with the earlier work that was limited to magnetic fields below 7 Tesla [46]. With increasing magnetic field, a second peak at F_2 develops [Fig. 4.11(b)] and for fields up to 15 tesla both peaks have about the same amplitude [Fig. 4.11(c)].

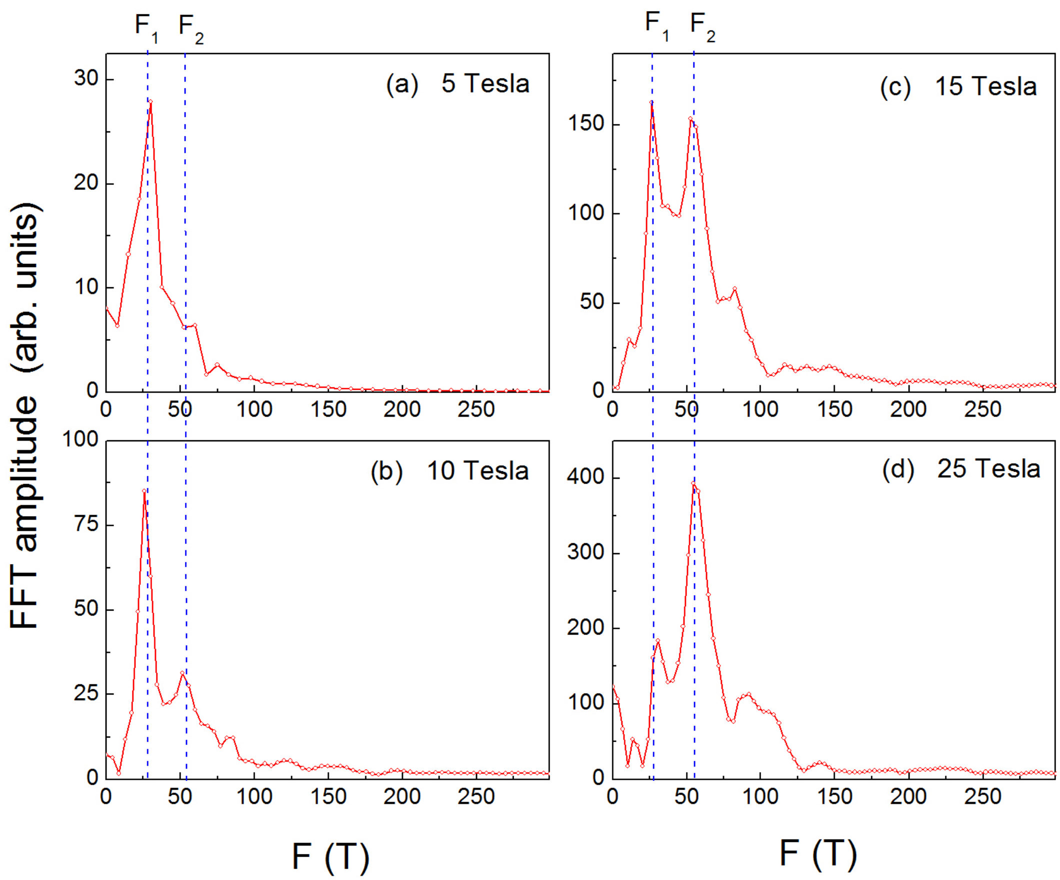

Figure 4.11: Fourier transform of ΔR_{xy} in different field ranges. The cutoff field is indicated in the graphs. The SdH oscillations with frequencies F_1 and F_2 are dominant at low and high magnetic fields, respectively.

With further increasing field, the F_2 peak becomes dominant [Fig. 4.11(d)]. The development of the two peaks shown in Fig. [4.11] prove that F_1 and F_2 characterize SdH oscillations of different origin. In our previous communication, we have shown that the low-frequency oscillation (F_1) arises from topological surface states, but the origin of the second frequency observed at higher fields is not clear. It appears conceivable to attribute the F_2 frequency to bulk SdH oscillations, as conjectured

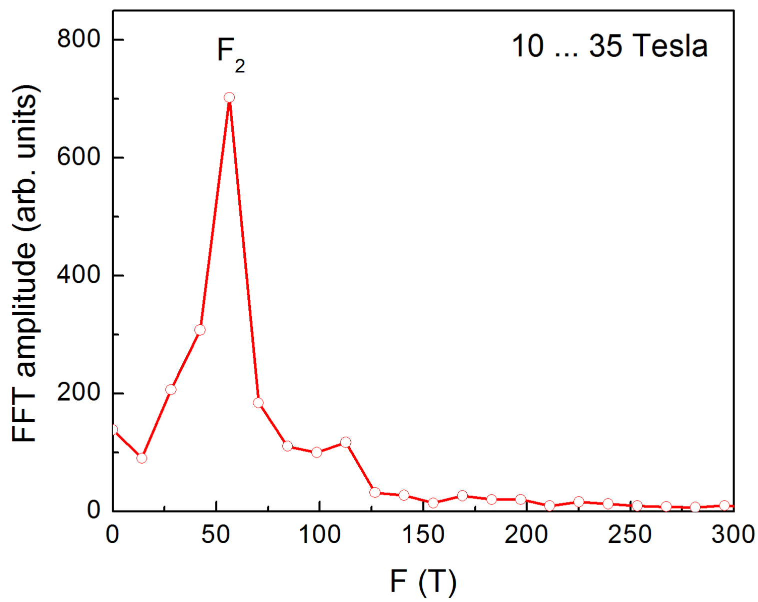

Figure 4.12: Fourier transform of ΔR_{xy} in the high-field range, between 10 and 35 Tesla. Only one peak is observed at frequencyF_2.

earlier [46]. To study the properties of the F_2 oscillation it has to be resolved separately, without the interference from the surface state oscillations (F_1). This can be achieved by analyzing the high-field data above 10 Tesla. Figure [4.12] shows that the FFT transform of the data above 10 Tesla exhibits only one pronounced peak at frequency F_2, i.e. the contribution from surface oscillations is largely eliminated.

4.3.2 Angle Dependence of SdH Oscillations

SdH oscillations from bulk and surface states can be distinguished by measuring the dependence on the angle with respect to the magnetic field direction. Surface oscillations of ΔR_{xy} or ΔR_{xx} are expected to be periodic if plotted as function of the inverse normal component, $1/\mathrm{B}_\perp$, of the field with respect to the surface. If the field

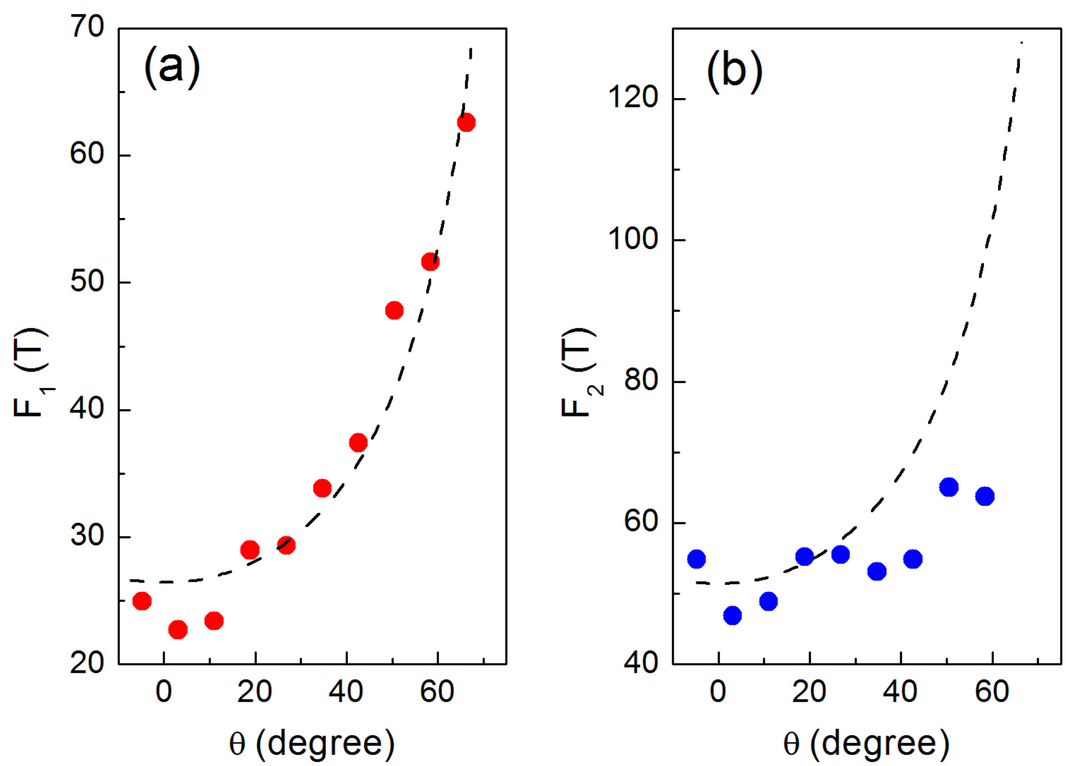

Figure 4.13: Angle dependence of the SdH oscillation frequencies F_1 (a) and F_2 (b). Only F_1 follows the $1/\cos(\theta)$ scaling for surface conduction (dashed line).

angle θ to the normal of the surface changes, the position of the oscillation frequency follows a $1/\cos\theta$ scaling, due to the strictly two-dimensional character of the surface conduction [48]. For bulk conduction, however, the SdH frequency will not follow the $1/\cos\theta$ scaling, but it may still show a minor angle dependence if the Fermi surface geometry is anisotropic [43].

The angle dependent measurements have been conducted over the whole field range up to 35 Tesla and angles between 0^o and 70^o. As shown in Fig. [4.13], the frequency F_1 scales well with $1/\cos\theta$ (dashed line in Fig. [4.13]) indicating that this conduction channel is two-dimensional. The F_2 oscillation, however, changes only very little with the angle θ and is therefore attributed to the bulk conduction channel.

It should be noted that there is a small shoulder in the Fourier transform spectrum near 100 Tesla visible in Figs. [4.11(d)] and [4.12]. This shoulder develops into a peak with frequency $F_3 \approx 90$ to 100 Tesla with increasing angle θ. This additional peak is attributed to another section of the bulk Fermi surface which contributes to the SdH oscillations only at higher angles θ. Since the value of F_3 is nearly independent of the angle θ, it cannot arise from surface states.

4.3.3 Berry Phase

The angle dependent transport data discussed so far lead to the conclusion that SdH oscillations from bulk and topological surface states can be measured simultaneously and resolved separately in different magnetic field ranges. The conclusion is further supported by an analysis of the Berry phase which distinguishes the nature of the charge carriers. The charge carriers of the topologically nontrivial surface states with a Dirac dispersion are expected to have a Berry phase $\beta = 1/2$, in contrast to the bulk carriers with a Berry phase of zero. β can be determined from the Landau level fan diagram [5].

It has been shown that the SdH oscillations of the conductivity $\Delta\sigma$, in contrast to oscillations of the resistivity $\Delta\rho$, provides a more accurate determination of the Berry phase [5]. To determine the nature of the charge carriers in the high-field range (with oscillation frequency F_2), we have to evaluate the SdH oscillations at sufficiently high fields, cutting off the low-field data, to eliminate any interference from the surface oscillations. It will be shown below, that the crossover from surface (F_1) to dominantly bulk (F_2) oscillations takes place at $B_c \approx 14$ Tesla. Therefore, we evaluate the bulk SdH oscillations in the field range between 15 and 35 Tesla using the the Hall conductivity $\sigma_{xy} = \rho_{xy}/(\rho_{xx}^2 + \rho_{xy}^2)$ to construct the Landau level fan diagram. The oscillating part of σ_{xy} at 5 K is plotted as function of the inverse field $1/B$ in Fig. [4.14]. The vertical dashed lines indicate the extrema above the cutoff field of 15 Tesla. It was shown that the minima and maxima of the field derivative of σ_{xy} correspond to the integer and half-integer numbers of n, respectively, whereas the extrema of σ_{xy} are shifted by $\Delta n = 1/4$ [14]. The Landau level fan diagram, shown in the inset of Fig. [4.14], includes data from both, σ_{xy} and its field derivative. The plot n vs. $1/B_n$ reveals a linear relation given by F/B_n - $\beta = n$ - 1 and the value n obtained from the extrapolation $1/B_n \rightarrow 0$ is very close to 1. Accordingly, the linear fit determines the Berry phase as $\beta = 0.03 \pm 0.08$. This value is consistent with the bulk nature of the charge carriers which give rise to the SdH oscillations in the high-field range, in agreement with the weak angle dependence (Fig. [4.13(b)]). For comparison, the Berry phase of the surface carriers is determined from the lowfield data, B $<$ 7 Tesla. In this field range, the SdH oscillations are pronounced in the second derivative of σ_{xx} with respect to the inverse field $1/B$ (see Fig. [4.15]). Here the maxima are assigned to integer values of the Landau level index n, as labeled in Fig. [4.15]. The linear extrapolation of the fan diagram (inset to Fig. [4.15]) to $1/B$ $\rightarrow 0$ reveals a value of $n_0 = 0.45$ corresponding to a Berry phase of $\beta = 0.55 \pm 0.06$. This value is in very good agreement with the earlier data for a similar crystal of $Bi_2Se_{2.1}Te_{0.9}$ [46]. The value of β close to 0.5 proves Dirac nature of the topological

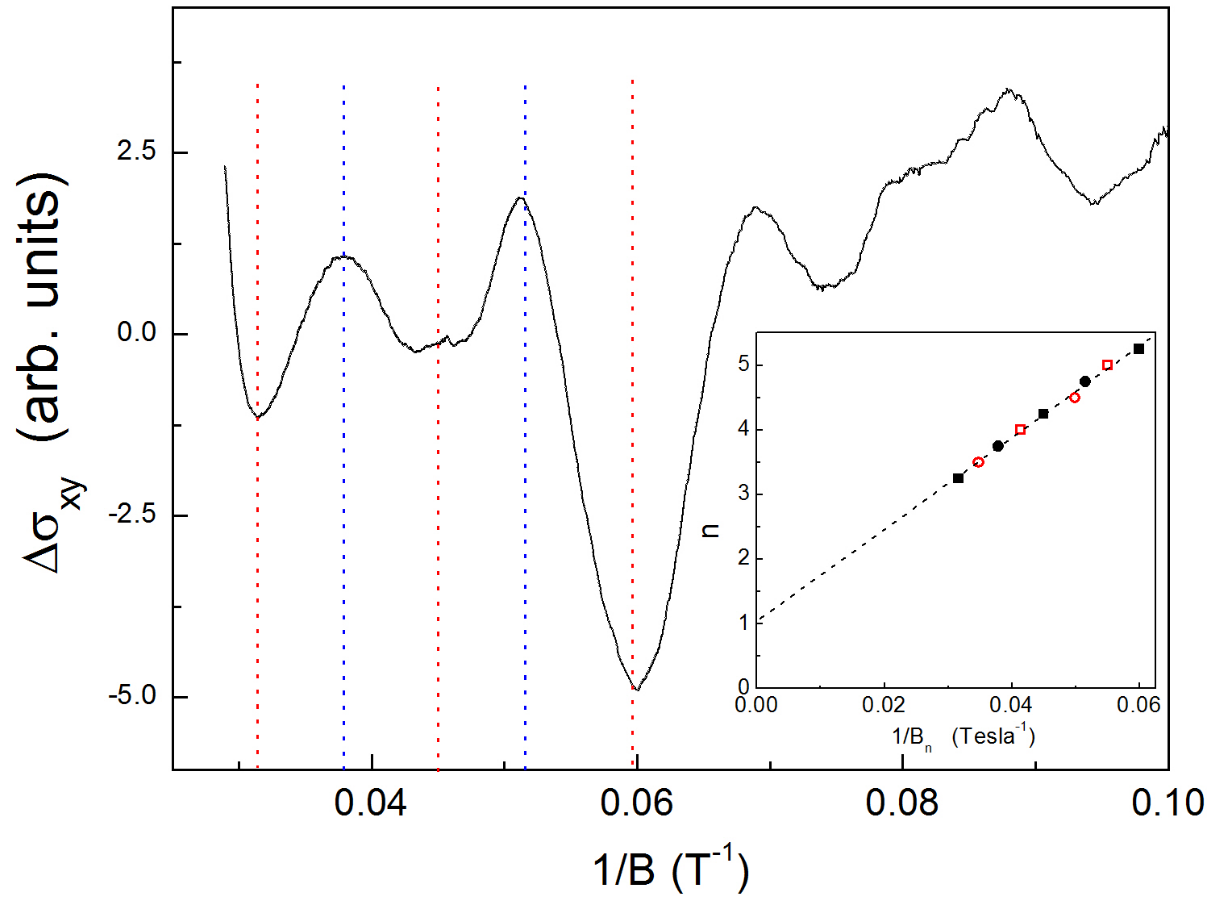

Figure 4.14: SdH oscillation of the conductivity $\Delta\sigma_{xy}$ vs. B^{-1} in the high-field range at $T = 5$ K. The positions of maxima and minima are indicated by vertical dashed lines. The inset shows the Landau level fan diagram. The linear extrapolation $1/B_n \to 0$ determines the Berry phase β. Bold (black) squares and circles are the positions of the $\Delta\sigma_{xy}$ minima and maxima, respectively. Open (red) symbols are derived from the extrema of the field derivative of $\Delta\sigma_{xy}$.

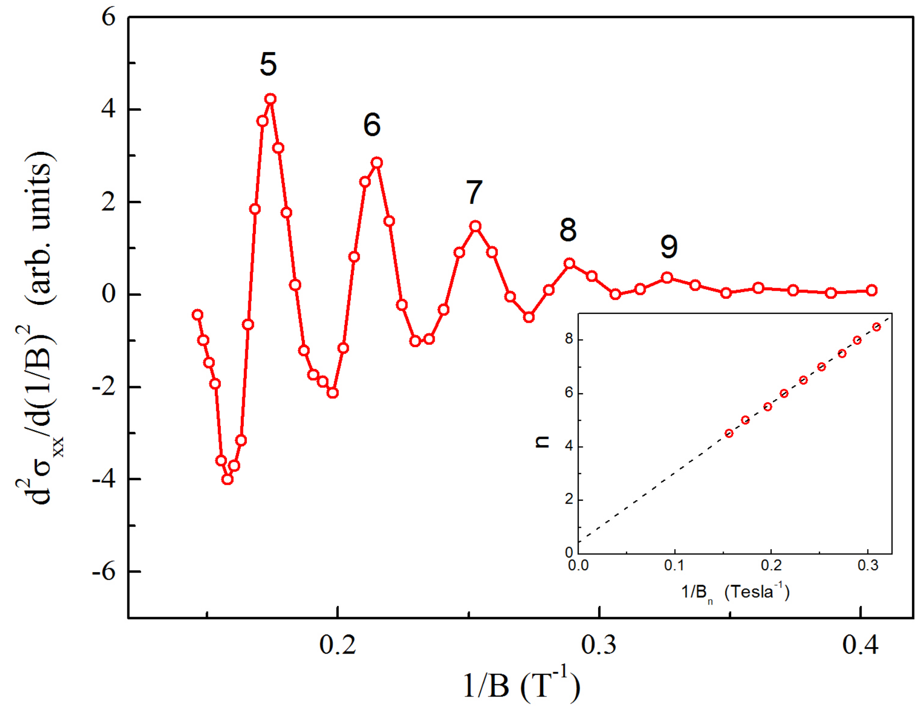

Figure 4.15: SdH oscillations of the second derivative of the conductivity $d^2\sigma_{xx}/d(1/B)^2$ vs. B^{-1} in the low-field range ($B < 7$ Tesla). The maxima correspond to integer value of n, as labeled. The inset shows the Landau level fan diagram. The linear extrapolation $1/B_n \to 0$ (dashed line) determines the Berry phase $\beta = 0.55$.

surface carriers.

4.3.4 Lifshitz-Kosevich Analysis

The separation of SdH oscillations due to the topological surface in low magnetic field from the trivial bulk states in a metallic topological insulator is interesting and it needs a careful analysis. In order to have a better understanding, the microscopic parameters defining the quantum oscillations have to be determined. This can be achieved through the Lifshitz-Kosevich (LK) analysis of the SdH oscillations of ΔR_{xx}

measured at different temperatures. According to the LK theory, the amplitude of the SdH oscillation of ΔR_{xx} is expressed as function of temperature and magnetic field: [14][5].

$$\Delta R(T,B) = \Delta R_0 e^{-\lambda_D(B)} \frac{\lambda(T/B)}{sinh[\lambda(T/B)]} \tag{4.1}$$

with

$$\lambda_D(B) = \frac{2\pi^2 k_B}{\hbar e} m_{cyc} \frac{T_D}{B} \tag{4.2}$$

$$\lambda(T/B) = \frac{2\pi^2 k_B}{\hbar e} m_{cyc} \frac{T}{B} \tag{4.3}$$

The first term in Eq. [4.1], ΔR_0, is the amplitude of the oscillation in the high-field limit $1/B \rightarrow 0$. The next term is the Dingle factor representing the exponential decrease of ΔR with decreasing field B. The last term describes the attenuation of ΔR with increasing temperature T, m_{cyc} is the cyclotron mass of the charge carriers and T_D is the Dingle temperature which is related to the inverse life time of the carriers.

There are only three fit parameters in Eqs. [4.1] to [4.3], ΔR_0, m_{cyc}, and T_D, which can be determined for a specific oscillation by analyzing the field and temperature dependencies of $\Delta R(T,B)$. Figure [4.16 (a))] shows the SdH oscillations of ΔR_{xx} in the high field range at different temperatures. The temperature dependence of ΔR is solely determined by the $\lambda/sinh\lambda$ term in Eq. [4.1]. The fitting of this expression to the data at different constant magnetic fields, e.g. at 25 Tesla as shown in Fig. [4.17], allows for the determination of the Landau level spacing $\Delta E_N(B) = \hbar eB/m_{cyc}$ and the cyclotron mass m_{cyc} from the slope of the plot ΔE vs. B in Fig. [4.17], lower

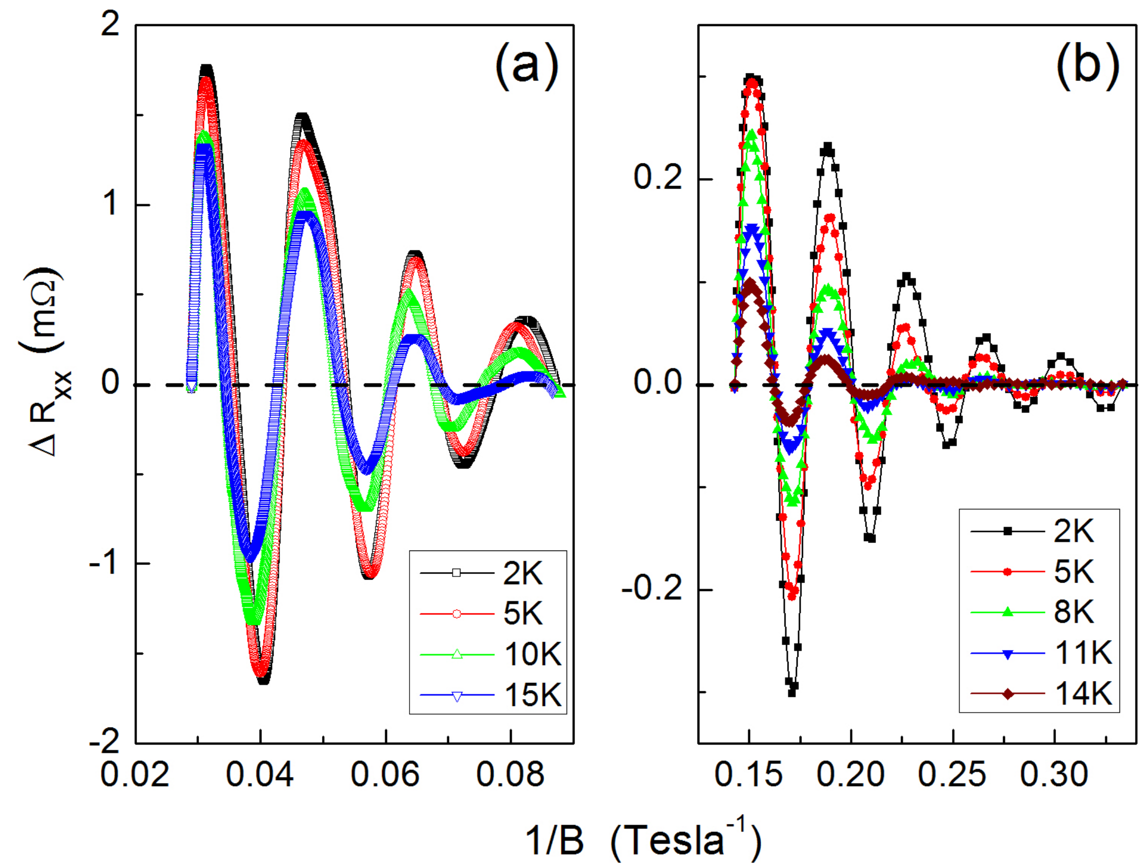

Figure 4.16: SdH oscillation of ΔR_{xx} vs. B^{-1} in the high-field range at different temperatures between 2 K and 15 K. (a) In high field range 12 T to 35 T (b) In low field range 3 T to 7 T.

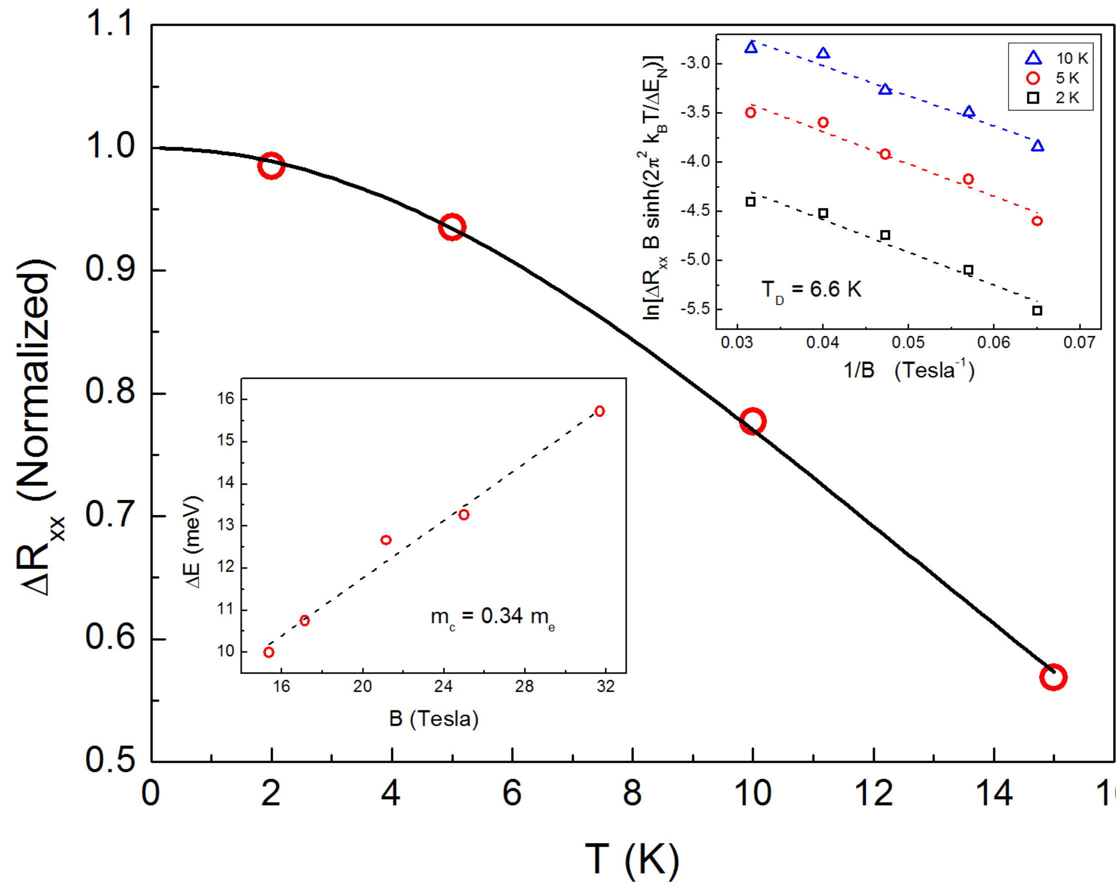

Figure 4.17: LK analysis of the high-field SdH oscillation with frequency F_2. Main panel: Temperature dependence of the amplitude ΔR_{xx} at 25 Tesla. The line is a fit to the LK formula (4.1). The lower inset shows the Landau level spacing ΔE as function of magnetic field B. The cyclotron mass $m_{cyc} = 0.34m_o$ is determined from the slope of $\Delta E(B)$. The upper inset is the semi-logarithmic Dingle plot from which the Dingle temperature $T_D = 8.5$ K is obtained.

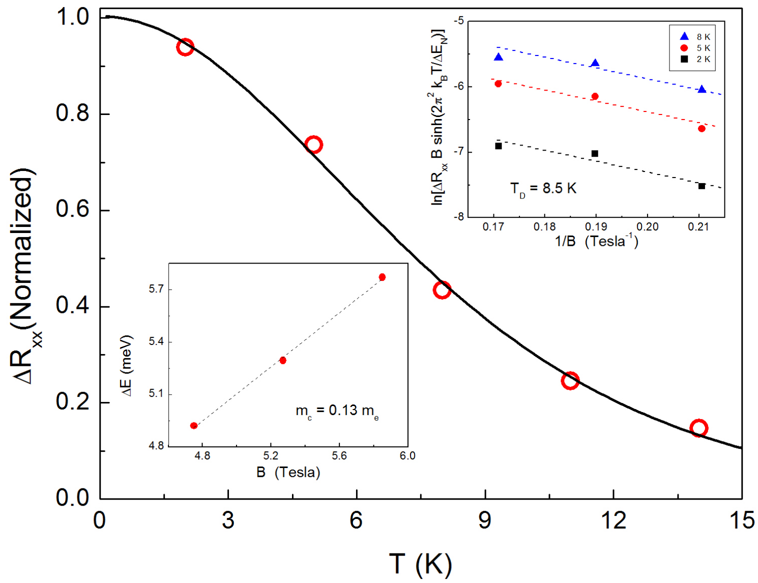

Figure 4.18: LK analysis of the low-field SdH oscillation with frequency F_1. Main panel: Temperature dependence of the amplitude ΔR_{xx} at 5.85 Tesla. The line is a fit to the LK formula (4.1). The lower inset shows the Landau level spacing, ΔE, as a function of magnetic field B. The cyclotron mass m_{cyc}= 0.13 m_o is determined from the slope of ΔE (B). The upper inset is the semi-logarithmic Dingle plot from which the Dingle temperature T_D = 6.6 K is obtained.

inset. For the high-field (bulk) oscillations we obtain $m_{cyc} = 0.34 m_o$ (m_o is the bare electron mass).

The Dingle temperature can be determined from the semi-logarithmic plot shown in the upper inset of Fig. [4.17] for three different temperatures. The dashed lines are a linear fit to the data and T_D = 6.6 K is calculated from the slopes. With the parameters m_{cyc} and T_D fixed, the oscillation amplitude can be estimated from the data of Fig. [4.16] as ΔR_0 = 5.04 mΩ. The three parameters completely define the bulk SdH oscillation amplitude as function of magnetic field and temperature, dominating the quantum oscillations above 15 Tesla. In the low-field range, the SdH oscillations are determined by the topological surface states. A similar evaluation

Table 4.1: Comparison of the relevant parameters of bulk and surface SdH oscillations of $Bi_2Se_{2.1}Te_{0.9}$

	$\Delta\ R_0$(mΩ)	m_{cyc}/m_o	T_D (K)
Bulk	5.04	0.34	6.6
Surface	2.6	0.13	8.5

within the LK theory, restricted to below 10 Tesla, reveals the set of parameters for the SdH oscillations arising from the surface conduction. For the current sample, those parameters are $\Delta R_0 = 2.6$ mΩ, $m_{cyc} = 0.13\ m_o$, and $T_D = 8.5$ K.

The parameters for bulk and surface quantum oscillations are compared and summarized in Table [4.1]. Note that the oscillation amplitude ΔR_0 of the bulk SdH oscillations is larger by a factor of 2 as compared to ΔR_0 of the surface states, explaining the domination of bulk oscillations at higher magnetic fields. However, the cyclotron mass m_{cyc} of the bulk oscillations is also significantly larger than that of the surface conduction resulting in a faster exponential decay at lower fields and higher temperatures. Although the Dingle temperature T_D is slightly lower in the bulk, the product of m_{cyc} and T_D, which determines the exponent λ_D in Eq. [4.1], is still larger and the bulk oscillations decrease more rapidly upon decreasing magnetic field. Therefore, the SdH oscillations are dominated by surface states in the low-field range. As an example, we show in Fig. [4.19] the oscillation amplitudes for both, surface (frequency F_1) and bulk (frequency F_2) transport, at 5 K calculated with the parameters from Table [4.1]. It is obvious that, with increasing magnetic field, there is a crossover from surface dominated to bulk dominated SdH oscillations. For example, at 5.85 T (data shown in Fig. [4.18]) the ratio of surface and bulk oscillation

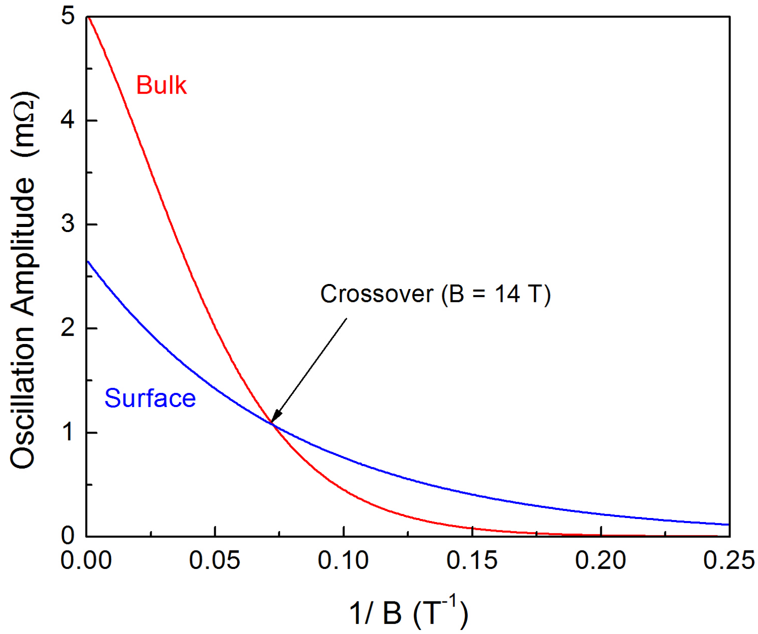

Figure 4.19: Amplitudes of bulk and surface SdH oscillations as function of inverse magnetic field at 5 K. The crossover point of 14 Tesla is indicated in the figure. The curves have been calculated from the LK theory (Eq. [4.1]) with the physical parameters listed in Table [4.1].

amplitudes is about 9, demonstrating the dominance of quantum oscillations from topological surface states at this field. At 14 T, both oscillation amplitudes are equal resulting in the strongest interference. Below and above this crossover field, surface and bulk oscillations can well be separated, as shown in the frequency analysis above.

4.3.5 Summary and Conclusions

Shubnikov-de Haas oscillations have been observed in metallic $Bi_2Se_{2.1}Te_{0.9}$ with hole type carriers in magnetic fields up to 35 T. Two characteristic oscillation frequencies, F_1 and F_2, represent oscillations from surface and bulk states, respectively. The character of the surface and bulk carriers is determined from the angle dependence of the SdH oscillations and the derived Berry phase. It is demonstrated that both oscillations can be separated whereas the topological surface states dominate in the low-field range and the bulk oscillations increase in relative weight at higher magnetic fields. The origin of this separation is found in the different cyclotron masses ($m_{cyc}^{bulk}/m_{cyc}^{surf} \approx 3$) which causes the bulk oscillations to decay (exponentially) more rapidly if the magnetic field is decreased. The crossover from bulk to surface dominated quantum oscillations upon decreasing field is found at a critical value of $B_c = 14$ Tesla. The results of this study show that SdH oscillation from topological surface states can be detected even when the Fermi energy cuts through the valence band and the bulk transport properties are metallic. The key to separate surface and bulk oscillations is the difference of the cyclotron mass m_{cyc} which has a profound effect on the oscillation amplitudes as a function of magnetic fields. According to the Lifshitz-Kosevich theory, the oscillation amplitude decreases exponentially with the inverse magnetic field and the exponent is determined by m_{cyc}. In the current example, $Bi_2Se_{2.1}Te_{0.9}$, the field ranges where bulk and surface oscillations dominate, are well separated and the analysis of the quantum oscillations can be conducted at high and low fields revealing the fundamental parameters of bulk and surface oscillations, respectively. Other topological systems with bulk metallic conduction are expected to show similar properties and may be analyzed following the procedure outlined above.

4.4 Weak Antilocalization in Bi_2Te_3

We have performed magnetotranport study to examine the weak antilocalization (WAL) effect in metallic Bi_2Te_3 single crystals. We have also calculated different physical parameters characterizing the weak antilocalization. From the angle dependence of WAL with respect to the magnetic field direction, we have shown the dominance of topological surface states in the magentoconductance of Bi_2Te_3 single crystals having low bulk carriers although the bulk states show a metallic behavior.

4.4.1 Experiment

We have selected 2 single crystals of freshly cleaved Bi_2Te_3 (HD1 and HD2) and cut them almost in a rectangular shape. Six gold contacts were sputtered on the a-b plane (hexagonal plane) as explained in method section. Platinum wires were attached for standard resistivity and Hall measurements. The magnetotransport measurements in low field up to 7 Tesla were carried out using ac-transport option of the physical property measurement system (PPMS, Quantum Design). The sample was mounted on the rotator platform and plugged into the PPMS horizontal rotator probe. Similarly, high field magnetotransport measurements have been conducted using a lock-in technique at the National High Magnetic Field Laboratory (NHMFL) in Tallahassee, FL. The sample was mounted on a rotating platform which allowed for positioning the sample at different angles with the magnetic field. The platform, mounted in a ^{3}He cryostat (Oxford), was inserted into the 50 mm bore of a resistive magnet with a maximum field of 31 Tesla. A Hall sensor was also attached on the sample platform to determine the precise angle of rotation of the sample with respect to the direction of magnetic field.

4.4.2 Resistivity and Hall Measurements

Figure [4.20] shows the temperature dependence of the longitudinal resistivity for the HD1 and HD2 samples. Both samples show a metallic behaviour below the room temperature. The resistivity of the HD1 sample is higher than the HD2 sample over the whole temperature range. The inset in Fig. [4.20] (upper left) shows the magnetic field dependence of the Hall resistance at 5 K. The positive slope of the Hall resistance for both the HD1 and HD2 samples indicate the positive (hole) type of the bulk carriers. The carrier concentration is inversely proportional to the slope of the Hall resistance. The slope of the Hall resistance for the HD1 sample is higher than that for the HD2 sample. This is consistent with the lower bulk carrier concentration of the HD1 sample $N(\mathrm{HD1}) = 6 \times 10^{17}$ cm^{-3} in compared to the HD2, $N(\mathrm{HD2}) = 3 \times 10^{18}$ cm^{-3}.

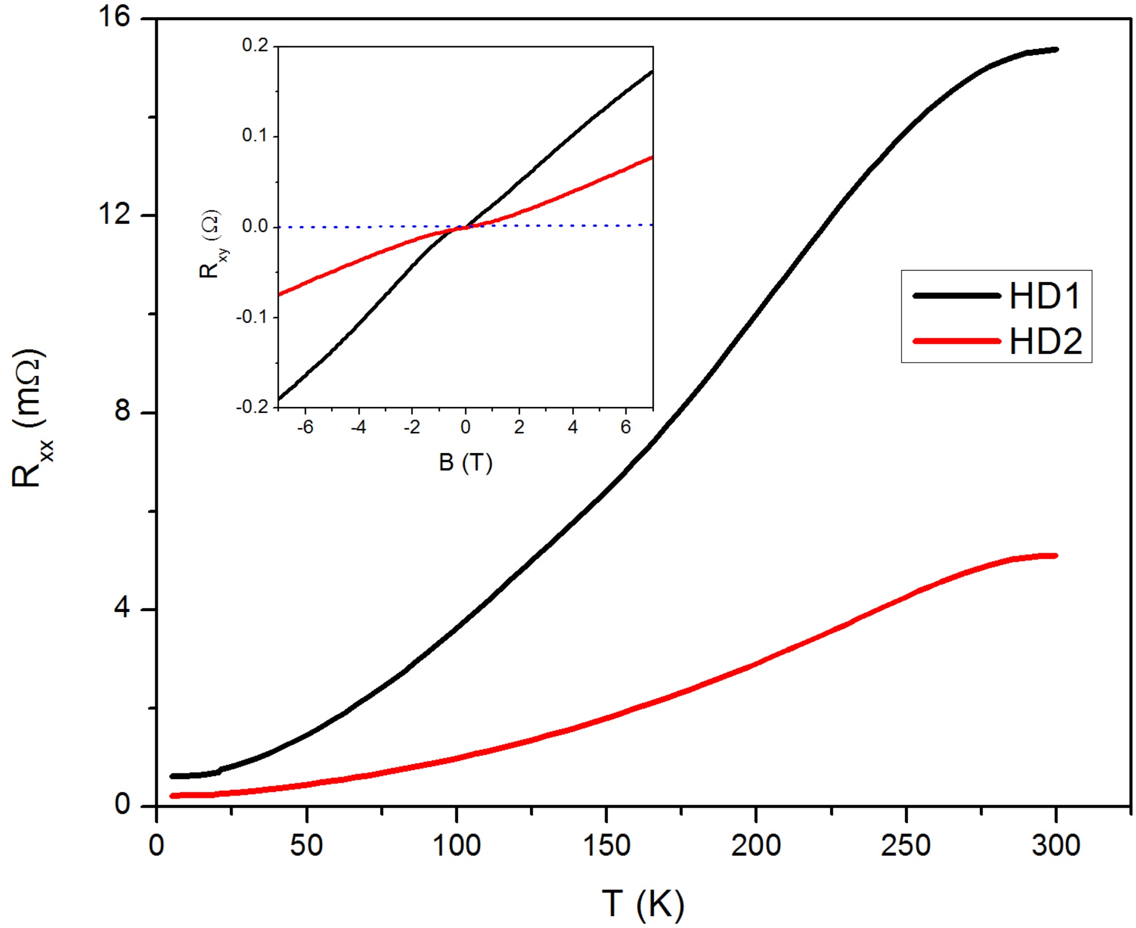

Figure 4.20: Temperature dependence of resistivity of Bi_2Te_3 samples (HD1 and HD2) single crystals. The upper left inset shows Hall data at 5 K.

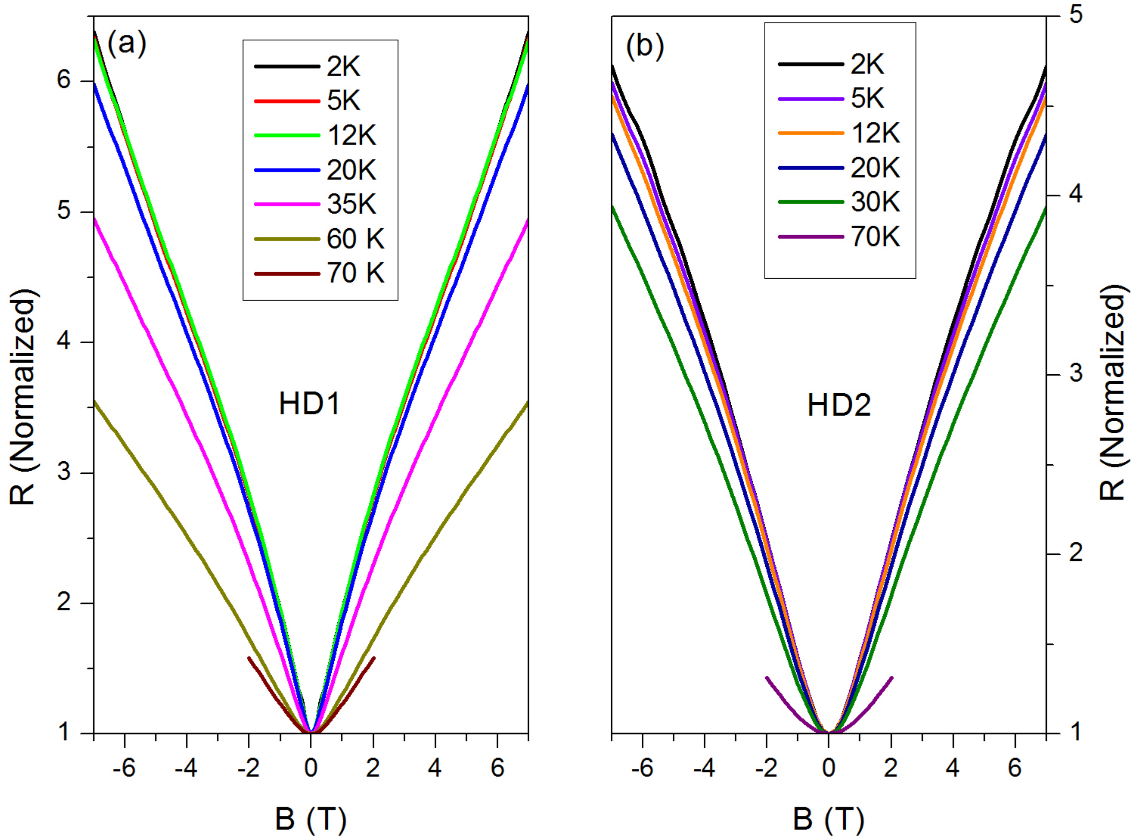

Figure 4.21: Normalized magnetoresistiance of Bi_2Te_3 HD1 and HD2 single crystals at various temperatures.

4.4.3 Magnetoconductance Measurements in Bi_2Te_3 Single Crystals

In order to understand the origin of the conductive channel in the HD1 and HD2 samples, we have performed magnetoresistance measurements with magnetic field perpendicular to the sample surface. Figure [4.21 (a)] shows the normalized magnetoresistance, i.e. R(B)/R(0), of the HD1 sample at different temperature as a function of magnetic field up to 7 T. A sharp resistance dip is clearly observed at T=2 K, indicating the presence of a WAL effect in the HD1 sample [32]. With an increase in temperature, the cusp like feature at low B is broadened and finally turns into parabolic feature (curve at 70 K in Fig. [4.21 (a)]) due to the decrease of the phase coherence length at higher temperature [49]. This observation is consistent with the previous reports in Bi-Se-Te topological insulators [50][38].
Similar magnetoresistance measurements were carried out in the HD2 sample in magnetic field up to 7 T. The temperature dependent magnetoresistance curves of the HD2 sample is shown in Fig. [4.21 (b)]. There also exists a cusp like feature in the magnetoresistance curve at low temperature, T = 2 K. This indicates the existence of a WAL in the HD2 sample as well. However, the sharpness of cusp like feature in the HD2 sample is smaller than in the HD1 sample. This gives a hint to a partial 3D contribution of the bulk spin-orbit coupling [38].

As a quantum correction to classical conductivity, a WAL can be originated either from the strong spin-orbit coupling in the bulk states or in the topological surface states. In order to clarify the origin of the WAL, we have performed the angle dependent magnetoresistance measurements at high magnetic field up to 31

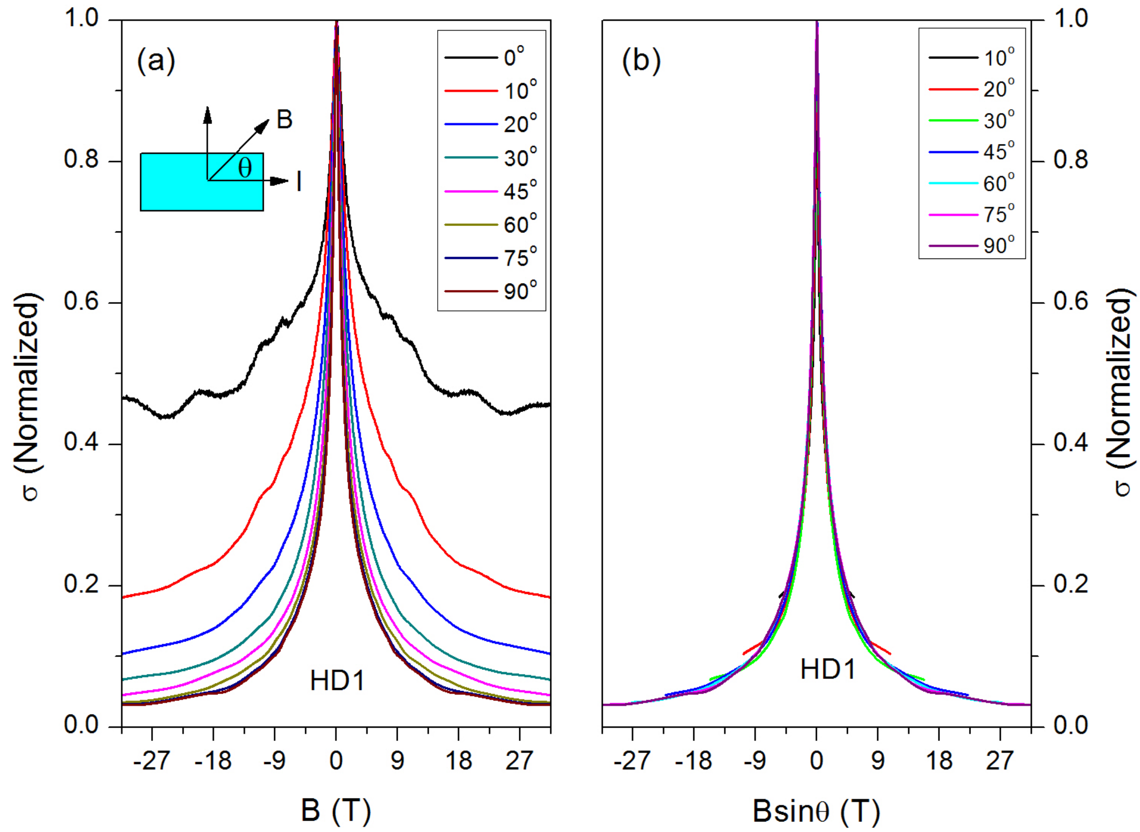

Figure 4.22: Magnetoconductance curves of the HD1 sample measured at 0.4 K. (a) The angle dependent magnetoconductance curves at different angle of rotation of sample. (b) The magnetoconductance curves plotted against the perpendicular component, $B sin\theta$ of the magnetic field.

T in national high magnetic field laboratory, Florida. Figure [4.22 (a)] shows the magnetoconductance, defined as $\sigma(B,\theta) = R(0)/R(B,\theta)$, measured along different angle of rotation θ at 0.4 K. The angle, θ is defined as the angle between the direction of magnetic field (B) and the current (I). The magnetoconductance strongly depends on the tilt angle of the applied field B. If the WAL is originated due to spin-orbit interaction in the topological surface states, the magnetoconductance should

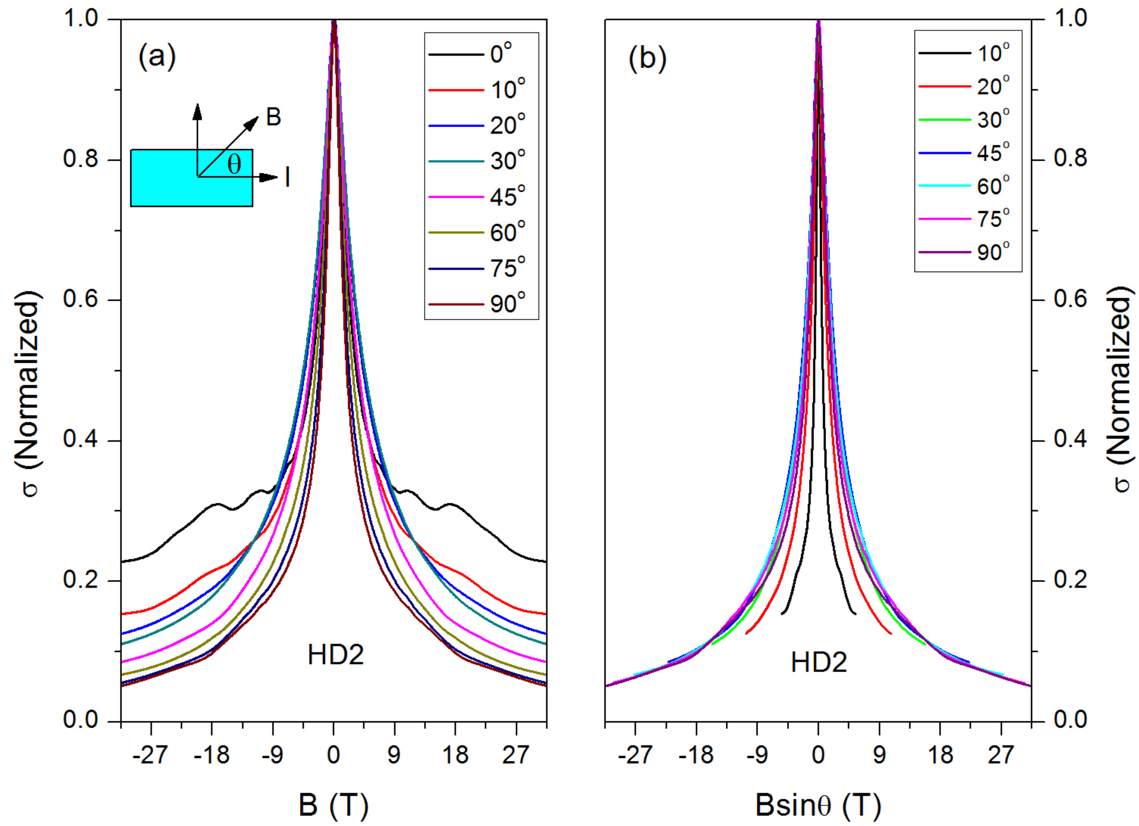

Figure 4.23: Magnetoconductance curves of the HD2 sample measured at 0.4 K. (a) The angle dependent magnetoconductance curves at different angle of rotation of sample. (b) The magnetoconductance curves plotted against the perpendicular component, $Bsin\theta$ of the magnetic field.

depend only on the normal component of magnetic field [34][51]. All the magnetoconductance curves at low magnetic field merged together when they are plotted as a function of the normal component $B\sin\theta$, as shown in Fig. [4.22 (b)]. This indicates that the observed WAL arises from 2D topological surface states in the HD1 sample.

We have also carried out the similar angle dependent magnetoconductance experiments on the HD2 sample. Figure [4.23 (a)] shows the magnetoconductance as a function of the angle θ at 0.4 K for the HD2 sample. Because of the large scale

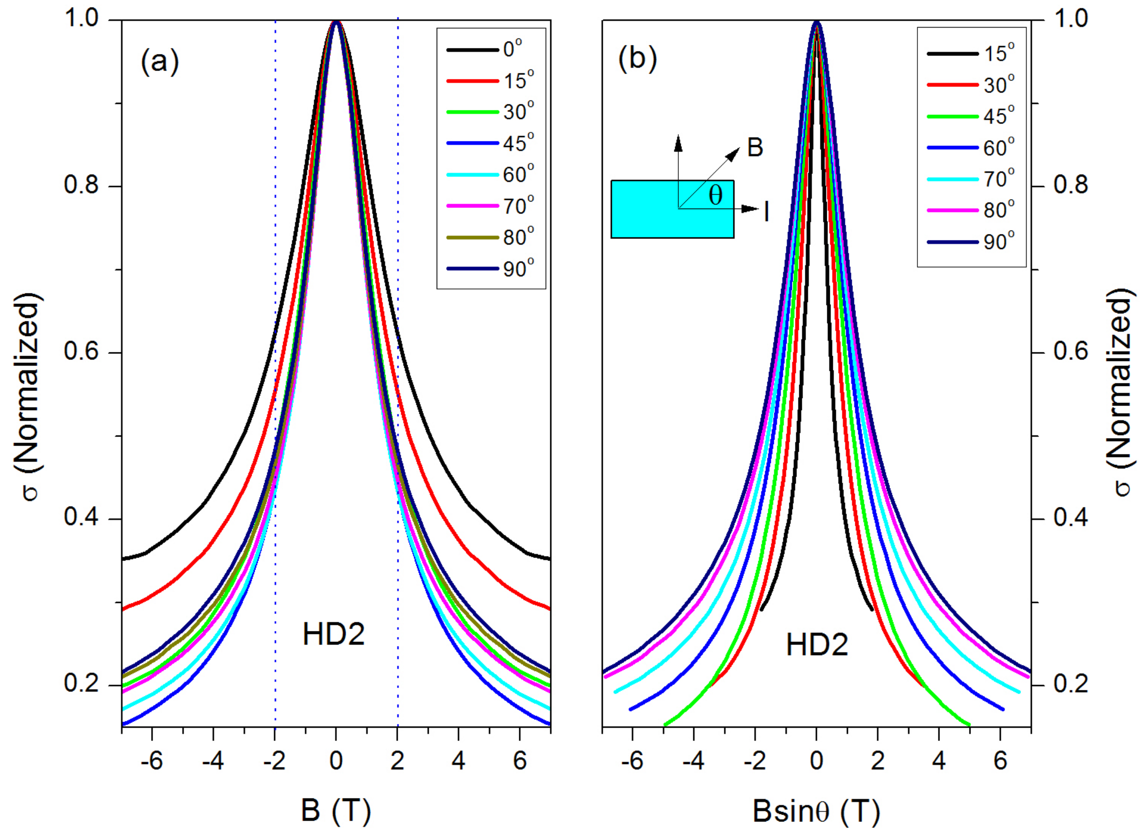

Figure 4.24: Magnetoconductance curves of the HD2 sample measured at 5 K. (a) The angle dependent magnetoconductance curves at different angle of rotation of sample. (b) The magnetoconductance curves plotted against the perpendicular component, $Bsin\theta$ of the magnetic field.

of the figure, it is hard to judge whether the magnetoconductance curves scale with B or $B\sin\theta$. In order to investigate it further, we have performed low field magnetotransport measurments in PPMS (Quantum Design). The persistent magnetic field and stable temperature control, as opposed to the sweeping magnetic field at the high magnet lab, allow us to carry out precise measurements in PPMS. Figure [4.24] shows the magnetoconductance curves of the HD2 sample in low field range (7 Tesla) at 5 K. Within 2 Tesla field range, the magnetoconductance curves weakly depend on the angle of rotation θ. This behavior is similar to the case where a WAL is caused mainly by the spin-orbit coupling in a 3D bulk channel. If the WAL is caused mainly by the spin-orbit coupling in a 3D bulk channel, the magnetoconductivity is independent of the tilt angles of the magnetic field. Except lower angles, the magnetoconductance curves scale very well with the magnetic field B as shown in Fig. [4.24(a)], suggesting the bulk states origin. The bulk origin of the WAL in the HD2 sample is further verified from the spreading of the magnetoconductance curves plotted as a function of the normal components $Bsin\theta$, as shown in Fig. [4.23 (b)].

The results discussed above show that although the WAL effects are observed both in the HD1 and HD2 samples, they have originated from different electronic states. The dominance of topological surface states in the magnetoconductance in the HD1 sample as compared to the HD2 sample is interesting and need more careful analysis. Both the HD1 and HD2 samples show a metallic behavior and have p-type bulk charge carriers. The only difference is that the HD1 sample has lower carrier concentration than the HD2 sample. This gives a hint that the carrier density might be playing a role for the dominance of surface states in WAL effect of the HD1 sample. In order to understand this further, we have chosen another n-type single crystal, HD3, having lower bulk charge carriers. The n-type nature of the bulk carriers in the HD3 sample also allows us to investigate whether the nature of the charge carriers (p or n-types) plays a role in the observation of the WAL due to topological surface states or not.

The temperature dependence of the resistivity of the HD3 sample is shown

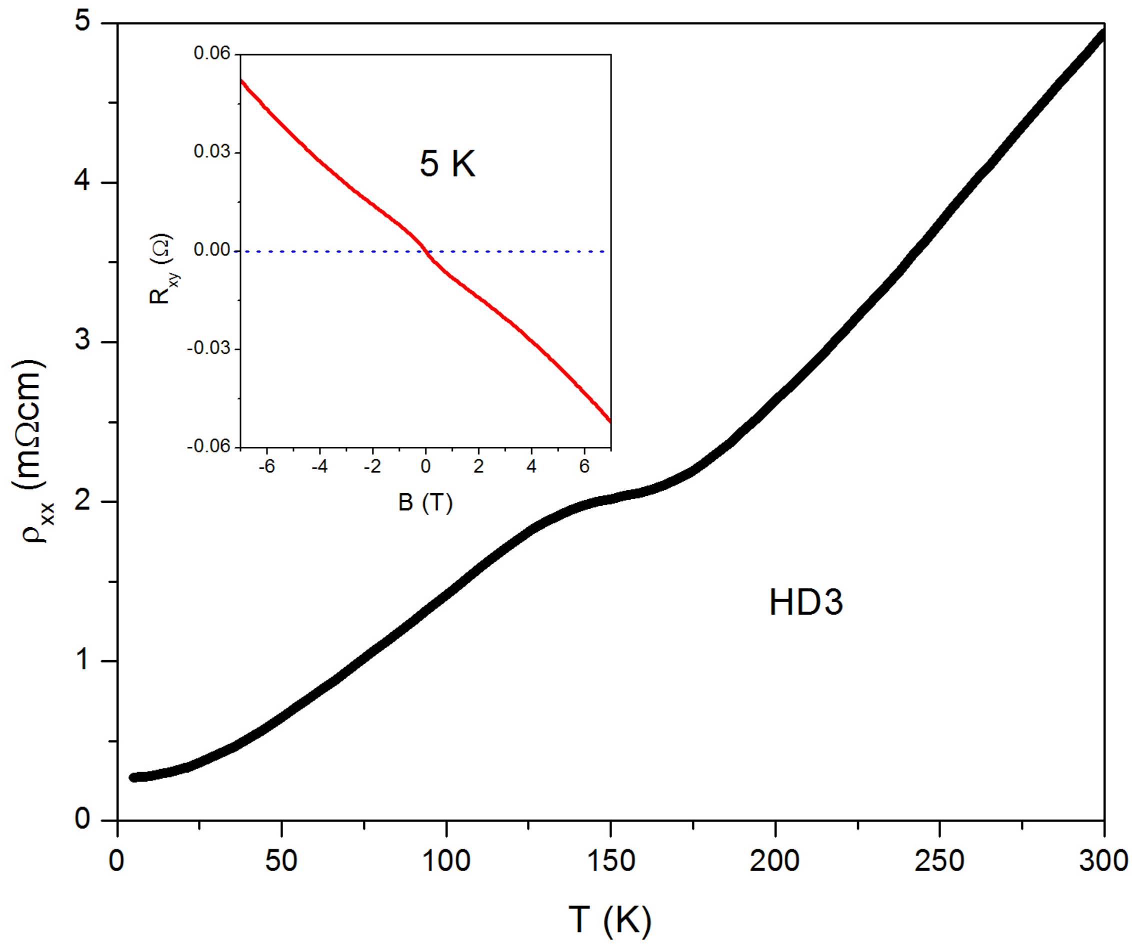

Figure 4.25: Temperature dependence of resistivity of Bi_2Te_3 HD3 single crystal. The upper left inset shows Hall data at 5 K.

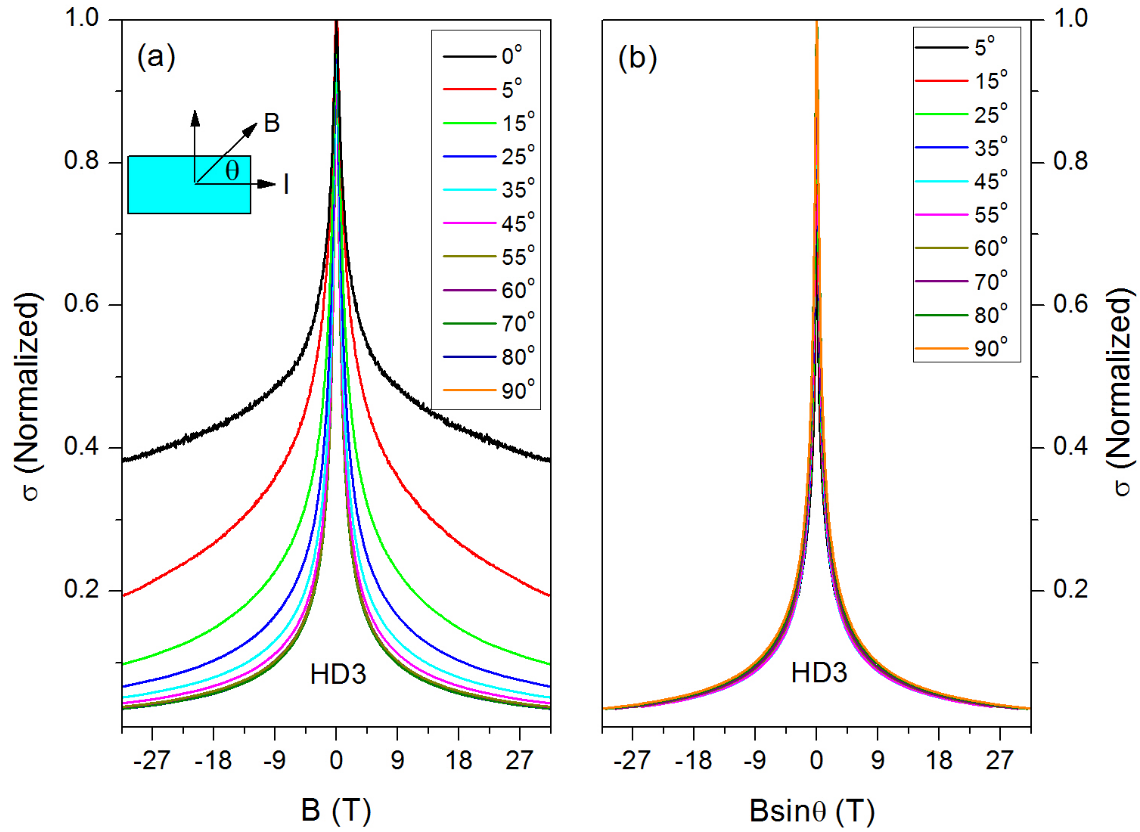

Figure 4.26: Magnetoconductance curves of the HD3 sample measured at 5 K. (a) The angle dependence magnetoconductance curves at different angle of rotation of sample. (b) The magnetoconductance curves plotted against the perpendicular component, $Bsin\theta$ of the magnetic field.

in Fig. [4.25]. The resistivity shows the metallic behavior below room temperature. Around 150 K, there is a slight upturn of the resistivity, however, the resistance decreases further lowering the temperature. The negative slope of the Hall resistance reveals that the charge carriers are negative (electron), as shown in the inset of Fig. [4.25]. The bulk carrier density at 5 K is estimated to be $N = 1{\times}10^{18}\ cm^{-3}$ from the Hall measurement. Figure [4.26 (a)] shows the magnetoconductance of the HD3 sample along different angle of rotation at 0.4 K. The magnetoconductance decreases with an increase in magnetic field. A cusp like feature at low magnetic field shows the existence of the WAL effect also in the HD3 sample. The WAL curve depends on the tilt angle of rotation θ, showing the possible dominace of surface states conduction channels as in the HD1 sample. The scaling of all WAL curves, as shown in Fig. [4.26 (b)] with the normal component, $Bsin\theta$ shows that the WAL in the HD3 sample is originated from topological surface states.

4.4.4 Hikami-Larkin-Nagaoka Model

To gain a deeper understanding of the WAL phenomena in the HD1, HD2 and HD3 samples, a more quantitative analysis is necessary. The quantum correction of magnetoconductivity in the 2D system can be described using Hikami-Larkin-Nagaoka (HLN) formula [37]. Under the assumption that the inelastic scattering time is much longer than both the elastic and spin-orbit scattering times,

$$\sigma = -A\left[\Psi\left(\frac{1}{2}+\frac{\hbar}{4el_\phi^2 B}\right) - ln\left(\frac{\hbar}{4el_\phi^2}\right)\right] \tag{4.4}$$

where Ψ is the digamma function, l_ϕ is the phase coherence length, and the parameter $A = \alpha\frac{e^2}{2\pi^2\hbar}$, for which α=1/2 per conduction channel. Using Eq. [4.4] to the experimental data, the fitting parameters l_ϕ and A can be obtained.

Figure [4.27] shows the HLN fitting of the magnetoconductivity data of the HD1 sample at 2 K in low field range 1 T. It is clear that the data can be fitted well using the 2D HLN model. Similarly, HLN fittings were also carried out in the HD2 and HD3 samples and calculated the parameters A and l_ϕ. The fitting parameter l_ϕ(T) represents the coherence length, i.e the distance traveled by an electron before its

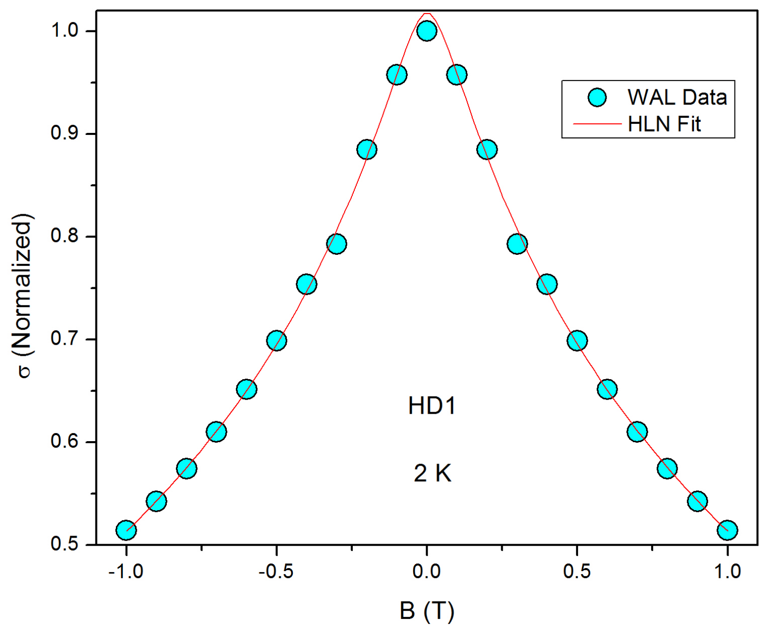

Figure 4.27: Magnetoconductance WAL curve of the HD1 sample (skyblue dot) and HLN fit (solid red).

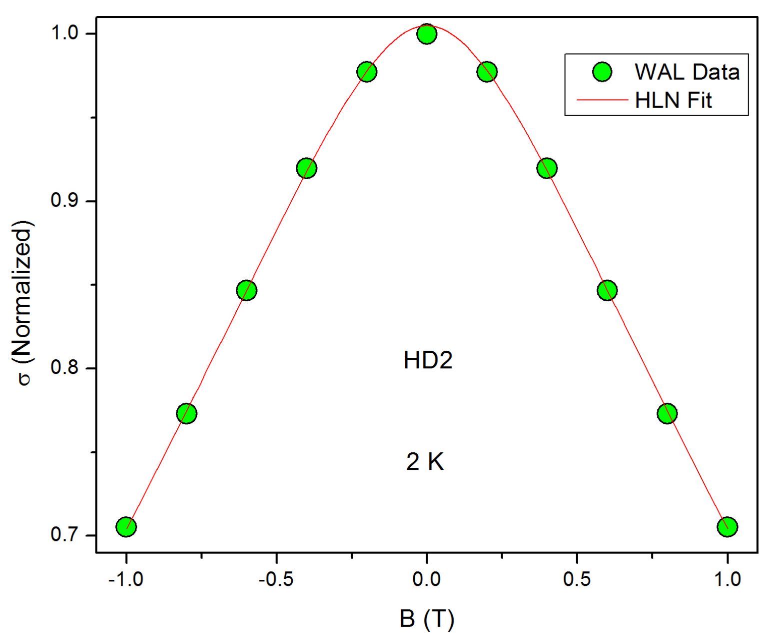

Figure 4.28: Magnetoconductance WAL curve of the HD2 sample (green dot) and HLN fit (solid red).

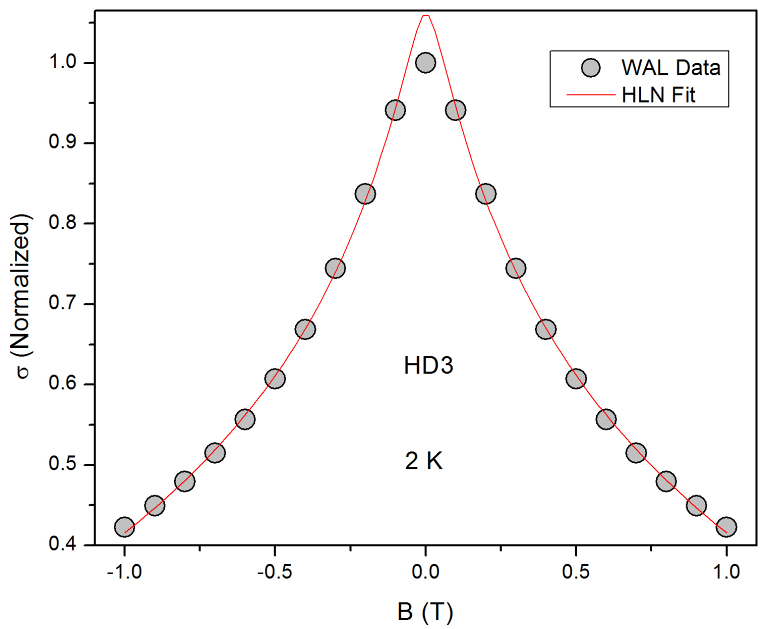

Figure 4.29: Magnetoconductance WAL curve of the HD3 sample (gray dot) and HLN fit (solid red).

phase is changed. The parameter $A = \alpha \frac{e^2}{2\pi^2\hbar}$, determines the number of conduction channels present in a sample [49]. The temperature dependence of the coherence length l_ϕ for the HD1, HD2 and HD3 samples are shown in Fig. [4.30 (a)]. According to WAL of TIs , both the electron-electron (e-e) scattering and electron-phonon (e-ph) scattering are supposed to emerge in the 3D TIs [52][49]. Therefore, the l_ϕ as a function of temperature may be expressed as:

$$\frac{1}{l_\phi^2(T)} = \frac{1}{l_\phi^2(0)} + A_{ee}T^{p_1} + A_{ep}T^{p_2}. \tag{4.5}$$

where, $l_\phi(0)$ represents the zero-temperature coherence length, $A_{ee}T^{p_1}$ and $A_{ep}T^{p_2}$ represent the contribution from the e-e and e-ph interaction, respectively. The coherence length l_ϕ (T) can be well described by Eq. [4.5] with $p_1 = 1$ and $p_2 = 2$ with l_ϕ = 59 nm, 26 nm, and 78 nm for the HD1, HD2, and HD3 samples, respectively,

Table 4.2: Comparison of the fitting parameters to Eq. [4.5] of HD1, HD2 and HD3 samples at 2 K

	l_ϕ (0) (nm)	A_{ee} (nm^{-2})	A_{ep}(nm^{-2})
HD1	59	-5.13 $\times10^{-6}$	3.25 $\times10^{-7}$
HD2	26	-6.17 $\times10^{-6}$	8.83 $\times10^{-7}$
HD3	78	3.75 $\times10^{-6}$	3.88 $\times10^{-7}$

as shown in Fig. [4.30]. The larger values of $l_\phi(0)$ for the HD1 and HD3 samples provide a further evidence of the dominance of topological surface states in their magnetoconductivities. However, the lower value of $l_\phi(0)$ in the HD2 sample tells that there is a significant bulk states contribution. Figure [4.30 (b)] shows the parameter A as a function of temperature. Almost constant values of A over a temperature range shows the existence of a constant number of conduction channels in the crystals [49]. Theoretical value of A is of the order of 10^{-6} in case of 2D systems showing WAL effect. However, A values obtained for all of our samples are less than 1, i.e., nearly 10^6 larger than the theoretical value. This difference is mainly caused by the significant contribution from the bulk conduction channels, as seen in other topological systems [53][49]. At a given temperature, the A values are almost equal for the HD1 and HD3 samples, but almost half as the A value of the HD2 sample. This tells that there exists a small number of conduction channels in the HD1 and HD3 samples as compared to the HD2 sample. The lower number of conduction channels further supports the dominance of the 2D conduction channels in the HD1 and HD3 samples.

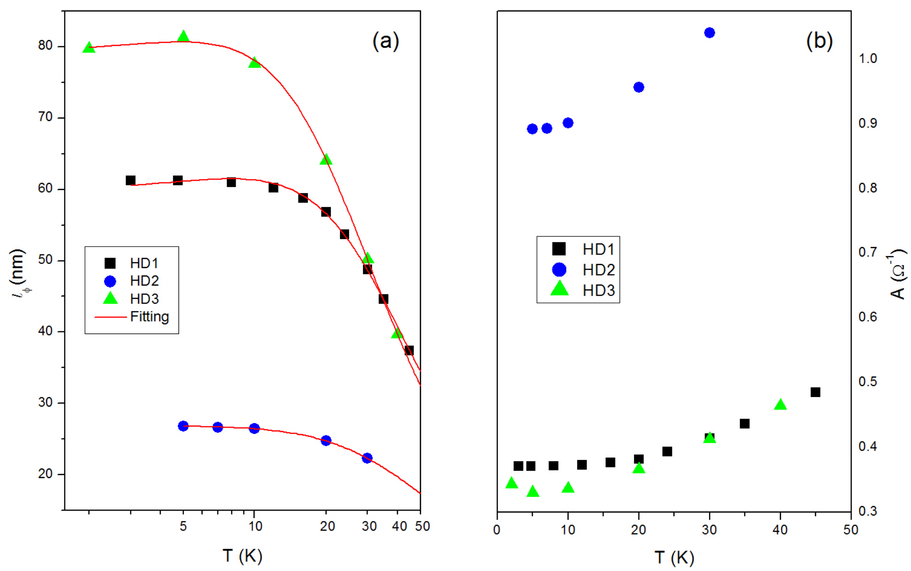

Figure 4.30: (a) Comparison of the temperature dependence of phase coherence lengths l_ϕ deduced from the WAL fit under a field limit of 1 T (solid circle). The red line shows the fit according to Eq. [4.5] with p_1=1 and p_2=2. (b) Temperature dependence of the parameter A in Eq. [4.4].

4.4.5 Summary and Conclusions

We have observed the weak antilocalization effect in the magnetoconductance measurements of Bi_2Te_3 single crystals in magnetic fields up to 31 T. The HD1 (p-type) and HD3 (n-type) samples have relatively smaller bulk carrier densities than the HD2 (p-type) sample. The angle dependence of the WAL with respect to the magnetic field direction showed the dominance of topological surface states in the samples having lower carrier concentrations, the HD1 and HD3 samples. The existence of surface states in both HD1 (p-type) and HD3 (n-type) samples shows the WAL due to topological surface states depends only the number of the bulk carriers, not on the nature of the charge carrries. The HLN formula is used to calculate different physical quantities that characterize the observed WAL effect. The temperature dependence of the coherence length of the HD1, HD2 and HD3 samples can be well described with the electron-electron and electron-phonon scattering model. For the HD1 and HD3 samples, the coherence length l_ϕ values are relatively larger and have smaller number of conduction channels as compared to the HD2 sample. The larger coherence length and smaller number of conduction channels further support the existence of topological surface states in the magnetoconductivity of the HD1 and HD3 samples.

4.5 Sb_2Te_2Se Topological Insulator

After the discovery of topological surface states in the bismuth based binary compounds like Bi_2Se_3, Bi_2Te_3, Sb_2Se_3, etc. [54][55], people have extended their research to the tetradymite-like compounds such as Bi_2Se_2Te, Bi_2Te_2Se, Bi_2Se_3Te etc [56][57]. Recently, first principles calculations have been carried out on Sb_2Te_2Se and has been reported the existence of a Dirac cone [56]. ARPES measurements have confirmed the existence of a single Dirac cone in this compound [58]. The magnetotransport measurements carried out by Wang *et al* [59] reported only the existence of a quasi-two dimensional Fermi surface based on the angle dependence of the frequency. However, the angle dependence of the quantum oscillations and the Berry phase determine whether the quantum oscillations originate from surface or bulk states. Here, we have shown the existence of topological surface states from both the angle dependence of the quantum oscillations and the Berry phase calculations.

4.5.1 Experiment

We have selected a freshly cleaved single crystal of Sb_2Te_2Se and cut into a rectangular shape. Six gold contacts were sputtered as explained in the method section for a standard longitudinal and Hall resistance measurements. Six platinum wires were used to make electrical contact for the measurements. The sample was mounted in the rotating platform of the standard probe designed in the National High Magnetic Field Laboratory, Tallahassee, FL.

4.5.2 Resistivity, Hall, and Seebeck Coefficient Measurements

Figure [4.31] shows the temperature-dependence of the resistivity for a Sb_2Te_2Se single crystal. The sample exhibits the metallic behavior below room temperature. A Hall measurement was carried out to determine the nature of the bulk charge carriers and its concentration. From the positive slope of the Hall resistance (shown in the upper left inset to Fig. [4.31]), the bulk carriers are p - type and its concentration was estimated to be $3\times10^{18}\text{cm}^{-3}$ at 5 K. The lower right inset of Fig. [4.31] shows the Seebeck coefficient as a function of temperature. The Seebeck coefficient is positive above $\approx$ 150 K. But it decreases with decreasing temperature and becomes negative below 100 K. With the further decrease of temperature, the Seebeck coefficient becomes less negative and then positive below 10 K. The sign change of the Seebeck coefficient with lowering the temperature hints that many factors contribute to Seebeck coefficient of Sb_2Te_2Se sample. The positive Seebeck coefficient at 5 K is consistent with the hole nature of the bulk carriers from the Hall measurement.

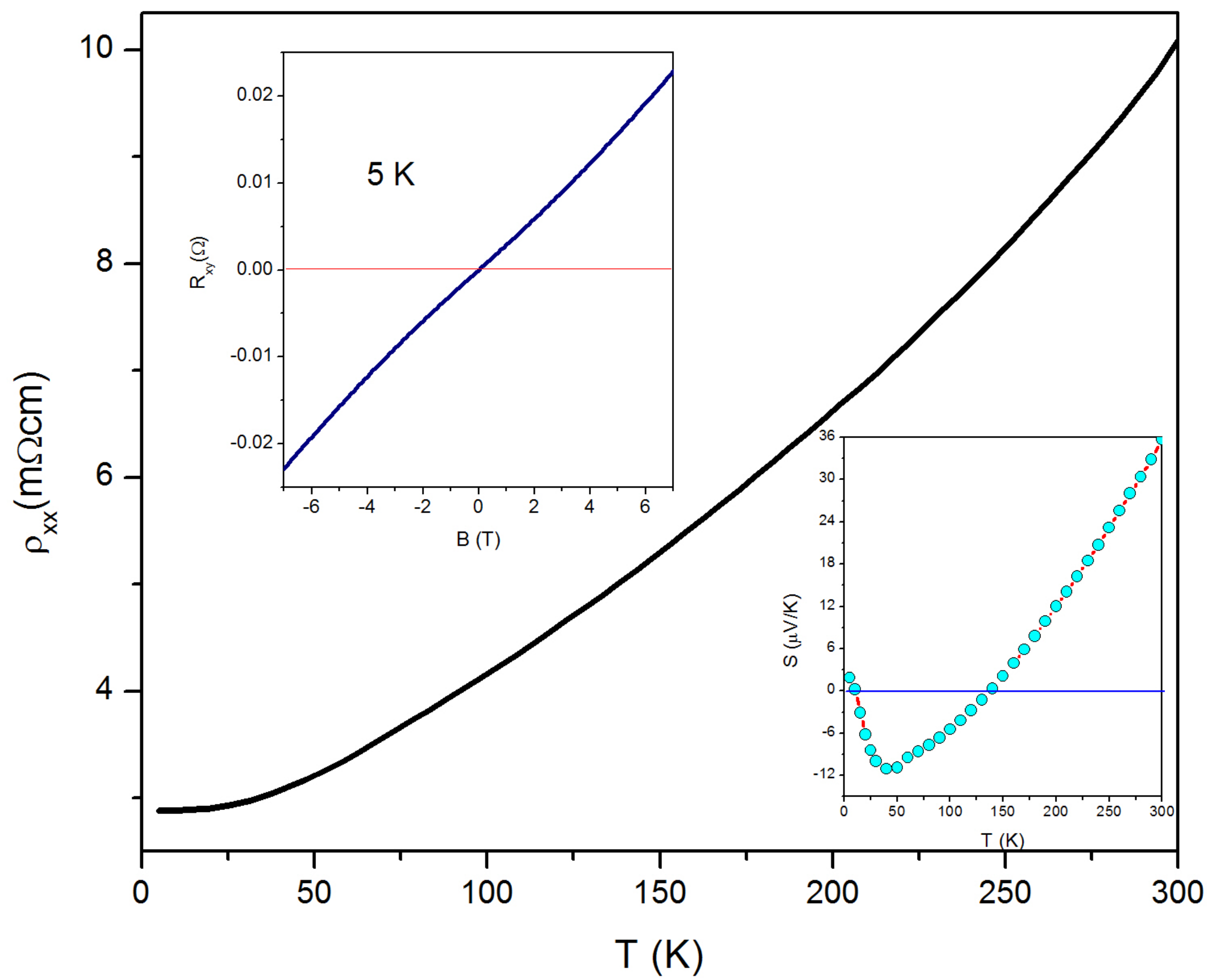

Figure 4.31: Temperature-dependence of resistivity of the Sb_2Te_2Se single crystal. The upper left inset shows Hall data at 5 K. The lower right inset displays the temperature-dependence of the thermoelectric power.

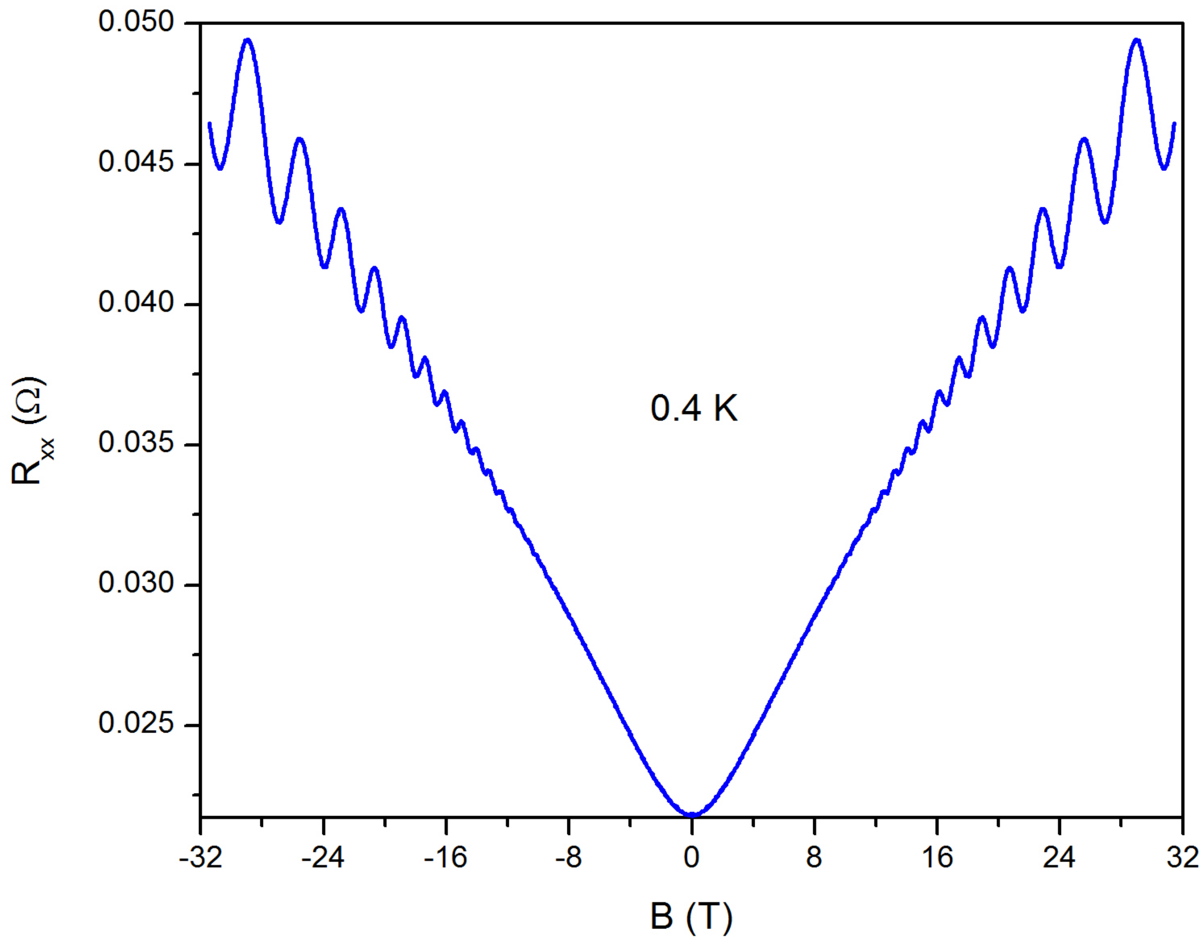

Figure 4.32: The magnetoresistance the Sb_2Te_2Se single crystal plotted as a function of B at 0.4 K.

4.5.3 Shubnikov de Haas Oscillations

Figure [4.32] shows the magnetoresistance of the Sb_2Te_2Se at 0.4 K. The longitudinal magnetoresistance (R_{xx}) is asymmetric in the positive and negative magnetic field direction. This is due to the contribution of the transverse magnetoresistance caused by the imperfect alignment of the Hall geometry. However, the antisymmetric part of R_{xx} can be removed by taking the average of R_{xx} in the positive and negative fields, i.e., $[R_{xx}(B)+R_{xx}(\text{-}B)]/2$. The magnetic field was applied perpendicular to the a-b plane of the single crystal. Due to the quantization of the electron density of states into the Landau levels in a strong magnetic field, the magnetoresistance shows SdH oscillations. The magnetoresistance of the Sb_2Te_2Se shows oscillations in the field above 15 T as shown in Fig. [4.32]. The oscillations are clear and have a single frequency. Figure [4.33] shows the quantum oscillations obtained after substracting a smooth polynomial background at different temperatures. The amplitude of quantum oscillation decrease with an increase in temperature. The oscillations are periodic in $1/B$ and have a single frequency $F = 215$ Tesla in the frequency spectrum as shown in Fig. [4.34]. The amplitude of frequencies also decreases with an increase in temperature; however, the value of frequency does not change.

4.5.4 Angle Dependent Magnetoresistance Measurements

In order to investigate the origin of quantum oscillations observed here, we have performed magnetoresistance measurements along different tilt angle of the sample w.r.t. the applied magnetic field. The sample platform in magnetic field was rotated by a stepper motor attached on the top of the probe as explained in the methods section. Figure [4.35] shows the angle-dependence of SdH oscillations at different angle (θ) of rotation with respect to the direction of the applied magnetic field B. The maxima and minima positions change systematically with the tilt angle θ. However, the maxima and minima positions align when the oscillations are plotted as a function of the normal component $Bcos\theta$ as shown in Fig. [4.36]. This implies that SdH oscillations seen here depend on the normal component of the magnetic

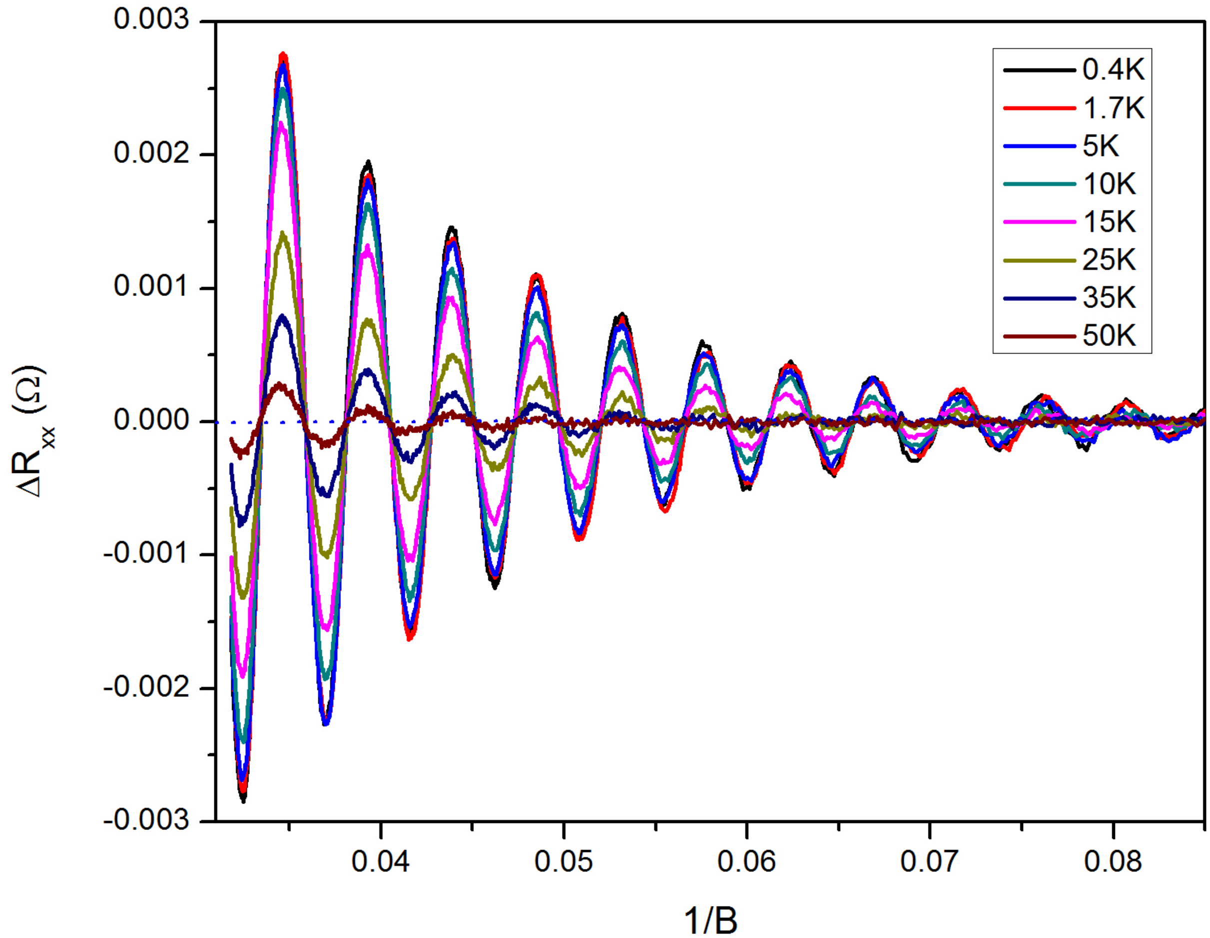

Figure 4.33: The quantum oscillations of the Sb_2Te_2Se single crystal obtained after substracting a smooth polynomial background.

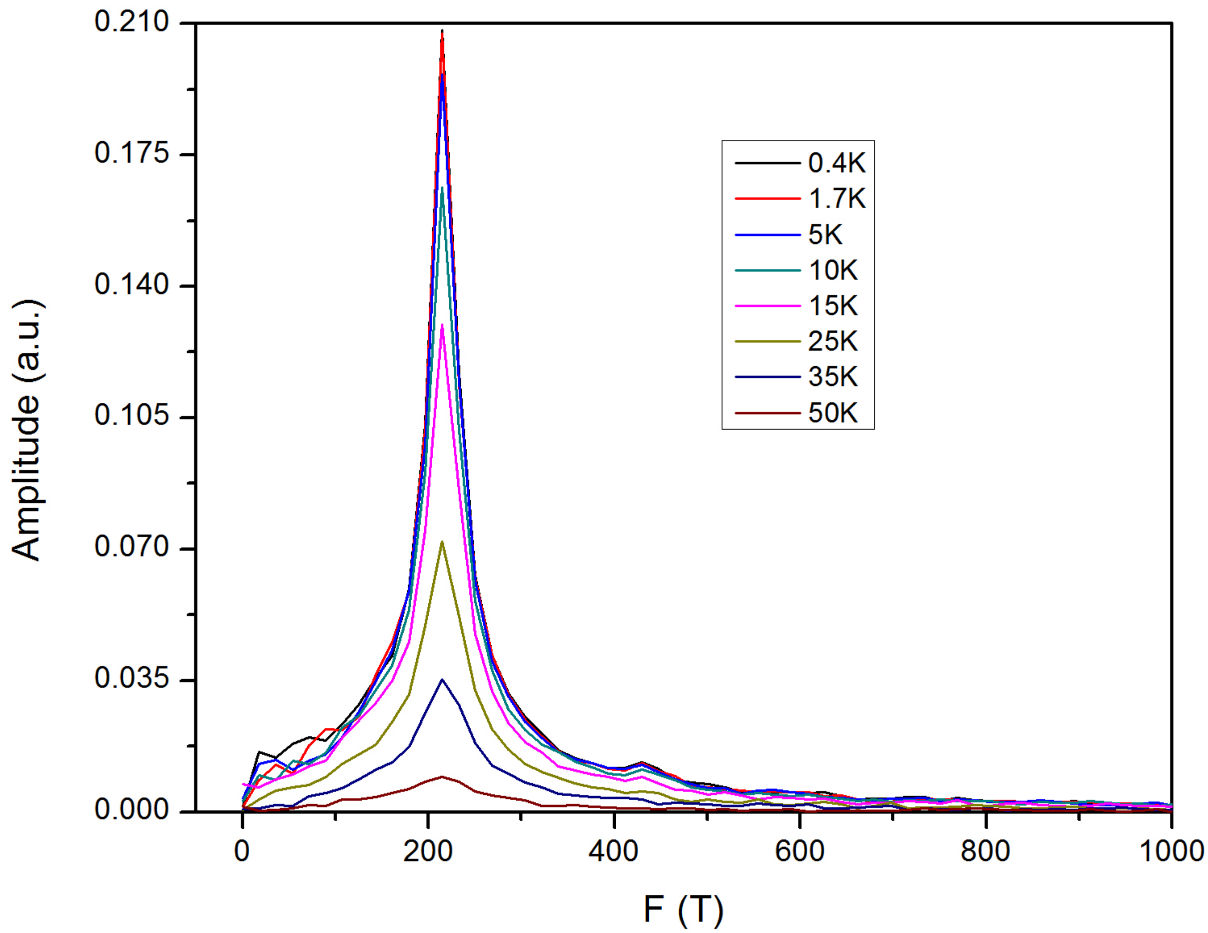

Figure 4.34: The frequency spectrum of the Sb_2Te_2Se single crystal obtained by taking the fast Fourier transform of Fig. [4.33].

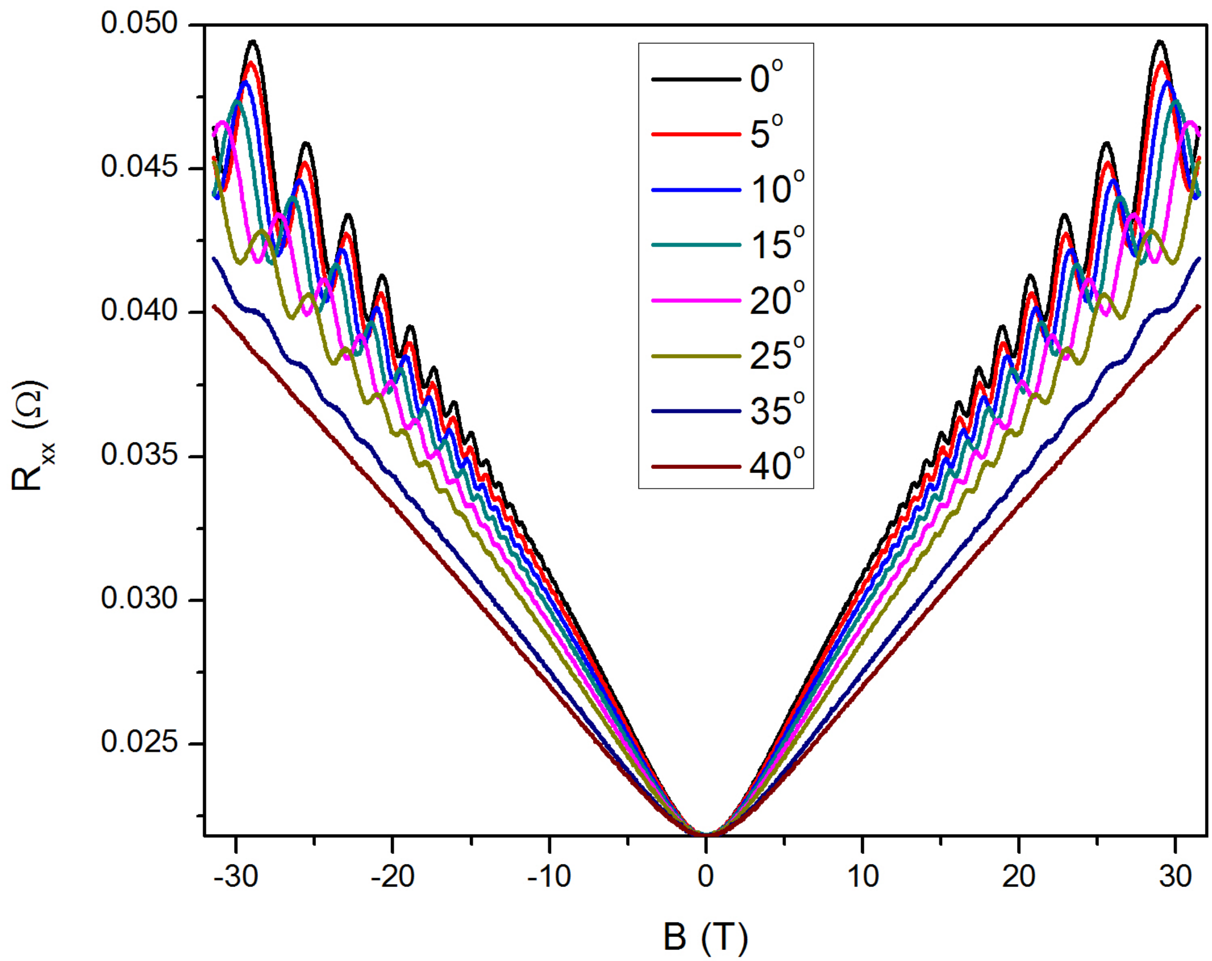

Figure 4.35: The angle-dependence of Shubnikov de Haas oscillations of the Sb_2Te_2Se single crystal plotted as a function of B.

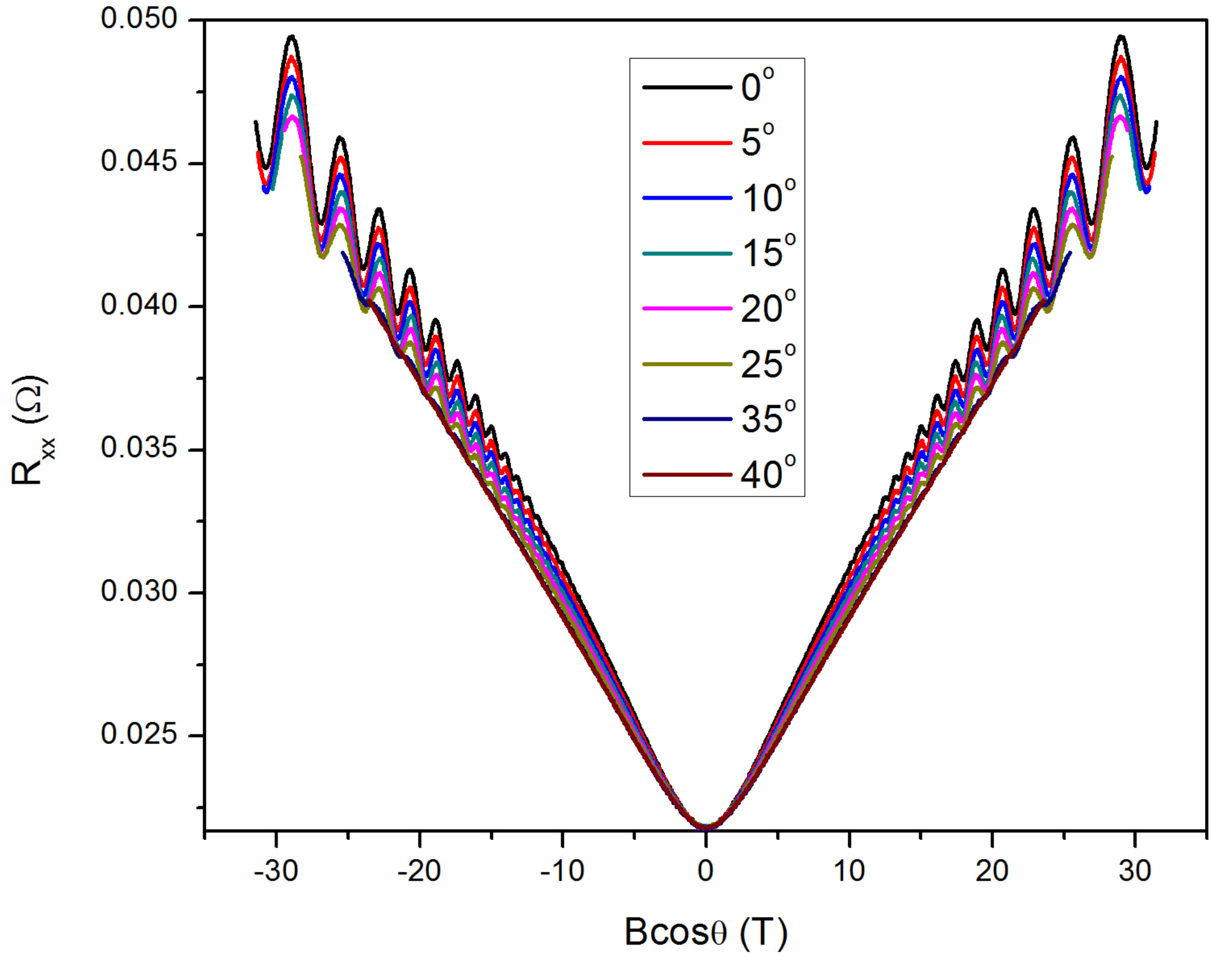

Figure 4.36: The angle-dependence of Shubnikov de Haas oscillations of the Sb_2Te_2Se single crystal plotted as a function of the normal component $Bcos\theta$.

field. This is consistent with the surface states nature of the charge carriers [5]. The SdH oscillations can not be resolved above 40^o angle of rotation of the sample. This further supports the origin of the SdH oscillation is from the topological surface states [14] [5].

4.5.5 Berry Phase

The origin of SdH oscillations can be determined by calculation of the Berry phase (β). The Berry phase takes a value of $\beta = 0.5$ for surface state electrons (Dirac electrons) and $\beta = 0$ for normal electrons. We have calculated the conductivity of the Sb_2Te_2Se using the formula,

$$\sigma_{xx} = \rho_{xx}/(\rho_{xx}^2 + \rho_{xy}^2).$$

where ρ_{xx} and ρ_{xy} are the longitudinal and the Hall resistivities respectively. Figure [4.37] shows the magnetoconductivity plotted as a function of $1/B$ at 0.4 K. The quantum oscillation is clear and has a single-frequency. The existence of a well-defined single-frequency allows us to calculate the Berry phase precisely. Let $1/B_{max}$ and $1/B_{min}$ represent the position of maxima and minima of the quantum oscillation, respectively. The positions of minima and maxima are assigned an integer and a half integer values respectively to construct the LL fan diagram [5], shown in Fig. [4.38]. In the limit of $1/B \to 0$, the LL fan diagram allows to calculate the Berry phase. The linear extrapolation $1/B \to 0$ in the Landau level fan diagram gives $\beta = 0.43 \pm 0.02$. This value of β is very close to the theoretical value of 0.5 for the Dirac particle (surface state electron). This further proves that the quatum oscillations are coming

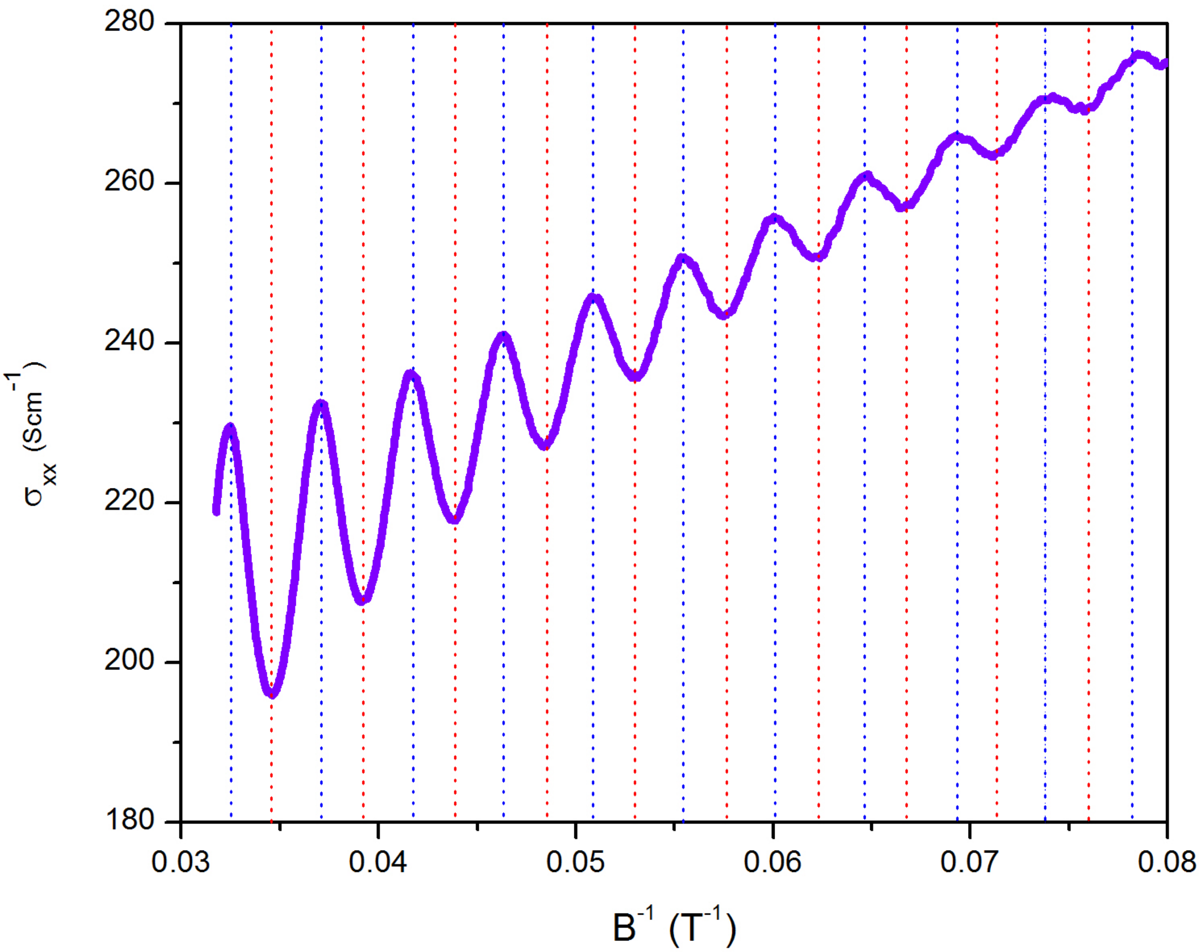

Figure 4.37: The magnetoconductivity of the Sb_2Te_2Se single crystal plotted as a function of the inverse of the magnetic field B^{-1}.

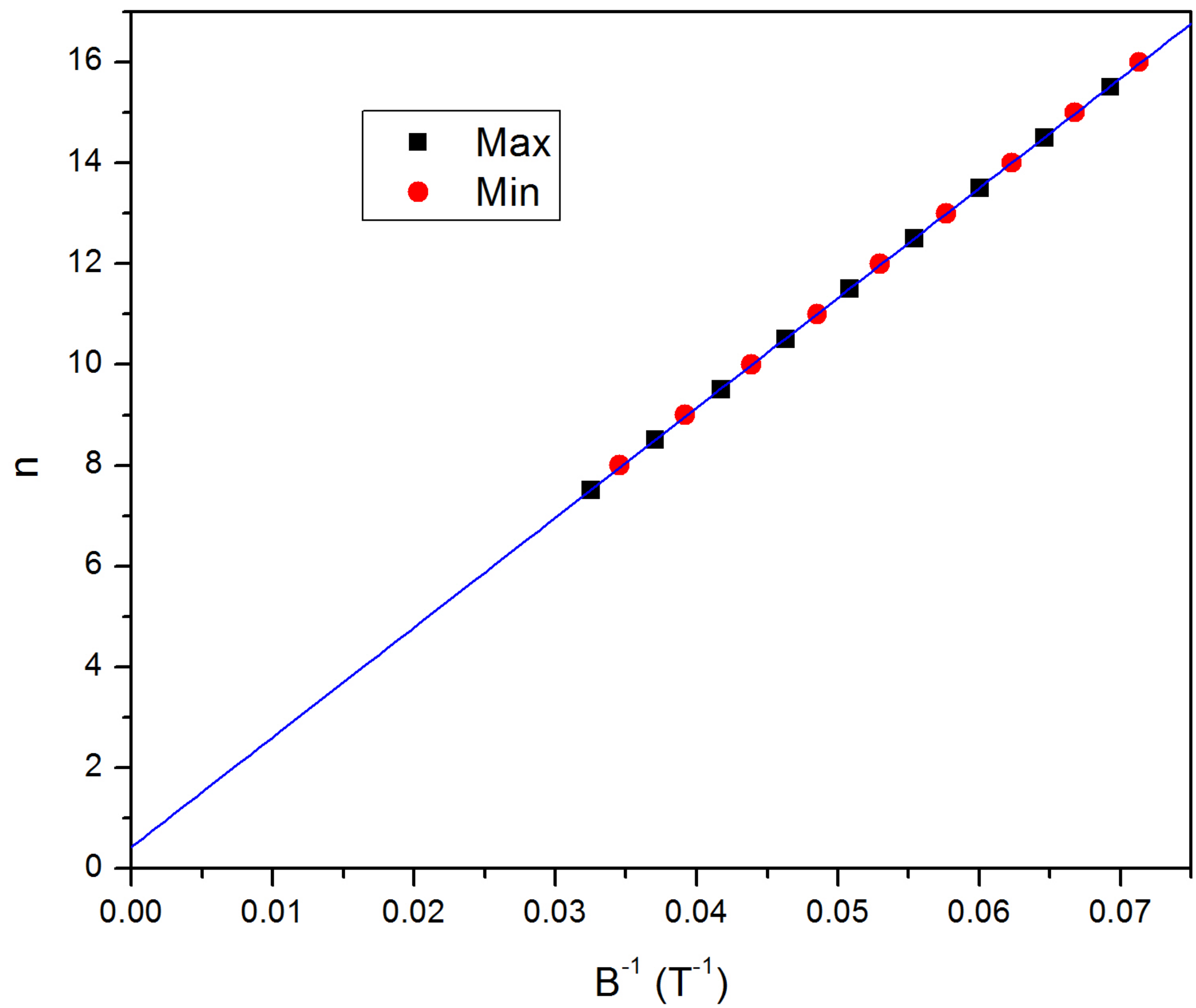

Figure 4.38: The Landau level fan diagram of the Sb_2Te_2Se single crystal.

from the topological surface states.

4.5.6 Lifshitz Kosevich Analyses

The characteristic angle dependence and the value of the Berry phase show that the SdH oscillations in the transport data are predominantly caused by the topological surface states in the Sb_2Te_2Se single crystal. We have used the Lifshitz Kosevich (LK) theory to calculate the different physical parameters which characterize the observed quantum oscillations. The frequency of oscillations, $F = 215$ T, corresponds to a Fermi momentum $k_F = 8\times10^6$ cm^{-1} according to the Onsager relation $F = \hbar/(2\text{e})k_F{}^2$. The value of k_F is almost 3 times larger than that obtained in our study on the $Bi_2Se_{2.1}Te_{0.9}$ topological insulator [46], indicating the higher position of the Fermi level from the Dirac point in the Sb_2Te_2Se single crystal. For a circular Fermi surface, this value of k_F results in a surface carrier density of $n_{2D} = k_F^2\ /4\pi$ $= 5.7\times10^{12}\ cm^{-2}$.

The temperature dependence of quantum oscillations is described by the LK formula,

$$\Delta R(T,B) = \Delta R_0 e^{-\lambda_D(B)} \frac{\lambda(T/B)}{sinh[\lambda(T/B)]} \tag{4.6}$$

with

$$\lambda_D(B) = \frac{2\pi^2 k_B}{\hbar e} m_{cyc} \frac{T_D}{B} \tag{4.7}$$

$$\lambda(T/B) = \frac{2\pi^2 k_B T}{\Delta E_N(B)} \tag{4.8}$$

The first term in Eq. [4.6], ΔR_0, is the amplitude of the oscillation in the high-field limit $1/B \to 0$. The next term is the Dingle factor representing the exponential decrease of ΔR with decreasing field B. In the last term, $\Delta E_N(B) = \hbar eB/m_{cyc}$

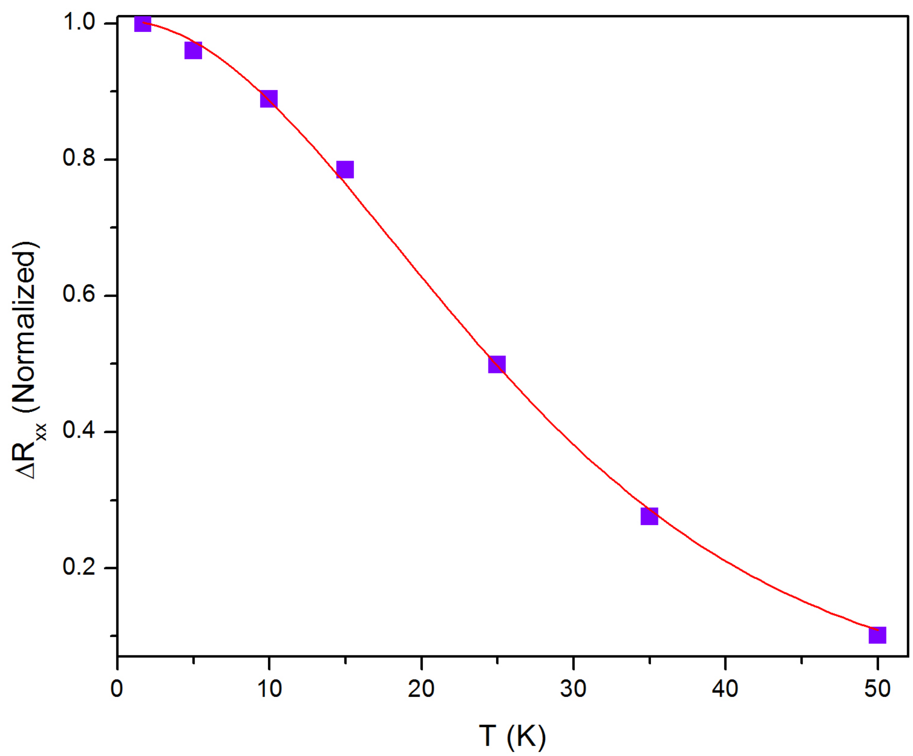

Figure 4.39: Temperature-dependence of the amplitude of the SdH oscillation (ΔR_{xx}) at $B = 28.8$ T. The red line represents the fit to the equation for ΔR_T.

and it describes the attenuation of ΔR_{xx} with increasing temperature T, m_{cyc} is the cyclotron mass of the charge carriers and T_D is the Dingle temperature which is related to the inverse life time of the carriers. Figure [4.39] shows the temperature dependence of the amplitude of the SdH oscillation of the Sb_2Te_2Se single crystal at $B = 28.8$ T. The red line shows the LK fit to the data. The LK formula describes the temperature-dependence of ΔR_{xx} very well. From the fitting to the LK formula, we have calculated the magnetic field-dependence of the energy difference between two consecutive Landau levels $\Delta E_N(B)$ as shown in Fig. [4.40]. The spacing energy $\Delta E_N(B)$ depends linearly on the applied magnetic field. From the slope of the linear fit to the data, we have calculated the cyclotron mass $m_{cyc} = 0.1m_0$, where m_0 is

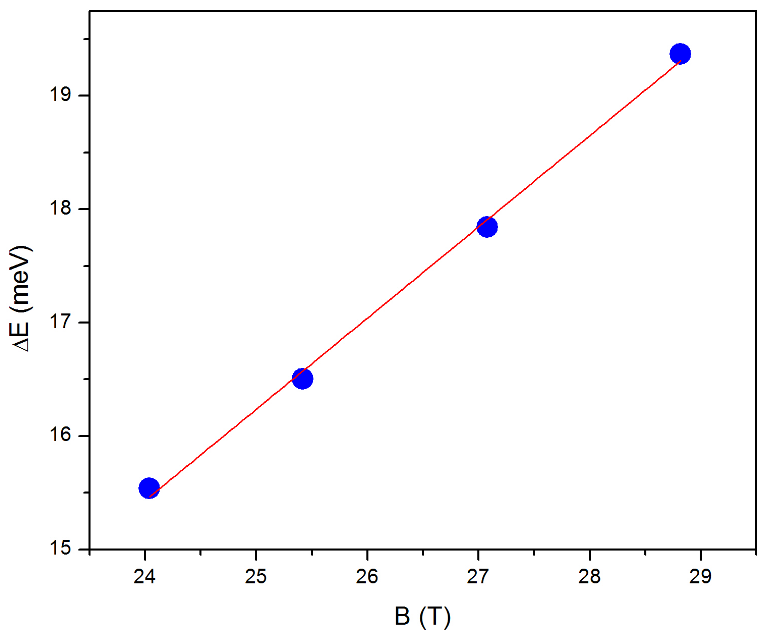

Figure 4.40: Magnetic field-dependence of the parameter ΔE_N of the Sb_2Te_2Se single crystal. The solid red line shows a linear fit to the data.

the rest mass of an electron. Using the linear dispersion relation for surface state $v_F = \hbar k_F/m_{cyc}$, we have estimated the Fermi velocity $v_F = 6.7 \times 10^5\ ms^{-1}$.

Following the standard Dingle temperature analysis, we have calculated the Dingle temperature, T_D, from the slope of the semilogarithmic plot, as shown in Fig. [4.41], $T_D = 35$ K. With the value of $T_D = 35$ K, the surface carrier life time $\tau = \hbar/2\pi k_B T_D$ is estimated to be 3.5×10^{-14} s. Similarly, other physical parameters like the mean free path $l = v_F\tau$, mobility $\mu = e\tau/m_c$ and Fermi energy E_F are estimated to be 23 nm, 600 cm^2/Vs, and 250 meV respectively. These physical parameters are comparable with the previous reports on other topological systems.

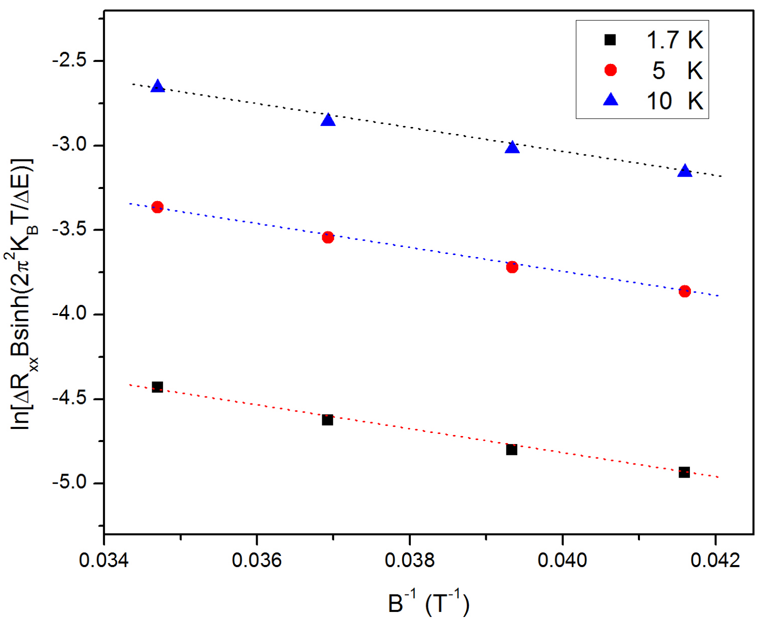

Figure 4.41: Dingle plot used to determine the Dingle temperature T_D and the carrier lifetime τ of the Sb_2Te_2Se single crystal.

4.5.7 Discussion

From the angle dependence and the Berry phase calculations, we have proved the existence of topological surface states in the Sb_2Te_2Se single crystal. It is interesting to observe topological surface states in the metallic Sb_2Te_2Se with such a high oscillation frequency. We have not observed any signature of a second frequency as observed in our previous study of $Bi_2Se_{2.1}Te_{0.9}$ [46]. The higher value of the Fermi wave vector k_F in the Sb_2Te_2Se implies the higher position of the Fermi energy w.r.t. the Dirac point. Following similar argument as before [46], although the Fermi energy is higher in the Sb_2Te_2Se crystal, it still cuts the two valence band maxima in the band structure. That is why it still shows a metallic behavior and has the p-type bulk carriers. Due to the higher value of the bulk states Fermi wave vector, an even higher magnetic field strength is needed to observe quantum oscillations from the bulk states as constrained by the relation $F/B_n - \beta = (n-1)$, where n represents the Landau level. This explains qualitatively the dominance of topological surface states in the Sb_2Te_2Se single crystal. The bulk states interference might be seen at higher magnetic field, beyond the 31 T maximum magnetic field of this study. The smaller value of the electron mean free path (l) in the Sb_2Te_2Se sample as compared to that for the $Bi_2Se_{2.1}Te_{0.9}$ sample implies the presence of more scattering centers in the Sb_2Te_2Se sample. The more the scattering centers, the smaller the electron mobility. This is consistent with the lower value of electron mobility (μ) in the Sb_2Te_2Se than in the $Bi_2Se_{2.1}Te_{0.9}$ sample.

Chapter 5

Conclusion

In this dissertation, we have investigated the topological surface states in three classes of metallic topological compounds; namely $Bi_2Se_{2.1}Te_{0.9}$, Bi_2Te_3 and Sb_2Te_2Se. Magnetotransport studies at high fields were carried out to see different physical phenomena like Shubnikov de Haas oscillations and weak antilocalization. $Bi_2Se_{2.1}Te_{0.9}$ is metallic and has p-type bulk carriers. The angle dependence of quantum oscillations in a magnetic field of up to 7 T and Berry phase calculations showed the suface states origin of the quantum oscillations. There is a negligible interference from the bulk states frequency in the frequency spectrum. However, the interference increases with an increase in magnetic field strength. The surface states quantum oscillations dominate at low magnetic field and the surface to bulk states cross-over takes place at higher magnetic field. Similarly, the quantum oscillations at high field in the Sb_2Te_2Se sample were revealed to originate from surface states although the bulk state is p-type and shows metallic behaviour. The physical reason for the dominance of topological surface states in p-type metallic sample is due to the "M" shaped valence band structure. If the Fermi energy, measured from the Dirac point, is low enough that it cuts two valence bands, then the sample is metallic and p-type. In this case, the Fermi wave vector for the surface states is small, whereas it is large for the bulk state. That is the reason the surface states quantum oscillation dominates at low magnetic field. The position of the Fermi energy determines the value of the Fermi wave vectors (both surface and bulk). Due to the higher value of the Fermi energy in the Sb_2Te_2Se sample, we have not observed the bulk states oscillation even up to 31 T magnetic field in the frequency spectrum, as observed in the $Bi_2Se_{2.1}Te_{0.9}$ sample. However, the bulk state interference is expected beyond the current magnetic field range.

We have observed weak antilocalization in the metallic Bi_2Te_3 single crystals having different bulk carrier densities. The angle dependence of weak antilocalization with respect to the direction of the magnetic field showed the surface states dominance in the samples having lower carrier concentration. The surface states dominance in WAL does not depend the nature of the bulk charge carriers (p or n-type). Using the Hikami-Larkin-Nagaoka formula, we have found the number of conduction channels is small in the samples having lower carrier concentration. This explains the surface state dominance in the mangetoconductivity of those samples. In this work, we have demonstrated the existence of topological surface states in metallic topological compounds. This work opens a new window for the search and study of topological surface states even in metallic topological insulators.

Bibliography

[1] H. K. Onnes. The resistance of pure mercury at helium temperatures. *Communication Physics Laboratory Univiersity Leiden*, 14:818, 1911.

[2] K. V. Klitzing, G. Dorda, and M. Pepper. New method for high-accuracy determination of the fine-structure constant based on quantized hall resistance. *Physical Review Letters*, 45:494–497, 1980.

[3] D. C. Tsui, H. L. Stormer, and A. C. Gossard. Two-dimensional magnetotransport in the extreme quantum limit. *Physical Review Letters*, 48:1559–1562, 1982.

[4] M. Z. Hasan and C. L. Kane. Colloquium: Topological insulators. *Reviews of Modern Physics*, 82:3045–3067, 2010.

[5] Y. Ando. Topological insulator materials. *Journal of the Physical Society of Japan*, 82:1–32, 2013.

[6] A. P. Schnyder, S. Ryu, A. Furusaki, and A. W. W. Ludwig. Classification of topological insulators and superconductors. *AIP Conference Proceedings*, 1134:10–21, 2009.

[7] Y. Xu, I. Miotkowski, C. Liu, J. Tian, H. Nam, N. Alidoust, J. Hu, C. K. Shih, M. Z. Hasan, and Y. P. Chen. Observation of topological surface state quantum Hall effect in an intrinsic three-dimensional topological insulator. *Nature Physics*, 10:956–963, 2014.

[8] C. Z. Chang, J. Zhang, X. Feng, J. Shen, Z. Zhang, M. Guo, K. Li, Y. Ou, P. Wei, L. L. Wang, Z. Q. Ji, Y. Feng, S. Ji, X. Chen, J. Jia, X. Dai, Z. Fang, S. C. Zhang, K. He, Y. Wang, L. Lu, X. C. Ma, and Q. K. Xue. Experimental observation of the quantum anomalous Hall effect in a magnetic topological insulator. *Science*, 340:167–170, 2013.

[9] J. Zhang, C. Z. Chang, P. Tang, Z. Zhang, X. Feng, K. Li, L. L. Wang, X. Chen, C. Liu, W. Duan, K. He, Q. K. Xue, X. Ma, and Y. Wang. Topology driven magnetic quantum phase transition in topological insulators. *Science*, 339:1582–1586, 2013.

[10] L. Fu and C. L. Kane. Superconducting proximity effect and majorana fermions at the surface of a topological insulator. *Physical Review Letters*, 100:0964071–0964074, 2008.

[11] A. R. Akhmerov, J. Nilsson, and C. W. J. Beenakker. Electrically detected interferometry of Majorana fermions in a topological insulator. *Physical Review Letters*, 102:2164041–2164044, 2009.

[12] Y. S. Hor, A. J. Williams, J. G. Checkelsky, P. Roushan, J. Seo, Q. Xu, H. W. Zandbergen, A. Yazdani, N. P. Ong, and R. J. Cava. Superconductivity in

$Cu_xBi_2Se_3$ and its implications for pairing in the undoped topological insulator. *Physical Review Letters*, 104:0570011–0570014, 2010.

[13] Z. Liu, X. Yao, J. Shao, M. Zuo, L. Pi, S. Tan, C. Zhang, and Y. Zhang. Superconductivity with topological surface state in $Sr_xBi_2Se_3$. *Journal of the American Chemical Society*, 137:10512–10515.

[14] D. X. Qu, Y. S. Hor, J. Xiong, R. J. Cava, and N. P. Ong. Quantum oscillations and Hall anomaly of surface states in the topological insulator Bi_2Te_3. *Science*, 329:821–824, 2010.

[15] C. Kittel. *Introduction to Solid State Physics*. Wiley India Pvt. Limited, seventh edition, 2006.

[16] L.D. Landau and E.M Lifshitz. *Statistical Physics*. Elsevier, third edition, 1980.

[17] L. Fu, C. L. Kane, and E. J. Mele. Topological insulators in three dimensions. *Physical Review Letters*, 98(10):1–4, 2007.

[18] J. E. Moore and L. Balents. Topological invariants of time-reversal-invariant band structures. *Physical Review B*, 75:3–6, 2007.

[19] R. Roy. Three dimensional topological invariants for time reversal invariant Hamiltonians and the three dimensional quantum spin Hall effect. *Physical Review B*, 79(2009):195322–195327, 2006.

[20] D. Hsieh, D. Qian, L. Wray, Y. Xia, Y. S. Hor, R. J. Cava, and M. Z. Hasan. A topological Dirac insulator in a quantum spin Hall phase. *Nature*, 452(7190):970–974, 2008.

[21] D. Hsieh, Y. Xia, L. Wray, D. Qian, A. Pal, J. H. Dil, J. Osterwalder, F. Meier, G. Bihlmayer, C. L. Kane, Y. S. Hor, R. J. Cava, and M. Z. Hasan. Observation of unconventional quantum spin textures in topological insulators. *Science*, 323:919–922, 2009.

[22] J. E. Moore. The birth of topological insulators. *Nature*, 464:194–198, 2010.

[23] K. Ueno, K. Shiga, S. Morina, and T. Sunada. *A mathematical gift I: The interplay between topology, functions, geometry, and algebra*. American Physical Society, 2003.

[24] D. J. Thouless, M. Kohmoto, M. P. Nightingale, and M. D. Nijs. Quantized Hall conductance in a two-dimensional periodic potential. *Physical Review Letters*, 49(6):405–408, 1982.

[25] S. Murakami, N. Nagaosa, and S. C. Zhang. Dissipationless quantum spin current at room temperature. *Science*, 301:1348–1351, 2003.

[26] M. Onoda and N. Nagaosa. Spin current and accumulation generated by the spin hall insulator. *Physical Review Letters*, 95:106601–106604, 2005.

[27] C. L. Kane and E. J. Mele. Quantum spin Hall effect in graphene. *Physical Review Letters*, 95:2269011–2269014, 2005.

[28] M. König, L. W. Molenkamp, X. L. Qi, and S. C. Zhang. Quantum spin Hall state in HgTe quantum wells. *Science*, 766:766–771, 2012.

[29] D. Shoenberg. *Magnetic Oscillations in Metals*. Cambridge University Press, 1984.

[30] Ashcroft, N. W. and Mermin, N. D. *Solid State Physics*. Books/Cole, Cengage Learning, 1976.

[31] H. Z. Lu and S. Q. Shen. Weak localization and Weak Antilocalization in topological insulators. *Proceedings of Society of Photographic Instrumentation Engineers*, 9167:91672E1–91672E11, 2014.

[32] H. T. He, G. Wang, T. Zhang, I. K. Sou, G. K. L. Wong, J. N. Wang, H. Z. Lu, S. Q. Shen, and F. C. Zhang. Impurity effect on Weak Antilocalization in the topological insulator Bi_2Te_3. *Physical Review Letters*, 106:1668051–1668054, 2011.

[33] C. Shekhar, C. E. V. Barbosa, B. Yan, S. Ouardi, W. Schnelle, G. H. Fecher, and C. Felser. Evidence of surface transport and weak anti-localization in single crystal of Bi_2Te_2Se topological insulator. *arXiv*, 90:1651401–1651406, 2014.

[34] J. Lee, J. Park, J. H. Lee, J. S. Kim, and H. J. Lee. Gate-tuned differentiation of surface-conducting states in $Bi_{1.5}Sb_{0.5}Te_{1.7}Se_{1.3}$ topological-insulator thin crystals. *Physical Review B*, 86(24):1–10, 2012.

[35] H. Z. Lu and S. Q. Shen. Finite-temperature conductivity and magnetoconductivity of topological insulators. *Physical Review Letters*, 112:1466011–1466016, 2014.

[36] P. W. Anderson. Absence of diffusion in certain random lattices. *Physical Review*, 109:1492–1505, 1958.

[37] S. Hikami, A. I. Larkin, and Y. Nagaoka. Spin-orbit interaction and magnetoresistance in the two-dimensional random system. *Progress of Theoretical Physics*, 63:707–710, 1980.

[38] L Bao, L. He, N Meyer, X Kou, P. Zhang, Z. G. Chen, A. V. Fedorov, J. Zou, T. M. Riedemann, T. A. Lograsso, K. L. Wang, G. Tuttle, and F. Xiu. Weak Antilocalization and quantum oscillations of surface states in topological insulator Bi_2Se_2Te. *Scientific Reports*, 2:1–7, 2012.

[39] A. A. Taskin, Z. Ren, S. Sasaki, K. Segawa, and Y. Ando. Observation of dirac holes and electrons in a topological insulator. *Physical Review Letters*, 107:1–4, 2011.

[40] A. A. Taskin and Y. Ando. Quantum oscillations in a topological insulator $Bi_{1-x}Sb_x$. *Physical Review B*, 80:0853031–0853036, 2009.

[41] N. H. Tu, Y. Tanabe, K. K. Huynh, Y. Sato, H. Oguro, S. Heguri, K. Tsuda, M. Terauchi, K. Watanabe, and K. Tanigaki. Van der Waals epitaxial growth of topological insulator $Bi_{2-x}Sb_xTe_{3-y}Se_y$ ultrathin nanoplate on electrically insulating fluorophlogopite mica. *Applied Physics Letters*, 105:3–8, 2014.

[42] J. G. Analytis, R. D. McDonald, S. C. Riggs, J. H. Chu, G. S. Boebinger, and I. R. Fisher. Two-dimensional surface state in the quantum limit of a topological insulator. *Nature Physics*, 6(12):66–64, 2010.

[43] Z. Ren, A. A. Taskin, S. Sasaki, K. Segawa, and Y. Ando. Large bulk resistivity and surface quantum oscillations in the topological insulator Bi_2Te_2Se. *Physical Review B (Rapid Communication)*, 82:2413061–24130614, 2010.

[44] J. Xiong, A. C. Petersen, D. Qu, Y. S. Hor, R. J. Cava, and N. P. Ong. Quantum oscillations in a topological insulator Bi_2Te_2Se with large bulk resistivity. *Physica E*, 44:917–920, 2012.

[45] A. A. Taskin, S. Sasaki, K. Segawa, and Y. Ando. Achieving surface quantum oscillations in topological insulator thin films of Bi_2Se_3. *Advanced Materials*, 24:5581–5585, 2012.

[46] K. Shrestha, V. Marinova, B. Lorenz, and C. W. Chu. Shubnikov de Haas oscillations from topological surface states of metallic $Bi_2Se_{2.1}Te_{0.9}$. *Physical Review B (Rapid Communication)*, 90:2411111–2411115, 2014.

[47] B. Jalan, S. Stemmer, S. MacK, and S. J. Allen. Two-dimensional electron gas in δ-doped $SrTiO_3$. *Physical Review B*, 82:0811031–0811034, 2010.

[48] G. Li, Z. Xiang, F. Yu, T. Asaba, B. Lawson, P. Cai, C. Tinsman, A. Berkley, S Wolgast, Y. S. Eo, D. J. Kim, C. Kurdak, J. W. Allen, K. Sun, X. H. Chen, Y. Y. Wang, Z. Fisk, and L Li. Two-dimensional Fermi surfaces in Kondo insulator SmB_6. *Science*, 346:1208–12012, 2013.

[49] G. Xu, W. Wang, X. Zhang, Y. Du, E. Liu, S. Wang, G. Wu, Z. Liu, and X. X. Zhang. Weak Antilocalization effect and noncentrosymmetric superconductivity in a topologically nontrivial semimetal LuPdBi. *Scientific reports*, 4:57091–57097, 2014.

[50] T. Chen, Q. Chen, K. Schouteden, W. Huang, X. Wang, Z. Li, F. Miao, X. Wang, Z. Li, B. Zhao, S. Li, F. Song, J. Wang, C. V. Haesendonck, B. Wang, and

G. Wang. Aging the Cu-doped Bi_2Te_3 crystals for the topological transport and its atomic tunneling-clustering dynamics. *Nature Communication*, 5:1–8, 2014.

[51] J. Chen, X. Y. He, K. H. Wu, Z. Q. Ji, L. Lu, J. R. Shi, J. H. Smet, and Y. Q. Li. Tunable surface conductivity in Bi_2Se_3 revealed in diffusive electron transport. *Physical Review B (Rapid Communication)*, 83(24):2413041–2413044, 2011.

[52] X. Zhu, L. Santos, C. Howard, R. Sankar, F. C. Chou, C. Chamon, and M. El-Batanouny. Electron-phonon coupling on the surface of the topological insulator Bi_2Se_3 determined from surface-phonon dispersion measurements. *Physical Review Letters*, 108:185501–185504, 2012.

[53] J. G. Checkelsky, Y. S. Hor, M. H. Liu, D. X. Qu, R. J. Cava, and N. P. Ong. Quantum interference in macroscopic crystals of nonmetallic Bi_2Se_3. *Physical Review Letters*, 103:2466011–2466014, 2009.

[54] Y. L. Chen, J. G. Analytis, J. H. Chu, Z. K. Liu, S. K. Mo, X. L. Qi, H. J. Zhang, D. H. Lu, X. Dai, Z. Gang, S. C. Zhang, Hussain Z. Fisher, I. R., and Z. X. Shen. Experimental realization of a three-dimensional topological insulator Bi_2Te_3. *Science*, 325:178–181.

[55] H. Zhang, C. X. Liu, X. L. Qi, X. Dai, Z. Fang, and S. C. Zhang. Topological insulators in Bi_2Se_3, Bi_2Te_3 and Sb_2Te_3 with a single Dirac cone on the surface. *Nature Physics*, 5:438–442, 2009.

[56] H. Lin, T. Das, L. A. Wray, S. Y. Xu, M. Z. Hasan, and A. Bansil. An isolated Dirac cone on the surface of ternary tetradymite-like topological insulators. *New Journal of Physics*, 13:0–6, 2011.

[57] W. Zhang, R. Yu, H. J. Zhang, X. Dai, and Z. Fang. First-principles studies of the three-dimensional strong topological insulators Bi_2Te_3, Bi_2Se_3 and Sb_2Te_3. *New Journal of Physics*, 12:0650131–06501314, 2010.

[58] S. Y. Xu, L. A. Wray, Y. Xia, R. Shankar, A. Petersen, A. Fedorov, H. Lin, A. Bansil, Y. S. Hor, D. Grauer, R. J. Cava, and M. Z. Hasan. Discovery of several large families of topological insulator classes with backscattering-suppressed spin-polarized single-Dirac-cone on the surface. *Arxiv.org*, 5111:1–11, 2010.

[59] K. Wang, D. Graf, and C. Petrovic. Large magnetothermopower and Fermi surface reconstruction in Sb_2Te_2Se. *Physical Review B*, 89:1252021–1252026, 2014.